UC Berkeley
UC Berkeley Electronic Theses and Dissertations

Title

The Impact of Electron—Hole Correlations on the Dynamics of Excitons and Biexcitons in Semiconductor Nanomaterials

Permalink

https://escholarship.org/uc/item/3jd146sr

Author

Philbin, John Patrick

Publication Date

2020

Peer reviewed|Thesis/dissertation

The Impact of Electron–Hole Correlations on the Dynamics of Excitons and Biexcitons in Semiconductor Nanomaterials

by

John Patrick Philbin

A dissertation submitted in partial satisfaction of the

requirements for the degree of

Doctor of Philosophy

in

Chemistry

in the

Graduate Division

of the

University of California, Berkeley

Committee in charge:

Professor Eran Rabani, Chair
Professor David T. Limmer
Professor Eric Neuscamman
Professor Jeffrey B. Neaton

Spring 2020

The Impact of Electron–Hole Correlations on the Dynamics of Excitons and Biexcitons in
Semiconductor Nanomaterials

Abstract

The Impact of Electron–Hole Correlations on the Dynamics of Excitons and Biexcitons in Semiconductor Nanomaterials

by

John Patrick Philbin

Doctor of Philosophy in Chemistry

University of California, Berkeley

Professor Eran Rabani, Chair

The creation of novel technologies based on semiconductor nanomaterials relies on new insights into the chemistry and physics of these confined systems. These insights will help propel chemically synthesized semiconductor nanomaterials from a class of materials that have been promised to revolutionize industries ranging from solar energy and carbon capture to medicine and quantum computing to a commercially viable class of materials. A major roadblock impeding nanomaterial-based applications is the lack of a detailed understanding of the many–body interactions in nanomaterials, in particular the quasiparticle–quasiparticle (e.g. quasielectron–hole, exciton–exciton) interactions are not well understood.

In this work, we enhance our understanding of quasiparticle–quasiparticle interactions in confined semiconductor nanomaterials through the development of theories and computational methods capable of calculating observables in nanomaterials with hundreds to tens of thousands of atoms. Furthermore, we apply these methods, often in close collaboration with experimentalist, to nanomaterials ranging from quasi–0D single material quantum dots to quasi–2D heterostructure nanoplatelets in order to test the accuracy of the formalisms and improve our understanding of semiconductor nanomaterials.

In the introduction, a brief overview of semiconductor nanomaterials is given with a focus on the impact that the size and shape have on the properties of the nanomaterial. The important timescales and decay channels of excitons (i.e. bound quasielectron–hole pairs) and biexcitons are reviewed in the introduction. In Chapter 2, we develop a new formalism for calculating Auger recombination lifetimes, which is typically the dominant decay channel of biexcitons in semiconductor nanomaterials. And we show that the inclusion of quasielectron–hole correlations in the new, interacting formalism results in it being the first quantitatively accurate formalism for calculating Auger recombination lifetimes for quantum dots in both the strong and weak confinement regimes. Furthermore, we highlight how the interacting formalism is the first theoretical method to postdict the experimentally known

"universal volume scaling law" for quantum dots in Chapter 2. In Chapter 3, we develop a low–scaling approach based on the stochastic resolution of identity. We then elucidate the shell thickness and band alignment dependencies of the biexciton Auger recombination lifetime for quasi–type–II CdSe/CdS and type–I CdSe/ZnS core/shell quantum dots. We find that the biexciton Auger recombination lifetime increases with the total nanocrystal volume for quasi–type–II CdSe/CdS core/shell quantum dots and is independent of the shell thickness for type–I CdSe/ZnS core/shell quantum dots. The impact that growing shells with shorter lattice constants (CdS and ZnS) has on the emission energies of CdSe cores is also discussed. In Chapter 4, we report on the size dependence of Auger recombination in CdSe nanorods and that noninteracting formalisms are incapable of accurately predicting Auger recombination lifetimes in nanorods. On the other hand, we show that our interacting formalism is accurate in nanorods. We then utilize kinetic modeling to uncover a competition between the kinetics of Auger recombination and charge separation in a hybrid semiconductor–metal nanoparticle. Next, we discuss how the alloying of Zn into the CdS shell can improve the optoelectronic properties of seeded nanorods. In Chapter 5, we apply the stochastic implementation of the interacting formalism to quasi–2D nanoplatelets. We find that the Auger recombination lifetimes depend nearly linearly on the lateral area and thickness of the nanoplatelet. We also connect these scalings to those of the area and thickness dependencies of single exciton radiative recombination lifetimes, exciton coherence areas, and exciton Bohr radii in these quasi–2D materials.

In loving memory of my best friend and brother,
Michael Philbin

Contents

List of Figures

List of Tables

Acknowledgements

The importance of the unconditional support and love that I have received from my parents, Joe and Diane Philbin, cannot be overstated – thank you mom and dad. The love and friendship of my siblings, Matt, Mike, Kevin, Tim, Colleen, and sister–in–law Sandy, has been amazing. I have also been blessed to have an exceptionally large and supportive extended family: thank you to all of my aunts, uncles, and cousins. I am truly lucky to have all of you always there for me. Mom and dad, all I need to do to see a great example of how to love and support someone through the good and bad times is to look at how you support not only one another but each one of your children, siblings, and countless nieces and nephews. Matt, your positivity and focus on solving important problems amazes and inspires me. Our phone conversations about topics ranging from my research on quantum dots to the possibility of using antimatter as an energy source have both been useful discussions for me to remind me of the big picture of my research as well as fun discussions on the wild, unlimited possibilities of science. It is those very wild, unlimited possibilities of science that originally got me interested in mathematics and science as a middle and high school student watching shows about string theory and the physics of the impossible with Mike. Kevin and Tim, the joy I receive from being your older brother is not measurable. I am very proud of both of you, and I look forward to making many more memories with you both. It is fitting that my Ph.D. studies began with Tim and my mom coming to Singapore to help move me back to the US and ended with a (research) trip to Australia with Kevin and my mom; thank you for joining me on these adventures and for giving me the peace of mind knowing that you both are always there for me. And Colleen, littles, I am so proud of the smart, beautiful, and strong woman that you have become over the years. I also need to thank my love, Victoria Sakal. From the time I thought I was going to fall down the stairs because my heart was beating so fast while leaving your NYC apartment for the first time to living together in San Francisco, our time together has been amazing and your love has been crucial to my success in graduate school, thank you.

I would like to thank my adviser, Eran Rabani, for his guidance during my tenure in his research group. I cannot imagine having had a better advisor throughout graduate school. It is crazy to recall the progression I made in your research group. In my first year, we would derive equations and code together in your office and I would almost entirely just watch and catch small bugs as you coded. This then transitioned to us taking turns controlling the keyboard while coding up the equations that I derived until I eventually understood the numerics and algorithms well enough to successfully code up programs quickly on my own. Not only were you crucial to the development of my scientific skills, but, arguably more importantly, the training I received from you on how to challenge, debate (maybe the correct word is argue given how high the decibel levels often get), and quickly test hypothesis has been world class. In addition to being a great scientist and mentor, you are a great, kind person. It has been inspiring to see you build and expand your research group in Berkeley while continuing to be an awesome father to your children and advisor to everyone in the group. I look forward to our many more encounters over the years.

In my time in the Rabani group, I had the privilege to work and become friends with a large number of top scientists and amazing people. My journey began in the basement of Gilman Hall where Tyler Takeshita and I were fortunate to have been given one of the only offices with a window. It was a pleasure to share an office with Tyler for a majority of my Ph.D. studies. Tyler was always down to teach and discuss science, and he was a great mentor for me. Tyler and I were soon joined by Ming Chen and Lyran Kidon as the Rabani group expanded its Berkeley presence. Ming brought not only exceptional technical abilities that undoubtedly benefitted everyone in the group but also was always available and willing to help me when I ran into trouble. I also really enjoyed our dinners together in the office. Lyran, your analytic skills were fun to see in action, and I appreciate your willingness and aptitude for teaching complex concepts. The group soon quickly expanded with the additions of Alex Lee, Wenjie Dou, Amikam Levy, Dipti Jasrasaria, Nathan Ng, Paul Wrona, and Daniel Weinberg. I am lucky to have been able to work and spend time with all of you. Alex, our afternoon ping pong games were always a welcome break. Dipti, thank you for being a good friend and collaborator. I always enjoyed our early morning discussions in the office whether we were discussing research, current events, or future plans – your scientific future is very bright. Wenjie, from taking graduate quantum together at UPenn to sharing an office together in Berkeley, it has been a pleasure. I have particularly enjoyed learning quantum dynamics from you. Amikam, Nathan, Paul, and Daniel: it has been a joy getting to know you over the past few years. I also would like to thank the talented undergraduates that I was able to work with during my time in the Rabani group: Michael Lostica, Joseph Kelly, and Devan Skubitz. Lastly, I would like to thank my first mentor from the Rabani group, Hagai Eshet.

In terms of collaborators, I am honored to thank Uri Banin, Ido Hadar, Yuval Ben–Shahar, Richard Schaller, Dmitri Talapin, Alexandra Brumberg, Paul Alivisatos, Chang Yan, and Justin Ondry. Uri, Ido, and Yuval, I sincerely appreciate you hosting me on my visits to Israel and your hard work during our successful collaborations. Rich and Alexandra, thank you for allowing me to visit Northwestern multiple times and for being great collaborators. Paul, Chang, and Justin, I could not have asked for better experimentalists to work with and learn nanoscience from while here at UC Berkeley, thank you. I would also like to thank Steven Louie, Felipe da Jornada, and Sivan Rafaely–Abramson for countless meetings and helpful discussions about my research and condensed matter physics.

To my Berkeley squad: Jose Roque, Ilya Piskun, and Alec Christian. The squad got off to a fast starting, immediately making our presence in Berkeley known, by taking the non–competitive intramural basketball league by storm with an undefeated season in my first year at Berkeley. Although I do fear we may have retired from organized basketball too early following that magical run, I thoroughly enjoyed all of our squad lunches, pick–up basketball games, and constant roasting of one another (primarily Ilya though) in our group chat. Jose, I knew from the first night we met that our friendship was going to be filled with good clean fun. Your work–ethic and relentless pursuit of scientific ingenuity has inspired me throughout my Ph.D. studies. I very confident that you will continue to do great work throughout your scientific career. Ilya, you not only led the squad in passion for basketball, but I want the

record to show that you have the second best basketball left hand in the squad. Off the court, you, Ilya, have been as supportive a friend as one could ask for. I appreciate your support and punctuality over the past 5 years. Alec, our friendship began with some healthy competition in a bowling alley in San Francisco which we then transitioned into daily early morning lifting competitions and annual Chemistry league softball championships games. No matter the activity we were competing in or who won and who lost (although I cannot remember ever losing), I will always look back fondly on these times and am very excited to get back to picking up and setting down heavy objects with you in Boston. Thank you for the healthy doses of competition that I needed and being an all–around great friend.

I would also like to thank many friends that I have had the fortune to get to know over the years before moving to Berkeley in August of 2015. From my time in Singapore: Calum Nicholl, Scott Moore, Vishan Wikramanayake, Bradley Schmitz, and Robert Teigland. My mood is always lifted when I recall the memories we made over the course of my year in Singapore along with the unforgettable trips within the United States. From UPenn: Kris Martin, Rob Harwood, Tosan Eyetsemitan, Evan Jackson, Dan Wilk, Christine Bowman, Alex Genshaft, and Nathan Koocher. Thank you for your support and friendship over the years. Kris, Rob, Tosan, and Evan, the times we had in 3928 can never be replaced, thank you for the great memories. Dan, our times together at Independence Hall were top notch — thanks for being great friends and housemates. Christine Bowman, Alex Genshaft, and Nathan Koocher, it has been great to mature with all of you from incoming freshman at UPenn to all of us completing our doctorate degrees, I cannot thank you enough for your support. Lastly, I would also like to thank my friends from middle and high school in Green Bay that have been there for me during all of the good and bad times: Justin Mulloy, Mitch Chester, Tyler Harke, Matt Mamrosh, and Trevor Bowman.

Altogether, thank you to all of my family, friends, and colleagues that have made my experience earning a Chemistry Ph.D. from UC Berkeley so enjoyable and rewarding.

Chapter 1

Introduction

1.1 Semiconductor nanomaterials

Semiconductors are ubiquitous in applications that involve either light emission or light harvesting, including lasers, photodetectors, photovoltaic cells and light–emitting diodes. Almost immediately following the discovery of semiconductor nanocrystals (NCs),[10–12] the potential of NCs to be a key material for the next generation of semiconductors was recognized due to their optical and electronic properties being readily tunable by controlling the size, shape and composition of the NC.[13–15] A simple way to understand how the optical and electronic properties of nanomaterials can be controlled by changing the size is by recalling the results of a particle in a box. Specifically, the energy eigenstates of a particle in 1D box of length L are

$$E_\mathrm{n} = \frac{n^2\pi^2\hbar^2}{2mL^2} \tag{1.1}$$

where n is a positive index and m is the mass of the particle. Therefore, by changing the length of the box (i.e. the size of the nanomaterial) one can continuously tune the energy eigenstates. In other words, by changing the particle size one can tune the degree of quantum confinement, and, as will be discussed in detail in future chapters, the size of the particle also determines more exotic properties of the nanomaterial.[3,14,16]

In terms of the variety of semiconductor nanostructures, the simplest colloidal nanomaterials are those of quasi–0D quantum dots (QDs), quasi–1D nanorods (NRs), and quasi–2D nanoplatelets (NPLs) made of a single material. The range of shapes, sizes, and compositions of nanomaterials that have been synthesized is now very large, with complex heterostructures of mixed dimensionality now commonly being synthesized (Figure 1.1).[17–23] In this work, a major focus will be on understanding the size and shape dependent properties of photo-excited QDs, NRs, and NPLs (Figure 1.1). An interesting aspect of confined nanomaterials that will not be discussed much in this work but is worth noting is that of the nanomaterial surface.[24,25] The size and shape dependent surface to volume ratios and surface curvatures are known to have important consequences in both the optical and electronic properties of
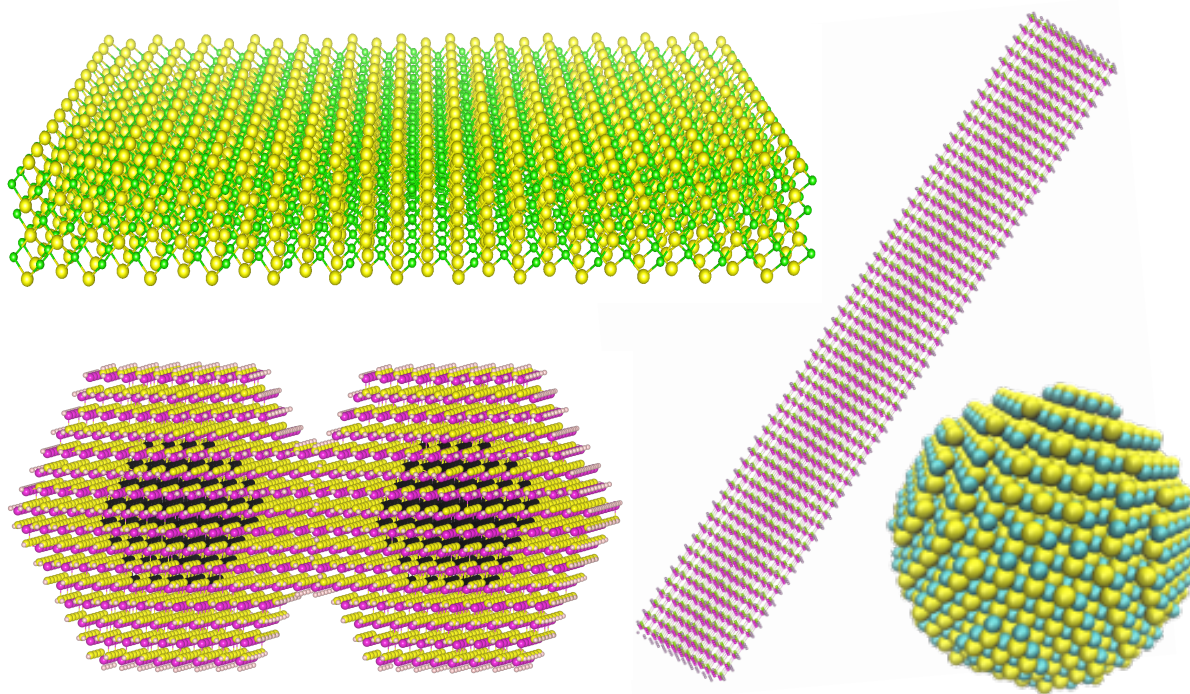
Figure 1.1: Pictorial representation of a colloidal quasi–0D quantum dot (bottom right), quasi–1D nanorod (middle right), quasi–2D nanoplatelet (top left), and core/shell quantum dot dimer (bottom left).

nanomaterials.[26–30] In particular, surface traps (primarily hole traps for II–VI semiconductor nanomaterials) can be very detrimental to the efficiency of nanomaterials (e.g. hole traps reduce quantum yields).[26–28, 31, 32]

In terms of applications, chemically synthesized semiconductor nanomaterials have been promised to revolutionize industries ranging from solar energy and carbon capture to medicine and quantum computing.[15] However, outside of QLED TVs and a few biological applications, a disconnect exists between the potential and practical utility of nanomaterials. This disconnect exists due, in part, to a lack of a detailed understanding of the relationship between the underlying atomic and quantum mechanical structure and the measured efficiency and lifespan of nanomaterial–based solar cells, lasers, photodetectors, carbon capture, bio-sensors, light–emitting diodes and quantum computers. This detailed understanding of nanomaterials requires a deep and broad knowledge of physical chemistry, engineering and quantum optics due to the length scales (single atom to greater than $100,000$ atoms) and timescales (femtosecond to many years) relevant to nanodevices. In the following chapters, the focus will be on II–VI semiconductors (with a primary focus on CdSe), but many of the conclusions are generally applicable and can be applied to other nanosystems (e.g. III–V semiconductors and the Pb–halide perovskites). Furthermore, the focus of this work is on the decay of neutral excitations (i.e. excitons) that are central to nanomaterial–based applica-
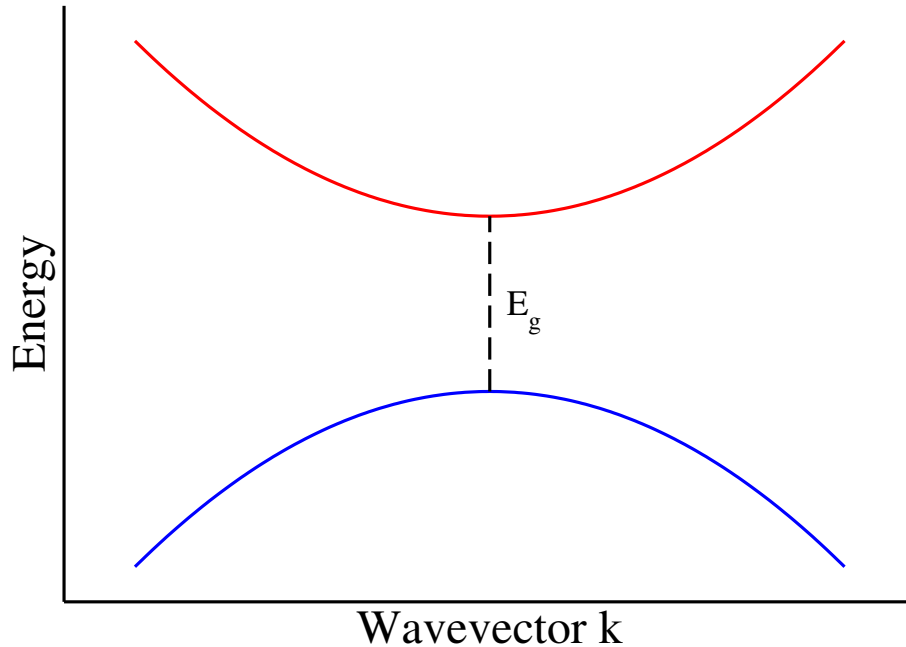
Figure 1.2: A scheme showing a direct band gap bulk material with parabolic bands. The conduction band (electron states) is shown in red and the valence band (hole states) is shown in blue. The band gap (E_{g}) is also labeled.

tions that require light–nanomaterial interactions (e.g. light–emitting diodes, photocatalyst, and lasers).

1.2 Excitons in nanomaterials

Excitons are bound states of a quasielectron (a negatively charged quasiparticle hitherto referred to simply as an electron) and a hole (a positively charged quasiparticle). Excitons in inorganic semiconductors, such as the III–VI and II–VI semiconductors, typically have binding energies on the order to 10 meV in bulk 3D materials and are referred to as Wannier (or Wannier—Mott) excitons.[33] Wannier excitons have exciton Bohr radii ($a_{\mathrm{B,exc}}$) that spread throughout multiple unit cells, this is on contrast to Frenkel excitons for which the electron and hole are localized to the same unit cell (i.e. very small $a_{\mathrm{B,exc}}$). Because this work focuses primarily on confined II–VI semiconductors, the aim of this section will be to introduce Wannier excitons.

In bulk 3D materials, Wannier excitons are often discussed in terms of a hydrogen–like spectral series. This model of excitons is justified from a band structure perspective and is widely used to understand excitons in bulk materials.[34] From a band structure perspective, if one analyzes the dispersion relation (energy versus the wavevector, k) of the low–energy free–carrier (i.e. electron and hole) states it is often reasonable to perform a
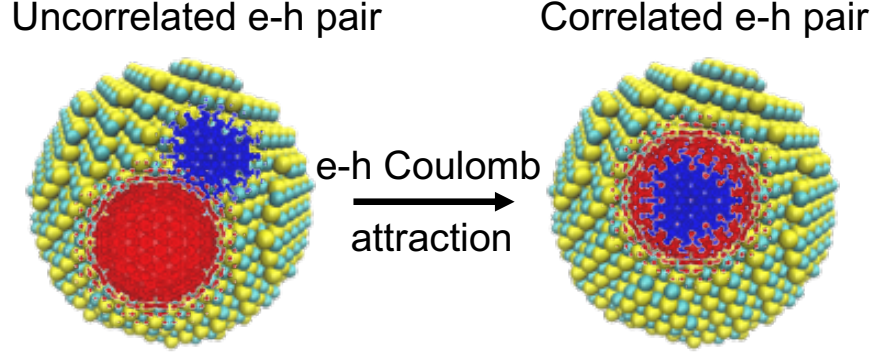
Figure 1.3: Schematic that shows uncorrelated (left) and correlated (right) electron–hole pairs.

parabolic band approximation to describe these low energy excitations within an effective mass approximation (Figure 1.2).[34] Within this approximation, the electron (conduction band) and hole (valence band) are modeled as negatively and positively charged particles with effective masses, m_e^* and m_h^*, respectively. Thus, near the band–edge in the parabolic band approximation,

$$E_{c\mathbf{k}} - E_{v\mathbf{k}} \;\; = \;\; E_\mathrm{g} + \frac{\hbar^2 k^2}{2m_c} - \frac{\hbar^2 k^2}{2m_v} = E_g + \frac{\hbar^2 k^2}{2\mu}, \tag{1.2}$$

where μ is the reduced mass of the electron ($m_e^* = m_c$) and hole ($m_h^* = -m_v$) and E_g is the band gap of the semiconductor.[35] Eq. (1.2) can effectively model the low–energy noninteracting (i.e. free–carrier) electron–hole states. The simplest way to take into account the interaction between the electron and hole is to add a Coulomb attraction term to Eq. (1.2). Doing this results in effective mass equation for Wannier excitons:

$$\left(\frac{\mathbf{p}^2}{2\mu} - \frac{e^2}{\epsilon\, r_\mathrm{e\text{-}h}} \right) \psi_\mathrm{exc} \left(\mathbf{r}_\mathrm{e\text{-}h} \right) \;\; = \;\; E_\mathrm{b} \psi_\mathrm{exc} \left(\mathbf{r}_\mathrm{e\text{-}h} \right). \tag{1.3}$$

In Eq. (1.3), $E_\mathrm{b} = E_\mathrm{exc} - E_\mathrm{g}$ is the exciton binding energy, $\psi_\mathrm{exc} \left(\mathbf{r}_\mathrm{e\text{-}h} \right)$ is its wavefunction with $\mathbf{r}_\mathrm{e\text{-}h} = \mathbf{r}_\mathrm{e} - \mathbf{r}_\mathrm{h}$ being the relative coordinate between the electron and hole, E_exc is the exciton energy, and ϵ is the dielectric constant.[35] The similarity of equation of Eq. (1.2) and that of the hydrogen atom is immediately obvious. Although Eq. (1.2) does miss a few important aspects of excitons,[36,37] the take home message of Eq. (1.2) is that there is an attractive Coulomb interaction between electrons and holes in semiconductors that causes correlations between the particles (Figure 1.3). A focus of the following chapters will be to show how these correlations drastically impact the dynamics of both excitonic and multiexcitonic states in systems of reduced dimensionality.[38]

In confined systems (Figure 1.1), the interaction between electrons and holes is significantly larger than in bulk 3D materials. The enhanced interaction strength in confined

High energy e-h pair   Low energy exciton

Cooling
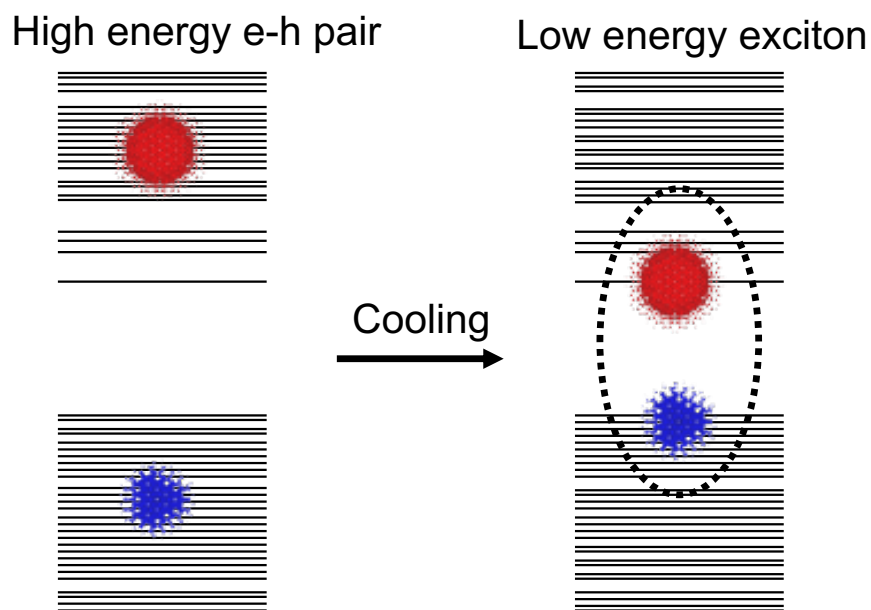
Figure 1.4: Schematic showing the density of states (horizontal lines) of a colloidal nano-material in which a high energy electron (red) and hole (blue) relax (i.e. cool) to form a band–edge exciton (i.e. correlated electron–hole pair as shown by the dashed oval) via phonon emission. This process typically occurs on a picosecond timescale.

systems arises from a multitude of reasons. In QDs, in which there is confinement in all three dimensions, the electron and hole are forced next to one another by the confinement. In NRs and NPLs, the reduced dimensionality results in a reduction in dielectric screening compared to 3D bulk materials which increases the Coulomb attraction between electrons and holes.[39,40] Furthermore, the Coulomb interaction is stronger in systems with less than three dimensions simply due to the geometry and the Jacobian (this is one reason that solving the hydrogen atom in three dimensions is easier than solving the hydrogen atom in lower dimensions). The strong interaction between electrons and holes in confined systems makes understanding their impact on measurable properties (e.g. emission energy) very relevant to understanding the efficiency and rationally designing nanodevices.[41]

Generally speaking, excitons are central to many nanomaterial–based applications because the absorption (emission) of a photon by a nanomaterial results in the generation (loss) of an exciton. Technically speaking, the absorption of a photon with an energy much greater than the optical gap of the nanomaterial can be reasonably well modeled by the creation of an unbound (i.e. uncorrelated) electron–hole pair (left hand side of Figure 1.4). In nanomaterials, these high energy states relax (i.e. cool) to the band–edge of the material with a timescale of approximately 1 ps. During the cooling process, the electron and hole interact with one another and become correlated due to the strong electron–hole interactions in reduced dimensionality systems, as discussed above (right hand side of Figure 1.4).

In summary, the electron–hole interaction is the most common quasiparticle–quasiparticle interaction in NCs. Its consequences range from exciton (a bound electron–hole pair) formation due to the Coulomb attraction between the positively charged hole and negatively charged electron[39] to more exotic physics. For example, the Coulomb interaction between the electron and hole has also been found to be responsible for the bypassing of the Marcus inverted regime in charge transfer systems due to Auger–assisted charge transfer.[42] In these systems, a photon is absorbed by a NC which creates an electron and hole on the NC. Then, the electron (hole) transfers to an electron (hole) accepting ligand and, in order to conserve energy, the hole (electron) transitions into a higher energy state within the NC.[42] This segues into our introduction of biexcitonic states in nanomaterials, where Auger physics is of central importance.[41]

1.3 Biexcitons in nanomaterials

A biexciton is a quasiparticle composed of two electrons and two holes (or, equivalently, two excitons). To begin to understand the importance of biexcitons and how the lack of understanding of quasiparticle–quasiparticle (exciton–exciton in this case) interactions is a roadblock to nanomaterial–based technologies, we will focus this discussion on nanomaterial–based lasers. Lasers are an important example of how this roadblock has impeded energy efficient NC–based technologies. A major issue with traditional lasers is that one cannot tune the wavelength (i.e. energy of the photons) of light emitted without using difficult and energy inefficient conversion processes. In NC–based lasers, the conversion process is simple and much more efficient: one just has to excite NCs which then naturally emits the desired wavelength (size and composition of the nanomaterial can be readily tuned to emit desired wavelengths, as discussed above).[8, 43–46] In fact, this property of NCs to be able to absorb one color of light and efficiently emit a different color light is central to the energy efficiency and color purity of current QLED TVs. Although this conversion process works well for QLED TVs, it does not work well in NC–based lasers because in lasing the material must be able to sustain population inversion – an arduous task for NCs. Population inversion in semiconductor NCs can be readily achieved by absorbing two photons to generate two excitons, but sustaining population inversion is the difficult part in NCs. A major part the work presented here is the development of the first theoretical and computational method capable of predicting quantitatively accurate timescales for which population inversion can be achieved in nanomaterials.

Specifically, each chapter discusses the decay of biexcitonic states via Auger recombination along with the theoretical and computational methods required to predict and understand the lifetime of biexciton Auger recombination for nanomaterials of varying sizes, shapes, compositions, and dimensionality. Auger recombination is the primary mechanism by which multiexcitonic states decay in NCs. As the word Auger signifies, it is a Coulomb mediated scattering process. In detail, Auger recombination is a process in which an electron–hole pair recombines and transfers its energy to an additional quasiparticle (Figure 2.1). This fast

decay channel for biexcitons has a sub–nanosecond timescale and prohibits the population inversion required to make a NC–based laser, as discussed above. Details of how to calculate biexcitonic states and their decay via Auger recombination will be discussed in detail in the following chapters for semiconductor quantum dots (Chapter 2), core/shell quantum dots (Chapter 3), nanorods (Chapter 4), and nanoplatelets (Chapter 5) along with the intricacies that arise in each of these systems due to the dimensionality of the nanosystems.

1.4   Dissertation Objectives

The primary objective of this thesis is to enhance our understanding of electron–hole correlations in semiconductor nanostructures along with the impact that these correlations have on the decay of excitonic and multiexcitonic states through the development and application of new theoretical and computational methods to semiconductor nanostructures of experimental relevance. Secondary objectives of this thesis are to develop computationally efficient algorithms to permit calculations of large nanostructures, validate these methods through close collaboration with experimental groups, and elucidate design rules and principles for nanomaterial–based applications.

A quick example of how these objectives are often intertwined with one another is a study we performed on the attachment of CdSe QDs in close collaboration with the Alivisatos group at UC Berkeley.[31] The atomic attachment of QDs is required to form strongly coupled QD dimers[22] and superlattices.[47] However, the Alivisatos group identified the formation of many defects along the interface, some of which were found to be difficult to remove, using *in situ* high–resolution transmission electron microscopy.[31] To understand the electronic consequences of these defects, we performed atomistic electronic calculations on CdSe QD dimers with the identified defects at the interface. Figure 1.5 shows that both prismatic stacking faults and edge dislocations result in hole traps at the interface. While the electron remains delocalized throughout the dimer when electron–hole interactions are ignored in both defects (panels C and G of Figure 1.5), the attractive Coulomb interaction between the electron and hole results in the electron localizing around the edge dislocation (Figure 1.5H).[31] This finding has important implications on the transport properties of attached CdSe QDs. Specifically, hole transport should be drastically reduced in QD superlattices with either prismatic stacking faults or edge dislocations whereas electron transport will be less impacted by these defects unless holes are localized to edge dislocations as that would result in electron localization as well. This short example of how electron–hole interactions result in the trapping of the electron around the edge dislocation highlights how the inclusion electron–hole correlations can qualitatively impact the conclusions of a calculation.

The major focus of this thesis is that of how electron–hole correlations impact the decay of biexcitonic states, and the interconnectedness of the aforementioned objectives will be evident throughout the detailed discussions of the nonradiative decay of biexcitonic states via Auger recombination. As will be shown in Chapter 2, the development of a new computational method for calculating the decay of biexcitonic states via Auger recombination
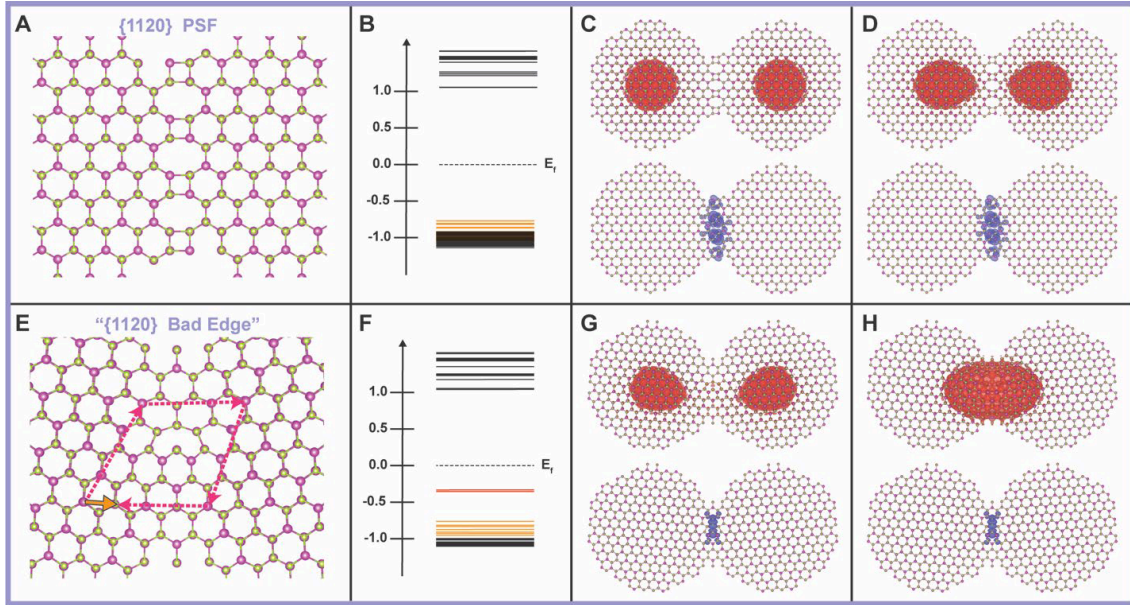
Figure 1.5: Atomistic electronic structure calculations of attached CdSe quantum dots with (A–D) a {11$\bar{2}$0} prismatic stacking fault and (E–H) a {11$\bar{2}$0} edge dislocation interfacial defect. (A, E) The interface of the attached quantum dots are shown. (B, F) Single–particle energy level diagrams (in eV) are shown with the Fermi energy (E_F) shown with a dashed line. Defect–related shallow and deep trap states are represented with orange and red lines, respectively. (C, G, D, H) Electron (red) and hole (blue) probability densities for (C, G) noninteracting (i.e. free–carrier) electron and hole states and (D, H) excitonic (i.e. correlated electron–hole) states.

(which is often the dominant decay channel of biexcitonic states in semiconductor nano-materials) that includes electron–hole correlations will be presented and thoroughly tested against experimental measurements. Because the method presented in Chapter 2 becomes too computationally demanding to be applicable to large nanomaterials, an efficient algorithm with reduced computational cost relative to the algorithm utilized in Chapter 2 is given in Chapter 3. We also take advantage of this efficient algorithm to learn how the timescale of Auger recombination depends on the size and band alignment of core/shell QDs in Chapter 3. In Chapter 4 we show that the electron–hole correlations that lead to exciton formation (Figure 1.3) are critical to understanding biexciton Auger recombination in quasi–1D NRs. These findings have many practical implications to the efficiency of nanomaterial–based applications. For example, we show how a semiconductor NR–metal hybrid nanoparticle synthesized to perform multi–electron photocatalysis can be designed to maximize the photocatalytic efficiency in multiexciton regimes in which Auger recombination typically dominates the dynamics. In Chapter 5, the results of two collaborative studies with the Schaller and Talapin groups that investigate fundamental properties of excitons and

biexcitons in quasi–2D NPLs are presented and discussed.

Chapter 2

Quantum Dots

2.1 Auger recombination in quantum dots

The fast nonradiative decay of multiexcitonic states is a central process to many nanocrystal (NC)–based applications.[3,41] This nonradiative decay occurs primarily via Auger recombination (AR) in which one electron–hole pair recombines by transferring its energy to an additional charge carrier (Figure (2.1)). In some cases, such as light harvesting devices, AR can limit performance by rapidly quenching the photoluminescence[3,48–51] and, as discussed in Chapter 1, destroying the population inversion required for NC–based lasers,[52] while in other cases, such as photodetectors,[53] single photon sources[54] and even for photocatalysis,[55] it can improve performance by providing a source of hot electrons. Therefore, developing a unified framework to describe AR is important from both fundamental and applied perspectives.

In recent years, much effort has been put into – and much success obtained in – the development of synthetic techniques and principles that result in NCs with rationally designed AR lifetimes.[41] The simplest and most well–known approach to increase the AR lifetime is to synthesize giant NCs. This approach works well because the AR lifetime, τ_{AR}, in single–material quantum dots (QDs) obeys the "universal volume scaling law" (i.e., $\tau_{AR,QD} \propto V$ in QDs).[3,16,56,57] However, current theories predict a steeper scaling with the QD volume,[58–60] signifying only a partial understanding of the AR process even in spherical, quasi–0D quantum dots (QDs). In addition to controlling the AR lifetime by changing the system size, many reports have found that an intelligent design of core/shell NCs with sharp or gradual interfaces allows for the AR lifetimes in NCs to be tuned.[60–66] In Chapter 3, we will discuss the scaling of AR lifetimes in core/shell QDs in more detail.

The situation is somewhat more confusing for non–spherical NCs.[4,5,7–9,67–70] The AR lifetime in quasi–1D nanorods (NRs) was reported to scale linearly with the length (L) of the NRs (i.e., $\tau_{AR,NR} \propto L$), but this observation has not been derived from first principles. Recently, it was argued that the AR decay in PbSe NRs has a crossover from cubic to bimolecular scattering as the length of the NR is increased,[69] calling into question the monotonic length dependence. Further complications arise from the difficulty to measure

precisely the AR lifetimes[5] and also to independently control the dimensions of NRs by current synthetic techniques. In fact, it was shown that NRs of equal volume (but differing diameters and lengths) can have AR lifetimes that differ by more than a factor of 2,[68] but whether this indicates a deviation from the volume scaling observed in QDs remains an open question. In Chapter 4, we will address the scaling of AR lifetime in NRs in more detail.

Quasi–2D nanoplatelets (NPLs) appear to provide an example of the breakdown of the volume scaling of AR lifetimes. First off, contradictory results have been reported for the scaling of AR lifetimes with the lateral area (A). She *et al.* showed that the AR lifetimes are independent of A,[8] while recently it was argued to scale linearly with A, attributed to collisions of excitons limited by their spatial diffusion.[9] The scaling of the AR lifetime as a function of the number of monolayers (MLs) was reported to obey a seventh power dependence, $\tau_{AR,NPL} \propto (ML)^7$, in CdSe NPLs.[9] This was rationalized by a simple noninteracting effective mass model.[9] In Chapter 5, we will address the scaling of the AR lifetime in NPLs in more detail.

In order to simplify and better understand the size and dimensionality dependence of AR lifetimes in NCs, a unified theoretical framework for calculating AR lifetimes in quasi–0D, quasi–1D and quasi–2D nanostructures must be developed. Such a development has been hampered by various factors, including limitations resulting from the enormous number of excitonic and biexcitonic states in NCs as well as the difficulties in including electron–hole correlation effects. Indeed, previous theoretical works have relied on a non–atomistic model[58,71] or a noninteracting electron–hole picture, thought to be suitable for strongly confined systems.[58–61,72,73] However, this approach fails to handle the continuous transition from strong to weak confinement regimes as well as nanostructures that have both strong and weak confinement along different dimensions (e.g., weakly confined along the NR axis and strongly confined in the others).

In this chapter, we develop a unified approach for calculating AR lifetimes that is applicable to all degrees of confinement. The approach is based on Fermi's golden rule to couple excitonic with biexcitonic states. Electron–hole correlations are explicitly included in the initial biexcitonic states by solving the Bethe–Salpeter equation (BSE) to obtain correlated electron–hole states which are then used to form the initial biexcitonic states. This procedure captures most of the electron–hole correlation as the exciton binding energy is typically an order of magnitude larger than the biexciton binding energy.[74] Through a study of CdSe QDs of varying dimensions, we show that our approach predicts AR lifetimes in quantitative agreement with experiments whereas the noninteracting formalism often overestimates the AR lifetimes by $1 - 2$ orders of magnitude. The shorter AR lifetimes are a consequence of electron–hole pair localization which increases the Coulomb coupling and thereby the AR rate in the interacting formalism. By comparing the interacting and noninteracting formalisms (Figure 2.1), we also make evident the importance of including electron–hole correlations for the first theoretical postdiction of the observed volume scaling of the AR lifetime in QDs. Interestingly, the transition to the regime where excitonic effects must be included for an accurate AR lifetime calculation occurs at a surprisingly small diameter in CdSe QDs, below the exciton Bohr radius of CdSe. Additionally, we explain the AR lifetime scaling behavior

in terms of the scaling of the Coulomb matrix elements and the density of final states in QDs. The method presented in this chapter is generally applicable to quasi–0D, quasi–1D, quasi–2D and NC heterostructures, as will be demonstrated in the following chapters.

AR involves the coupling of an initial biexcitonic state ($|B\rangle$) of energy E_B to a final excitonic state ($|S\rangle$) of energy E_S via the Coulomb interaction (V). We utilize Fermi's golden rule to calculate the AR lifetime (τ_{AR}) where we average over thermally distributed initial biexcitonic states and sum over all final decay channels into single excitonic states:

$$\tau_{AR}^{-1} = \sum_B \frac{e^{-\beta E_B}}{Z_B} \left[\frac{2\pi}{\hbar} \sum_S |\langle B\,|V|\,S\rangle|^2 \delta\left(E_B - E_S\right) \right]. \tag{2.1}$$

In the above, the delta function $\delta\left(E_B - E_S\right)$ enforces energy conservation between the initial and final states and Z_B is the partition function for biexcitonic states. Note that throughout this work when we compare to experimental values, we use a room temperature β for this Boltzmann weighted average, but we do not include temperature fluctuations in our NC configurations.[75]

A brute force application of Eq. (2.1) for nanostructures is prohibitive for several reasons. First, there is currently no tractable electronic structure method for a fully–correlated biexcitonic state and for excitonic states at high energies. Second, the number of initial and final states that satisfy energy conservation increases rapidly with the system size. For these reasons, computational and theoretical studies of AR in confined nanostructures have relied on a noninteracting formalism to describe $|S\rangle$ and $|B\rangle$:[58–61,71–73]

$$|S\rangle^{(0)} = a_a^\dagger a_i |0\rangle \otimes |\chi_S\rangle \tag{2.2}$$

$$|B\rangle^{(0)} = a_b^\dagger a_j a_c^\dagger a_k |0\rangle \otimes |\chi_B\rangle, \tag{2.3}$$

where the superscript "(0)" signifies a noninteracting picture is used. In the above, $a_a^\dagger$ and a_i are electron creation and annihilation operators in quasiparticle state "a" and "i", respectively. The indexes $a, b, c...$ refer to the quasiparticle electron (unoccupied) states and $i, j, k...$ refer to quasiparticle hole (occupied) states, with corresponding quasiparticle energies ε_a and ε_i. In Eq. (2.3), $|0\rangle$ is the ground state and $|\chi_S\rangle$ and $|\chi_B\rangle$ are the spin parts of the wavefunctions for excitons and biexcitons, respectively. Within the noninteracting formalism, the excitonic and biexcitonic energies are given by $E_S^{(0)} = \varepsilon_a - \varepsilon_i$ and $E_B^{(0)} = \varepsilon_b - \varepsilon_j + \varepsilon_c - \varepsilon_k$, respectively. The AR lifetime takes an explicit form (see the Supporting Information of Ref. 76 for a detailed derivation and discussion of the spin states studied herein) given by:

$$\left(\tau_{AR}^{(0)}\right)^{-1} = \frac{2\pi}{\hbar Z_B^{(0)}} \sum_{bckj} e^{-\beta(\varepsilon_b - \varepsilon_j + \varepsilon_c - \varepsilon_k)} \sum_a |V_{back}|^2 \delta\left(\varepsilon_b + \varepsilon_c - \varepsilon_k - \varepsilon_a\right)$$

$$+ \frac{2\pi}{\hbar Z_B^{(0)}} \sum_{bckj} e^{-\beta(\varepsilon_b - \varepsilon_j + \varepsilon_c - \varepsilon_k)} \sum_i |V_{ijck}|^2 \delta\left(\varepsilon_c - \varepsilon_j - \varepsilon_k + \varepsilon_i\right). \tag{2.4}$$

The first term on the right hand side (rhs) of Eq. (2.4) describes the decay of a negative trion of energy $\varepsilon_b + \varepsilon_c - \varepsilon_k$ into an electron of energy ε_a while one of the holes remains a
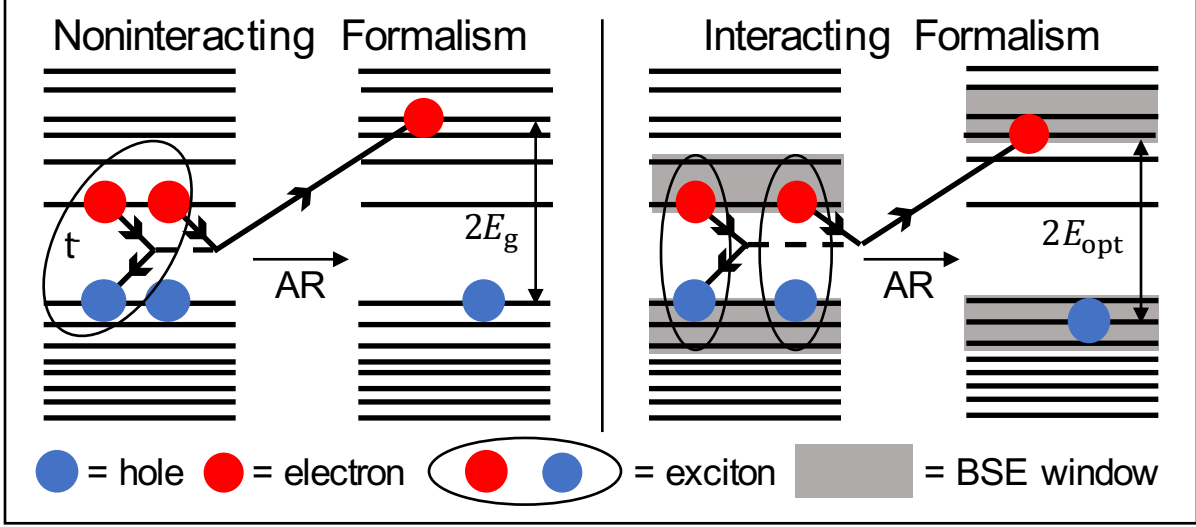
Figure 2.1: Pictorial representations are shown for the electron channel of an Auger recombination (AR) event in the noninteracting (left) and interacting (right) formalisms. The black horizontal lines represent the discrete quasiparticle states of the semiconductor nanostructures. The gray box in the interacting formalism represents the fact that the excitons (correlated electron–hole pairs) are a linear combination of the quasiparticle states within the box that were included in the BSE. E_g is the fundamental gap and E_{opt} is the optical gap. $|B\rangle^{(0)}$ is the initial state in the noninteracting formalism (note that one of the holes is a spectator and the AR process describes a negative trion, t^-, decaying to an excited quasielectron state). $|B\rangle$ is the initial state in the interacting formalism composed of two excitons and all 4 particles are involved in the AR process. The final states in both formalisms are given by $|S\rangle^{(0)}$. The dashed line represents the Coulomb interaction.

spectator (we refer to this as the "electron channel" and it is shown pictorially on the left side of Figure 2.1), and the second term on the rhs of Eq. (2.4) describes the decay of a positive trion of energy $\varepsilon_c - \varepsilon_j - \varepsilon_k$ into a hole of energy ε_i while one of the electrons remains a spectator (we refer to this as the "hole channel"). The explicit form of the Coulomb coupling is then given by:

$$V_{rsut} \;\; = \;\; \iint \frac{\phi_r\left(\mathbf{r}\right)\phi_s\left(\mathbf{r}\right)\phi_u\left(\mathbf{r}'\right)\phi_t\left(\mathbf{r}'\right)}{|\mathbf{r} - \mathbf{r}'|} d^3\mathbf{r}\, d^3\mathbf{r}', \tag{2.5}$$

where $\phi_s\left(\mathbf{r}\right)$ are the quasiparticle states for electrons ($s \in a$) or holes ($s \in i$) and there is no screening – consistent with Ref. 72 and Ref. 77.

As discussed in the introduction, the noninteracting approach is suitable for nanostructures in the very strong confinement regime, where the kinetic energy is large compared to electron–hole interactions. This approach fails, as shown below, for system sizes in the moderate to weak confinement regimes. The inclusion of electron–hole correlations is mainly

of significance in the description of the initial biexcitonic states while for the final excitonic states, the noninteracting framework seems suitable even for weakly confined structures, since the final state describes a highly excited electron–hole pair, above their ionization energy. Therefore, we use a noninteracting description for $|S\rangle$ given by Eq. (2.2), but include electron–hole correlations in the description of the initial biexcitonic state. Motivated by the work of Refaely–Abramson *et al.*,[77] we express the biexcitonic state as two spatially noninteracting but spin–correlated excitons. This is justified since electron–hole correlations are most significant within excitons as reflected by the larger exciton binding energy compared to that of biexcitons.[74] In our interacting approach the biexcitonic states take the form:

$$|B\rangle \;=\; \sum_{b,j}\sum_{c,k} c_{b,j}^{B} c_{c,k}^{B} a_{b}^{\dagger} a_{j} a_{c}^{\dagger} a_{k} |0\rangle \otimes |\chi_{B}\rangle, \tag{2.6}$$

where the coefficients $c_{b,j}^{B}$ are determined by solving the Bethe–Salpeter equation (BSE),[36] as detailed in Ref. 78. The excitonic energy is given by the noninteracting expression, while the biexcitonic energy is now a sum of the exciton energies, each obtained from the BSE. Within the interacting framework, the AR lifetime is given as a sum of electron–dominated (shown pictorially on the right side of Figure 2.1) and hole–dominated contributions:

$$
\begin{aligned}
\tau_{\mathrm{AR}}^{-1} \;=\; & \frac{2\pi}{\hbar Z_{B}} \sum_{B} e^{-\beta E_{B}} \sum_{a,i} \left| \sum_{b,c,k} c_{b,i}^{B} c_{c,k}^{B} V_{back} \right|^{2} \delta\left(E_{B} - \varepsilon_{a} + \varepsilon_{i}\right) \\
& + \frac{2\pi}{\hbar Z_{B}} \sum_{B} e^{-\beta E_{B}} \sum_{a,i} \left| \sum_{j,c,k} c_{a,j}^{B} c_{c,k}^{B} V_{ijck} \right|^{2} \delta\left(E_{B} - \varepsilon_{a} + \varepsilon_{i}\right),
\end{aligned}
\tag{2.7}
$$

where there are *coherent* sums of the Coulomb matrix elements multiplied with the coefficients that were obtained by diagonalizing the Bethe–Salpeter Hamiltonian matrix. Due to the presence of electron–hole interactions, all particles are involved in the AR process in the interacting formalism. For further details regarding the theory and the derivations of the above equations, please consult the Chapter 6 and Ref. 76.

For the implementation of the above frameworks, we chose the semi–empirical pseudopotential method to model the quasiparticle states.[79–82] And because we only need quasiparticle states in specific energy ranges (near the band–edge for the initial biexcitonic states and those that satisfy energy conservation for the final excitonic states), we utilize the filter–diagonalization technique[83,84] to obtain only the required electron and hole eigenstates.[84] Electron–hole correlations were included in the interacting formalism by solving the BSE within the static screening approximation, where the dielectric constant was taken from the work of Wang and Zunger.[80]

For QDs, we calculated the AR lifetimes for seventeen wurtzite CdSe QDs with diameters ranging from $D_{\mathrm{QD}} = 2R_{\mathrm{QD}} = 1.2$ nm ($Cd_{20}Se_{19}$) to $D_{\mathrm{QD}} = 2R_{\mathrm{QD}} = 5.3$ nm ($Cd_{1358}Se_{1360}$). For completeness, we also calculated the fundamental and optical gaps for the CdSe QDs, shown in Figure 2.2. The difference in the fundamental gap and optical gap is the exciton
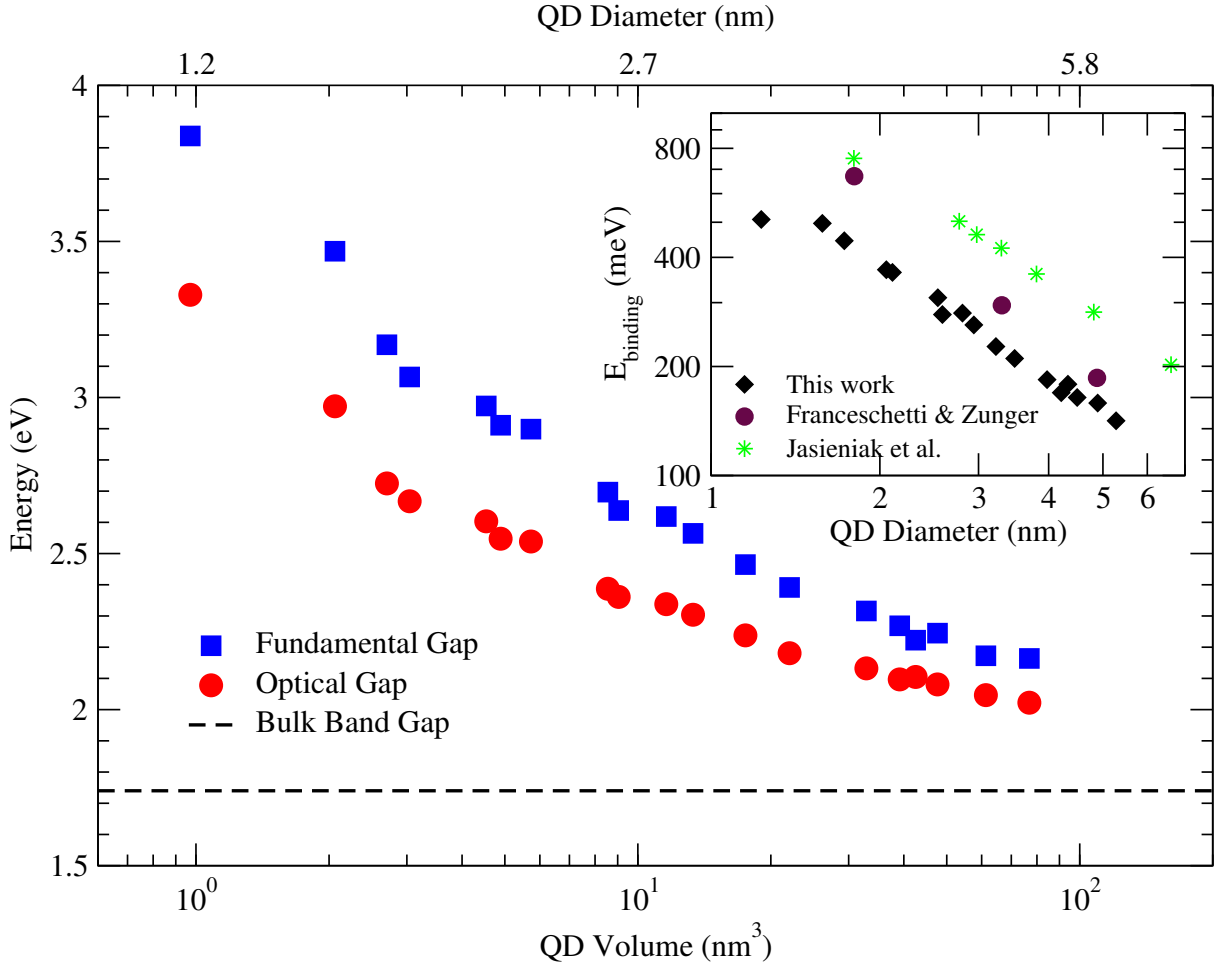
Figure 2.2: Energy gaps (in eV) for the seventeen CdSe QDs. The fundamental gap is shown in blue solid squares and the optical gap is shown in red solid circles. The inset shows the exciton binding energy (the energy difference between the fundamental and optical gaps) which ranges from ~ 500 meV for the smallest QDs to ~ 150 meV for the largest QDs studied here. For comparison, we also show the measured exciton binding energy (green stars, Ref. 1) and calculations based on a semi–empirical pseudopotential model using a perturbative scheme (maroon circles, Ref. 2).

binding energy and is in good agreement with previous studies.[1,2] This suggests that (a) our model is accurate enough to reproduce single– (fundamental gap) and two–particle (optical gap) properties with the simplification of a uniform dielectric screening and (b) that our computational machinery shows mild scaling with the system size, allowing a direct comparison with experiments for realistic NC sizes.

Figure 2.3 displays the AR lifetimes obtained by using both the noninteracting (Eq. (2.4)) and interacting (Eq. (2.7)) formalisms along with experimental[3–5] measurements of the AR
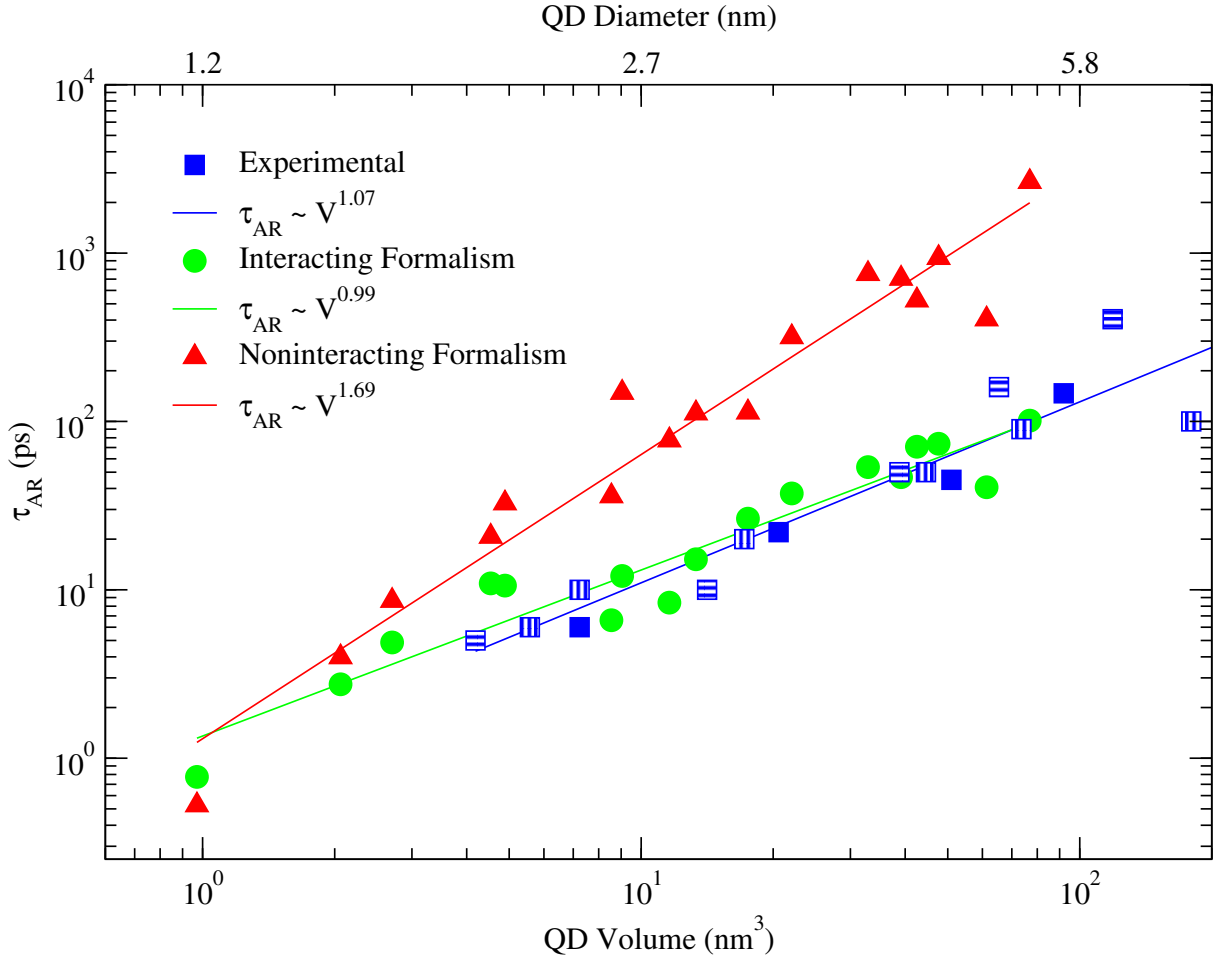
Figure 2.3: AR lifetimes, τ_{AR}, for CdSe QDs as a function of the volume of the QD. Good agreement is observed between the interacting formalism (green circles) and experimental (blue squares: solid,[3] vertical lines[4] and horizontal lines[5]) AR lifetimes for all sizes. On the other hand, the noninteracting formalism (red triangles) deviates from the experimental values for QD volumes > 10 nm³. Power law fits, $\tau_{AR} = a \times V^b$, are also shown for each of the three sets of AR lifetimes.

lifetimes. It is clear that neglecting electron–hole correlations in the initial biexcitonic state is only reasonable in the very strong confinement limit, where $R_{QD} \ll a_B$ (where $a_B = 5.6$ nm is the exciton Bohr radius of CdSe).[85] The noninteracting–based AR lifetimes increase too rapidly as the volume of the QD increases compared to both the interacting formalism and experimentally measured AR lifetimes.

Quantitatively, the computed scaling of the AR lifetime by the noninteracting formalism is $\tau_{AR,QD}^{(0)} \propto V^{1.69}$, which is in contrast to the known volume scaling of the AR lifetime in single material QDs.[3] On the other hand, the volume scaling is accurately captured by the

interacting formalism ($\tau_{\mathrm{AR,QD}} \propto V^{0.99}$), and the overall agreement with the experiments is remarkable. Recall that the previous theoretical studies using a noninteracting formalism for the AR lifetime either studied QDs small enough that the noninteracting formalism was able to relatively accurately predict the volume scaling of the AR lifetime[72] or the theories predicted a stronger dependence on the volume ($\propto V^{5/3}$ to V^2).[58,59] We find that the inclusion of electron–hole interactions has a larger influence on the hole channel than the electron channel. Specifically, the scalings are $\tau_{\mathrm{AR,e}}^{(0)} \propto V^{1.70}$ and $\tau_{\mathrm{AR,h}}^{(0)} \propto V^{1.91}$ in the noninteracting formalism and $\tau_{\mathrm{AR,e}} \propto V^{1.24}$ and $\tau_{\mathrm{AR,h}} \propto V^{0.80}$ in the interacting formalism (Figure 2.5 and Figure 2.6, respectively). It is important to note that the scalings reported for the electron and hole channels in the interacting formalism are not exactly those for a trion (charged exciton) due to coefficients in Eq. (2.7); however, these scalings are in rather good agreement with previous studies on the scaling of AR for negatively charged trions.[59,86]

To understand the origin of the volume scaling of the AR lifetimes for QDs, we start with Fermi's golden rule and, for simplicity, focus on the rate of decay to hot electrons via the electron channel (similar arguments also hold for the hole channel) at zero temperature ($b = c \equiv \ell = $ LUMO and $j \equiv h = $ HOMO) in the noninteracting approach:

$$\left(\tau_{\mathrm{AR,e}}^{(0)}\right)^{-1} = \frac{2\pi}{\hbar} \sum_a |V_{\ell a \ell h}|^2 \, \delta \left(\varepsilon_\ell + \varepsilon_\ell - \varepsilon_h - \varepsilon_a\right), \qquad (2.8)$$

where $\varepsilon_\ell + \varepsilon_\ell - \varepsilon_h = 2E_{\mathrm{g}}$ equals two times the fundamental gap, E_{g}. The scaling of the AR lifetime depends on the scaling of the final density of state and the Coulomb coupling. The former scales linearly with the volume of the NC.[87,88] Determining the scaling of the latter is more involved. Naively, one would predict it to scale with R_{QD}^{-1} due to the Coulomb potential. However, because the final hot electron state is highly oscillatory, reflecting the high kinetic energy of the hot electron, and the initial biexcitonic state is slowly varying, the leading term that scales as R_{QD}^{-1} vanishes. The next term, which can be obtained by invoking the stationary phase approximation, scales as R_{QD}^{-3}.[58] Altogether, these arguments predict an Auger lifetime that is proportional to the volume: $\tau_{\mathrm{AR,e}}^{-1} \propto \left|R_{\mathrm{QD}}^{-3}\right|^2 R_{\mathrm{QD}}^3 \propto R_{\mathrm{QD}}^{-3}$. Similar arguments hold for the scaling of the Auger lifetime in the interacting formalism.

We find, as predicted, that the density of hot electrons and holes scales linearly with the volume of the NCs (top panel, Figure 2.4) in both formalisms. However, the scaling of the average Coulomb coupling squared shows significant deviations from the expected V^{-2} stationary phase result in the noninteracting formalism ($\propto V^{-2.74}$), while in the interacting formalism it scales as expected, $\propto V^{-1.99}$. These different scalings can be rationalized by a more localized electron–hole wavefunction in the interacting case, due to the screened Coulomb electron–hole attraction term in the BSE, leading to more overlap with the wavefunction of the hot electron.

Surprisingly, the noninteracting formalism shows pronounced deviations from the interacting formalism for CdSe QDs with diameters as small as ~ 2.5 nm, much smaller than the exciton Bohr radius ($a_{\mathrm{B}} = 5.6$ nm for CdSe).[85] This was a rather surprising result as all QDs
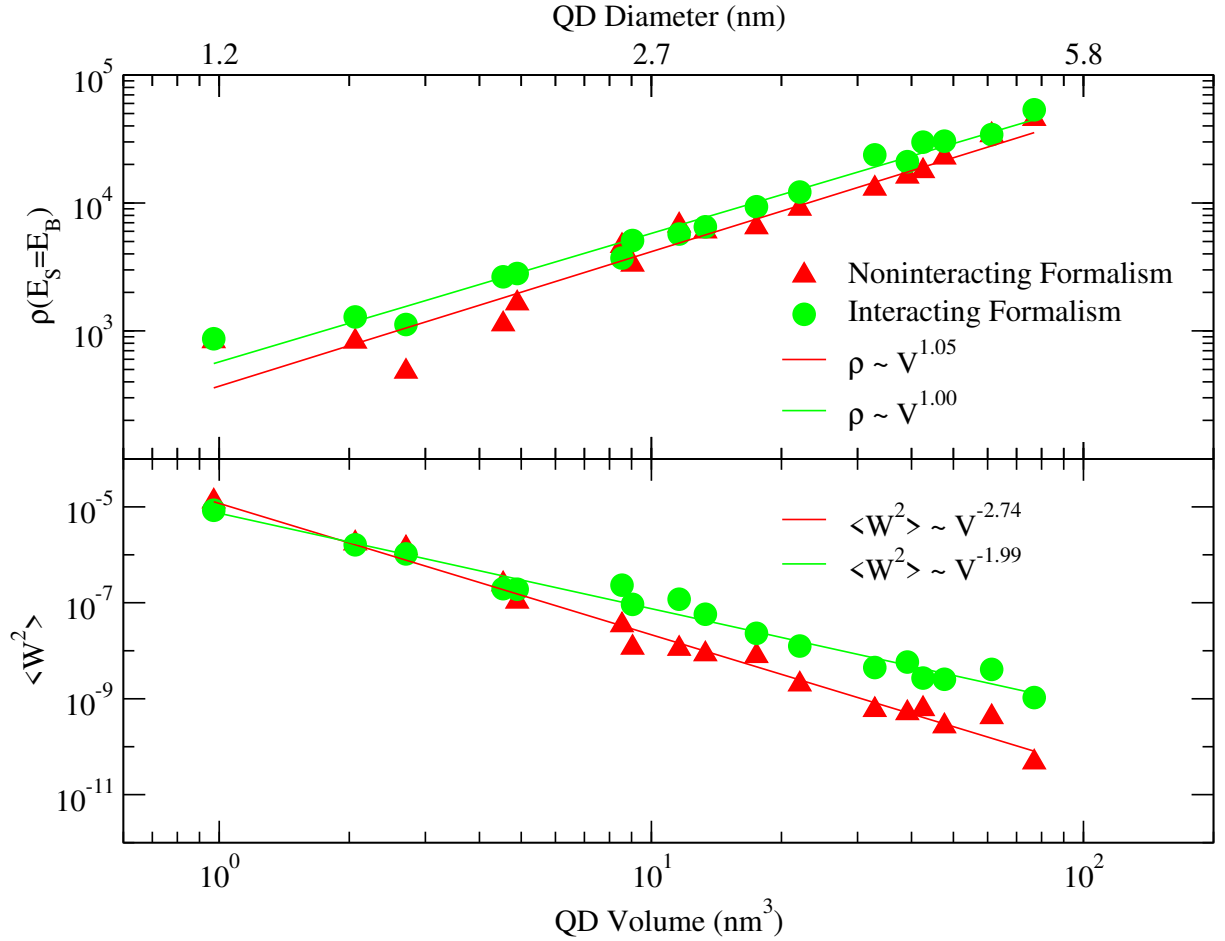
Figure 2.4: The top half shows the density of states at the energy of the hot electron and holes satisfying energy conservation for CdSe QDs as a function of the volume of the QD. The hot electrons (holes) have energies approximately E_{g} above (below) the HOMO (LUMO) in the noninteracting case and in the interacting formalism the hot electrons (holes) have energies approximately E_{opt} above (below) the HOMO (LUMO). The bottom half shows the average of the Coulomb couplings, $\langle W^2 \rangle$, squared to the final states. The noninteracting formalism results are shown as red triangles and the interacting formalism results are shown as green circles. Power law fits, $f(V) = a \times V^b$, are also shown for all sets.

studied here have $R_{\mathrm{QD}} < a_{\mathrm{B}}$, where electron–hole interactions are rather small compared to the confinement kinetic energy (see inset in Figure 2.2).

Figure 2.5 shows the Auger recombination lifetime scaling for the electron channel in both the interacting (red circles) and noninteracting (red triangles) formalisms. And Figure 2.6 shows the Auger recombination lifetime scaling for the hole channel in both the interacting (blue circles) and noninteracting (blue triangles) formalisms. It is seen that the inclusion of electron–hole correlations are important for both channels – having a larger impact on the
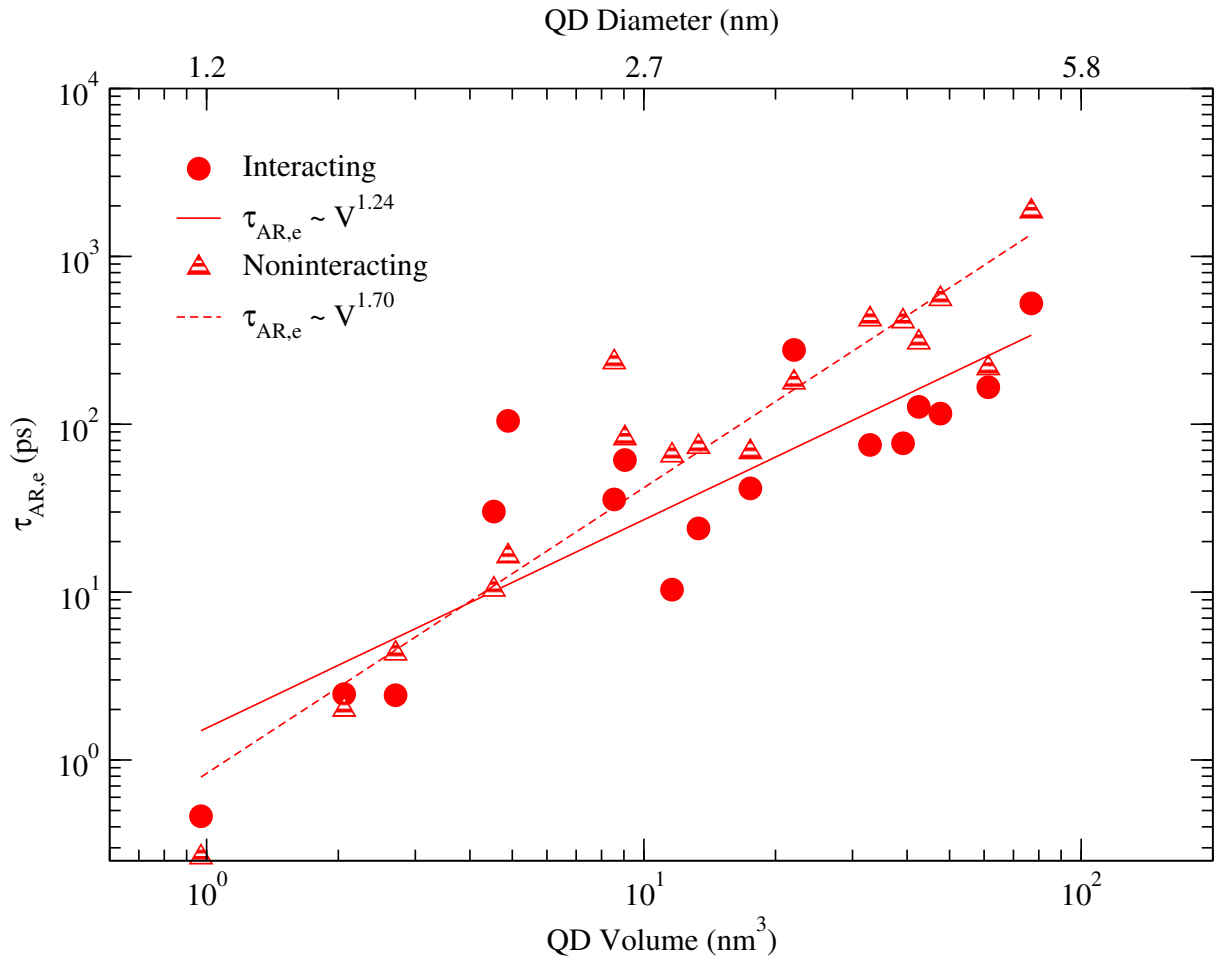
Figure 2.5: AR lifetimes for the electron channel only, $\tau_{\mathrm{AR,e}}$, for CdSe QDs as a function of the volume of the QD. The calculated lifetimes are shown for both the interacting (solid red circles) and noninteracting (stripped red triangles) formalisms are shown. Power law fits, $\tau_{\mathrm{AR,e}} = a \times V^b$ are also shown for both formalisms.
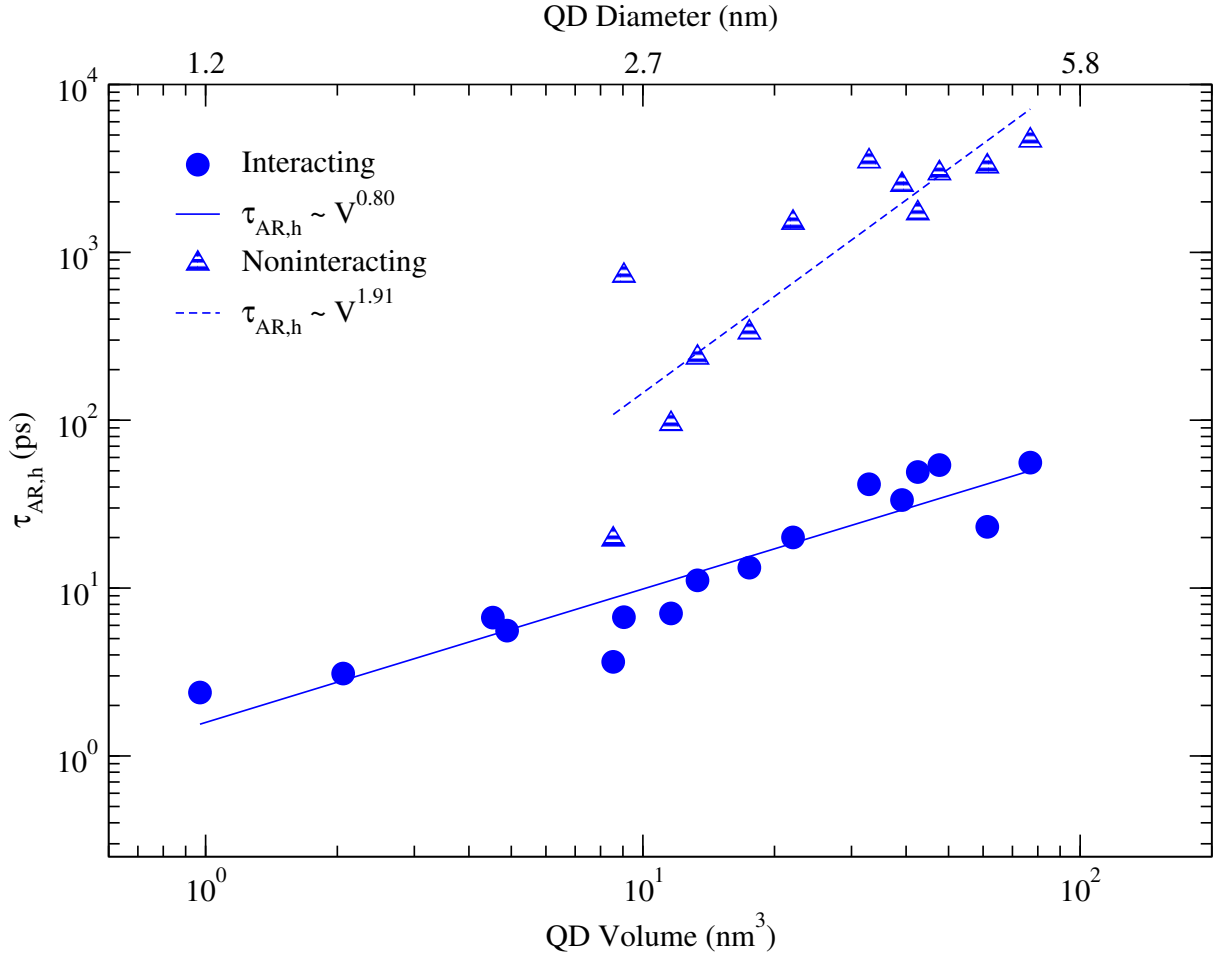
Figure 2.6: AR lifetimes for the hole channel only, $\tau_{\mathrm{AR,h}}$, for CdSe QDs as a function of the volume of the QD. The calculated lifetimes are shown for both the interacting (solid blue circles) and noninteracting (stripped blue triangles) formalisms are shown. Power law fits, $\tau_{\mathrm{AR,h}} = a \times V^b$ are also shown for both formalisms.

hole channel. Additionally, the noninteracting based scaling of the hole channel ($\tau_{\mathrm{AR,e,QD}} \propto V^{1.91}$) is steeper than that of the electron channel ($\tau_{\mathrm{AR,e,QD}} \propto V^{1.70}$) which is consistent with the findings from Ref. 66.

In conclusion, the interacting approach developed here for calculating AR lifetimes in NCs provides a framework that is able to predict quantitatively accurate AR lifetimes in QDs. Our interacting formalism is the first to postdict the experimentally observed linear volume dependence of the AR lifetime in QDs. This result was rationalized by noting that the matrix elements in AR lifetime calculations involve a product of the initial electron and hole states; thus, taking into account electron–hole correlations will have a large impact in regimes where the confinement energy is comparable or smaller than the exciton binding

energy. Electron–hole correlations result in a localization of the pair, thereby, increasing the Coulomb coupling between the initial and final states. Furthermore, the interacting formalism outlined in this chapter constitutes a large step in bringing theoretical studies up to speed with ability of experimentalists to measure AR lifetimes and, in general, multiexciton dynamics. Our approach allows for direct comparisons and joint investigations between theorists and experimentalists as it permits accurate theoretical calculations of AR lifetimes for experimentally relevant nanostructures of any dimensionality and composition. It should be noted that our framework assumes that the excitons scatter coherently; thus, systems in which exciton diffusion is the rate limiting step are currently outside the scope of our approach. In the following chapters, we apply this interacting formalism to study AR in core/shell QDs (Chapter 3), NRs (Chapter 4), and NPLs (Chapter 5).

Chapter 3

Core/Shell Quantum Dots

3.1 Auger recombination in type-I and quasi-type-II core/shell quantum dots

The viability of many semiconductor nanomaterial–based applications relies upon the ability to control multiexcitonic states.[3,41] For example, in typical nanomaterial–based lasers, generating population inversion requires two excitons in the nanosystem and, thus, the properties of the biexcitonic state determine, amongst other factors, the efficiency of the device.[8,46,89,90] In fact, this is arguably the case for other applications such as light–emitting diodes[89,91] and photocatalysts.[55] Therefore, understanding the properties of the biexcitonic state and its decay channels in core/shell QDs is central to improving and further developing many light–induced applications.

One of the major decay channels of the biexcitonic state is Auger recombination (similar to exciton–exciton annihilation), which is a nonradiative process where an electron and hole recombine and transfer their energy to a nearby electron or hole in a Coulomb mediated process (Figure 3.1). Auger recombination is typically is the dominant decay channel of biexcitons in semiconductor nanocrystals as it usually occurs on a sub–nanosecond timescale.

An aspect of biexciton Auger recombination that has drawn much attention over the years is that of how the rate of biexciton Auger recombination decay depends on the size of the nanocrystal.[3,9,16,59,68,76,92,93] For single material colloidal quantum dots (QDs), the linear dependence of the biexciton lifetime with the QD volume has become known as the "universal volume scaling law."[16] Although the size of a single material colloidal QD is a knob that can be tuned to change the biexciton lifetime and, thus, the efficiency of nanodevices that rely on biexcitonic states, changing the size also drastically impacts single exciton properties. On the other hand, heterostructure nanomaterials have many experimentally tunable parameters, including relative size and band alignments between the individual component materials, that can be chosen to optimize the performance of nanodevices. For example, independently tuning the shell thickness and band alignment has resulted in heterostructure nanocrystals with near–unity quantum yields along with promising light–emitting diode and lasing
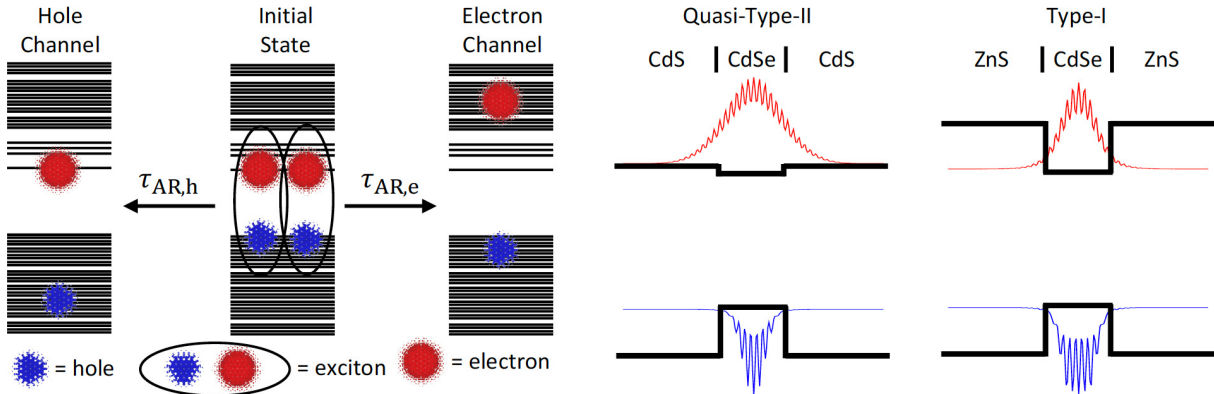
Figure 3.1: (A) Schematic of an Auger recombination event. The initial biexcitonic state is shown as two spatially uncorrelated excitonic states and the final states are shown as unbound electron–hole pairs. The hole (electron) channel on the left (right) shows the hole (electron) receiving a majority of the energy from the recombining exciton. (b) Schematic of the quasi–type–II nature of CdSe/CdS core/shell quantum dots and the type–I nature of CdSe/ZnS core/shell quantum dots. Projected electron (red) and hole (blue) probability densities are shown on top of the band alignment scheme to highlight the differences in electron localization between the two systems.

properties.[23, 56, 89, 91, 94–96] Interestingly, there have been multiple reports that the "universal volume scaling law" does not apply to core/shell QDs.[6, 60, 63, 91, 97–99] Although, significant theoretical progress has been made,[65, 100] particularly on the impact of the sharpness of the core/shell interface on biexciton lifetimes,[61] a quantitatively accurate atomistic electronic structure method has not yet been developed for heterostructure nanomaterials due to the inherently large nature of heterostructure nanosystems and the steep scaling with system size of computing Auger recombination lifetimes.

With this difficulty in mind, we report an efficient, stochastic method for calculating biexciton Auger recombination (AR) lifetimes within Fermi's golden rule suitable for large heterostructure nanosystems and apply it to elucidate the shell thickness dependence of AR in quasi–type–II CdSe/CdS and type–I CdSe/ZnS core/shell QDs (Figure 3.1). The stochastic approach, which also accounts for electron–hole correlations, reduces the scaling with the system size (N) of calculating AR lifetimes from $O\left(N^5\right)$ to $O\left(N^2\right)$ and predicts quantitatively accurate AR lifetimes in comparison to experiments. Additionally, the AR formalism predicts that adding a shell with a quasi–type–II band alignment (CdSe/CdS QDs) results in an increase in the AR lifetime, in agreement with previous experimental and theoretical results,[6, 60, 64, 99, 100] whereas the addition of a shell with a strictly type–I band alignment (CdSe/ZnS QDs) has little impact on the AR lifetime. Lastly, we explain the shell thickness dependencies of the AR lifetimes in terms of the size dependencies of the root–mean–square exciton radius, Coulomb coupling, and density of final states in quasi–type–II CdSe/CdS and type–I CdSe/ZnS core/shell QDs.

AR is a Coulomb mediated process for which an initial biexcitonic state ($|B\rangle$) of energy E_B decays into a final excitonic state ($|S\rangle$) of energy E_S via Coulomb scattering (V). An AR lifetime (τ_{AR}) for a nanomaterial can be calculated using Fermi's golden rule where we average over thermally distributed initial biexcitonic states and sum over all final decay channels into single excitonic states:

$$\tau_{\mathrm{AR}}^{-1} = \sum_B \frac{e^{-\beta E_B}}{Z_B} \left[\frac{2\pi}{\hbar} \sum_S |\langle B\,|V|\,S\rangle|^2 \delta\left(E_B - E_S\right) \right]. \tag{3.1}$$

In the above, the delta function ($\delta\left(E_B - E_S\right)$) enforces energy conservation between the initial and final states and the partition function ($Z_B = \sum_B e^{-\beta E_B}$) is for the initial biexcitonic states (we assume Boltzmann statistics for biexcitons). Utilizing the interacting framework, previously developed by Philbin and Rabani,[76] a deterministic calculation of an AR lifetime can be performed using

$$\tau_{\mathrm{AR}}^{-1} = \frac{2\pi}{\hbar Z_B} \sum_B e^{-\beta E_B} \sum_{a,i} \left| \sum_{b,c,k} c_{b,i}^B c_{c,k}^B V_{abck} \right|^2 \delta\left(E_B - \varepsilon_a + \varepsilon_i\right) \tag{3.2}$$

$$+ \frac{2\pi}{\hbar Z_B} \sum_B e^{-\beta E_B} \sum_{a,i} \left| \sum_{j,c,k} c_{a,j}^B c_{c,k}^B V_{ijck} \right|^2 \delta\left(E_B - \varepsilon_a + \varepsilon_i\right),$$

where the indices $a, b, c...$ refer to the electron (unoccupied) states, $i, j, k...$ refer to the hole (occupied) states with corresponding energies ε_a and ε_i, $r, s, u...$ are general indices, and V_{rsut} is the Coulomb coupling given by

$$V_{rsut} = \iint \frac{\phi_r\left(\mathbf{r}\right) \phi_s\left(\mathbf{r}\right) \phi_u\left(\mathbf{r'}\right) \phi_t\left(\mathbf{r'}\right)}{|\mathbf{r} - \mathbf{r'}|} d^3\mathbf{r}\, d^3\mathbf{r'}. \tag{3.3}$$

The coefficients ($c_{c,k}^B$) in Eq. (3.2) are determined by solving the Bethe–Salpeter equation.[36] For more details, please consult Ref. 76. The above formalism includes spatial correlations within the electron–hole pairs but ignores them between the two excitons[77] and in the final electron–hole pair (Figure 3.1). This approximation for the final state is valid in a majority of nanomaterials as the energy of the final electron–hole pair is approximately twice the optical gap, which is well above the typical exciton binding energy in all semiconductor nanomaterials.[71] In other words, the criteria for being able to approximate the final high energy excitonic state as an uncorrelated electron–hole pair instead of a Wannier or Frenkel exciton is that $E_{\mathrm{opt}} \gg E_{\mathrm{b}}$, where E_{opt} is the optical gap and E_{b} is the exciton binding energy. It was previously shown and discussed in Chapter 2 that this interacting (i.e. exciton–based) AR formalism (Eq. (3.2)) predicts quantitively accurate AR lifetimes for both single material QDs and nanorods.[76] On the other hand, noninteracting formalisms that ignore all electron–hole correlations in the initial biexcitonic state predict neither accurate AR lifetimes nor the scaling of the lifetimes with respect to QD volume except for QDs in the very strong

confinement regime[72] — highlighting the importance of electron–hole correlations and the resulting Wannier exciton formation in semiconductor nanomaterials.[76]

The main drawback of the exciton–based (interacting) AR formalism for calculating AR lifetimes (Eq. (3.2)) is the computational cost. Formally, the steepest scaling involved in Eq. (3.2) is diagonalization of the Bethe–Salpeter Hamiltonian to obtain the coefficients $(c_{c,k}^B)$, which formally scales as $O(N^6)$. However, in practice this takes less than 10% of the computational time for nanomaterials with $\leq 10,000$ atoms because only a few low–lying energy states are required in order to calculate the AR lifetime due to the Boltzmann factors in Eq. (3.2). The majority of the computational time is spent on calculating all of the Coulomb matrix elements, V_{abck} and V_{ijck}, that couple the initial biexcitonic states with the final electron–hole pairs. The number of Coulomb matrix elements that must be calculated scales as $O(N_{e,\text{final}}N_e^2 N_h + N_{h,\text{final}}N_h^2 N_e) \sim O(N^4)$, where $N_{e(h),\text{final}}$ is the number of high energy final electron (hole) states and $N_{e(h)}$ is the number of band–edge electron (hole) states, and the cost of calculating each Coulomb matrix element scales with the number of real–space grid points (N_{grid}) as $O(N_{\text{grid}} \ln N_{\text{grid}})$ to give the overall scaling of $O(N^5)$. This limits the application of Eq. (3.2) to relatively small systems ($\leq 1,000$ atoms).

To reduce the computational effort and scaling of the rate limiting step, we employ a plane–wave stochastic representation of the Coulomb operator:[101]

$$V_{rsut} \approx \left\langle R_{rs}^\zeta R_{ut}^\zeta \right\rangle_\zeta \tag{3.4}$$

where the notation $\langle ... \rangle_\zeta$ denotes an average over N_s stochastic orbitals (defined below),

$$R_{rs}^\zeta = \int \phi_r^*(\mathbf{r}) \phi_s^*(\mathbf{r}) \theta^\zeta(\mathbf{r}) \, d^3\mathbf{r}, \tag{3.5}$$

and $\theta^\zeta(\mathbf{r})$ is a stochastic representation of the Coulomb integral given by

$$\theta^\zeta(\mathbf{r}) = \frac{1}{(2\pi)^3} \int d\mathbf{k} \sqrt{\widetilde{u}_C(\mathbf{k})} \, e^{i\varphi(\mathbf{k})} \, e^{i\mathbf{k}\cdot\mathbf{r}}. \tag{3.6}$$

In the above equations, $\varphi(\mathbf{k})$ is a random phase between 0 and 2π at each k–space grid point, $\widetilde{u}_C(\mathbf{k}) = \frac{4\pi}{k^2}$ is the Fourier transform of the Coulomb potential, and the stochastic orbitals ($\theta^\zeta(\mathbf{r})$) are indexed by ζ. By inserting Eq. (3.4) into Eq. (3.2), we obtain

$$\tau_{\text{AR}}^{-1} = \tau_{\text{AR,e}}^{-1} + \tau_{\text{AR,h}}^{-1} \tag{3.7}$$

$$\tau_{\text{AR,e}}^{-1} = \frac{2\pi}{\hbar Z_B} \sum_B e^{-\beta E_B} \sum_{a,i} \left\langle \sum_b c_{b,i}^B R_{ab}^{\zeta'} \sum_{c,k} c_{c,k}^B R_{ck}^{\zeta'} \right\rangle_{\zeta'}^* \left\langle \sum_b c_{b,i}^B R_{ab}^\zeta \sum_{c,k} c_{c,k}^B R_{ck}^\zeta \right\rangle_\zeta \delta(E_B - \varepsilon_a + \varepsilon_i)$$

$$\tau_{\text{AR,h}}^{-1} = \frac{2\pi}{\hbar Z_B} \sum_B e^{-\beta E_B} \sum_{a,i} \left\langle \sum_j c_{a,j}^B R_{ij}^{\zeta'} \sum_{c,k} c_{c,k}^B R_{ck}^{\zeta'} \right\rangle_{\zeta'}^* \left\langle \sum_j c_{a,j}^B R_{ij}^\zeta \sum_{c,k} c_{c,k}^B R_{ck}^\zeta \right\rangle_\zeta \delta(E_B - \varepsilon_a + \varepsilon_i),$$

where $\tau_{\mathrm{AR,e}}$ and $\tau_{\mathrm{AR,h}}$ are the lifetimes for the electron and hole channels, respectively (Figure 3.1). The calculation of an AR lifetime using Eq. (3.7) scales as $O\left(N^3\right)$.

To further reduce the computational scaling and complexity, we utilize the stochastic resolution of the identity[102, 103] within the subspace of the final high energy electron and hole parts of the Hamiltonian. In simpler terms, we sample the final high energy electron and hole states in order to reduce the scaling with number of final excitonic states. Thus, we arrive at a general expression for calculating AR lifetimes of semiconductor nanomaterials using an efficient, doubly stochastic formulation of the interacting (exciton–based) AR formalism

$$\tau_{\mathrm{AR}}^{-1} = \tau_{\mathrm{AR,e}}^{-1} + \tau_{\mathrm{AR,h}}^{-1} \tag{3.8}$$

$$\tau_{\mathrm{AR,e}}^{-1} = \frac{2\pi}{\hbar Z_B} \sum_B e^{-\beta E_B} \left\langle \left\langle \left(\sum_b c_{b,i^A}^B R_{\theta^A b}^{\zeta'} \sum_{c,k} c_{c,k}^B R_{ck}^{\zeta'} \right)^* \left\langle \sum_b c_{b,i^A}^B R_{\theta^A b}^{\zeta} \sum_{c,k} c_{c,k}^B R_{ck}^{\zeta} \right\rangle_{\zeta'} \right\rangle_{\zeta} \right\rangle_A$$

$$\tau_{\mathrm{AR,h}}^{-1} = \frac{2\pi}{\hbar Z_B} \sum_B e^{-\beta E_B} \left\langle \left\langle \left(\sum_j c_{a^I,j}^B R_{\theta^I j}^{\zeta'} \sum_{c,k} c_{c,k}^B R_{ck}^{\zeta'} \right)^* \left\langle \sum_j c_{a^I,j}^B R_{\theta^I j}^{\zeta} \sum_{c,k} c_{c,k}^B R_{ck}^{\zeta} \right\rangle_{\zeta'} \right\rangle_{\zeta} \right\rangle_I,$$

where the indices θ^A, i^A and a^I, θ^I in Eq. (3.8) are sampled final states from the complete set of single excitonic states (a, i pairs) in Eq. (3.7). Energy conservation in Eq. (3.8) has been taken into account when forming the stochastic orbitals that sample the final excitonic states, namely, we only sample states that preserve energy. The computational cost of Eq. (3.8) is $O\left(N^2\right)$. This scaling does assume that the number of stochastic orbitals required to properly converge the calculations does not increase with the system size, which has shown to be true for a variety of electronic structure methods.[88, 102–105] Another beneficial feature of Eq. (3.8) is that it is embarrassingly parallel over all sets of stochastic orbitals. The speedup that arises from using Eq. (3.8) instead of Eq. (3.2) ranges from ~ 5 for QDs with $1,000$ atoms to greater than $1,000$ for QDs with $10,000$ atoms. This speedup made the study of the large core/shell QDs presented in the remainder of this chapter possible.

We have implemented the above equations using the semi–empirical pseudopotential method to model the electron and hole states.[72, 79–81] We utilized the filter–diagonalization technique[83, 84] to selectively calculate the low energy electron and hole states required to accurately describe the excitonic states that compose the initial biexcitonic state and the high energy electron and hole states that satisfy energy conservation. The Bethe–Salpeter equation[36] was solved within the static screening approximation. And all electronic structure calculations were performed using the minimum energy atomic configuration obtained via molecular dynamic minimization[106] of the heterostructure QDs. This computational scheme has been shown to predict quantitatively accurate single excitonic properties (e.g. optical gap and emission polarizations) and accurately takes into account the important effects of strain in heterostructure nanomaterials that arise from the lattice mismatch between core and shell materials.[23, 95]

Figure 3.2 displays the calculated AR lifetimes using Eq. (3.8) for the $d_{\mathrm{core}} = 3.8$ nm CdSe/CdS QDs along with the experimentally measured AR lifetimes[6] and AR lifetimes
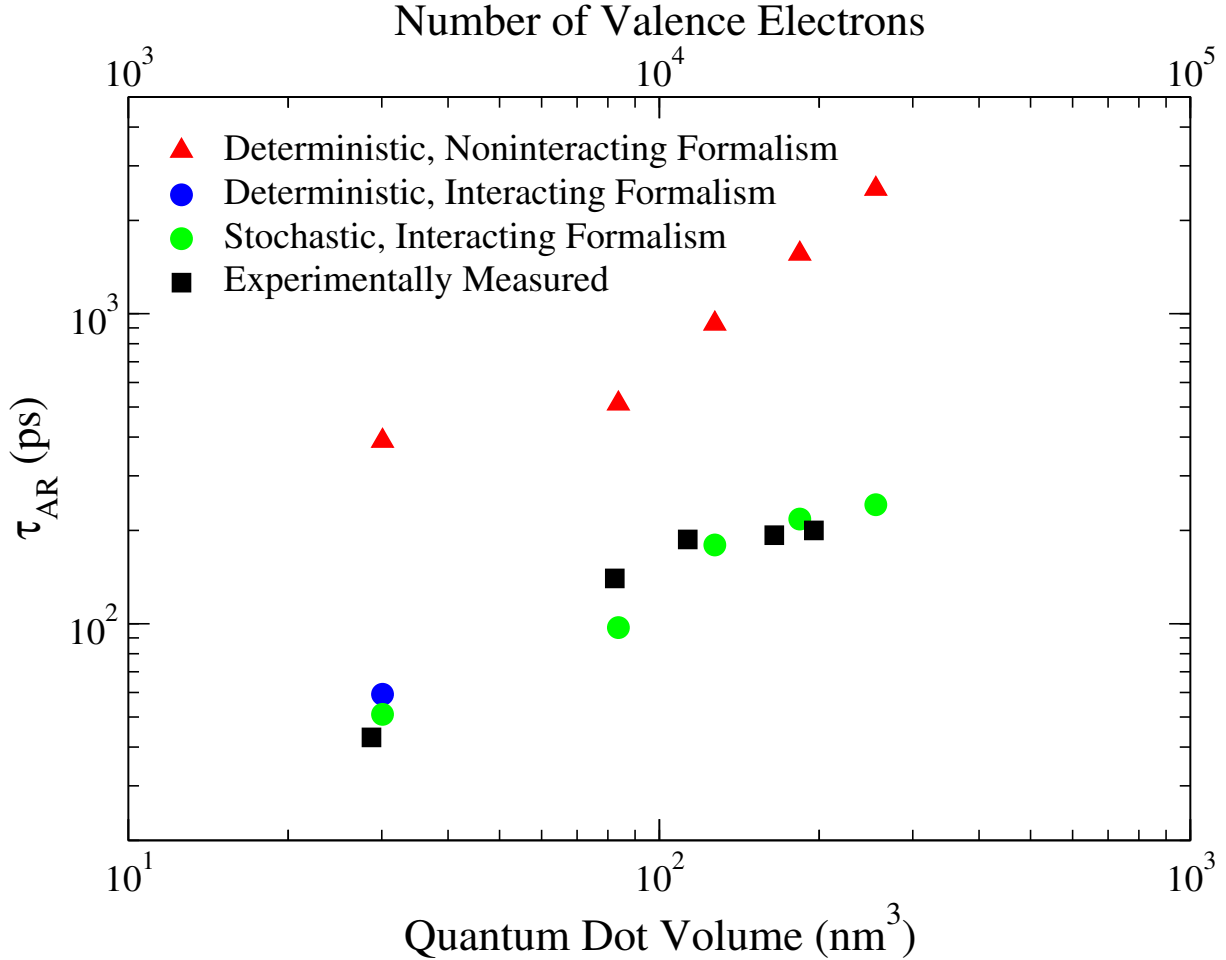
Figure 3.2: Comparison of Auger recombination lifetimes (τ_{AR}) that have been experimentally measured[6] (black), calculated using the deterministic interacting formalism (blue), stochastic formulation of the interacting formalism (green), and the deterministic formulation of the noninteracting formalism (red) of CdSe/CdS core/shell quantum dots with a CdSe core diameter of 3.8 nm and varying number of CdS shell monolayers.

calculated using a noninteracting, free carrier–based formalism.[72] Quantitative agreement with the experimental measurements on similarly sized CdSe/CdS QDs is observed when Eq. (3.8) is used. It is important to note that all of the core/shell QDs studied in this work have sharp core/shell interfaces.[99] In other words, there is no alloying region between the core and shell materials that is known to have important consequences on AR lifetimes.[61,63,65] The quantitative agreement shows the generality of the interacting (exciton–based) AR formalism for predicting quantitatively accurate AR lifetimes in nanomaterials. It is worthwhile to note that a noninteracting (free–carrier based) AR formalism predicts incorrect AR lifetimes in core/shell QDs, similar to the single material case.[76]
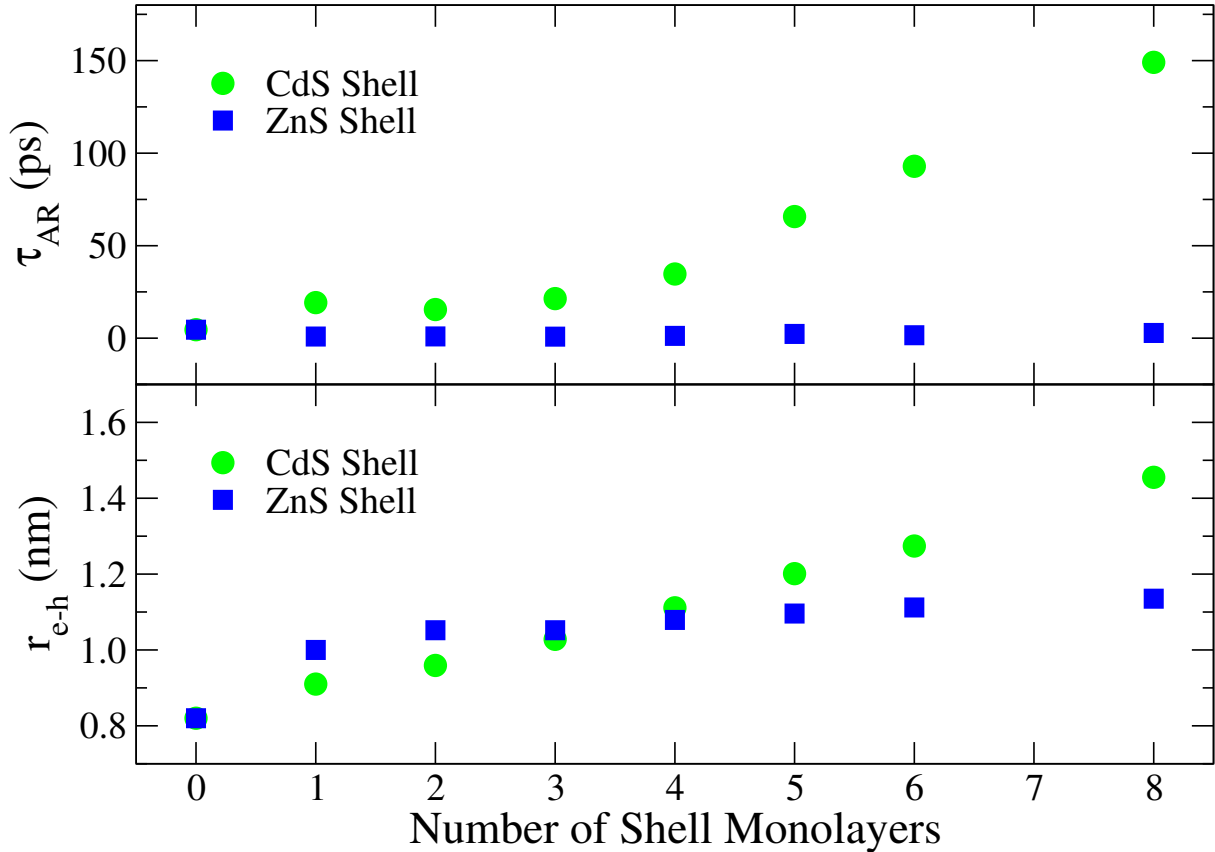
Figure 3.3: Auger recombination lifetimes (top) and root–mean–square exciton radii ($r_{e\text{-}h} = \sqrt{\langle r_{e\text{-}h}^2 \rangle}$), bottom) of CdSe/CdS (green) and CdSe/ZnS (blue) core/shell quantum dots as a function of the number CdS and ZnS shell monolayers, respectively, for a CdSe core diameter of 2.2 nm.

Figure 3.3 summarizes a main result of this work. The top panel of Figure 3.3 compares calculated AR lifetimes for CdSe cores with a diameter of 2.2 nm ($d_{\text{core}} = 2.2$ nm) as a function of the number of shell monolayers (MLs) for both CdS and ZnS from 0 MLs to up to 8 MLs. This constitutes a range of nanocrystal sizes from approximately 200 atoms ($V_{\text{QD}} \sim 5$ nm^3) to nearly 10,000 atoms ($V_{\text{QD}} \sim 350$ nm^3). Figure 3.3 highlights the dramatically different impact that growing a quasi–type–II shell (CdS) has on the AR lifetime compared to growing a type–I (ZnS) shell on a QD core (CdSe). Specifically, the addition of more and more CdS MLs leads to the AR lifetime increasing from ~ 5 ps for the 0 ML QD to ~ 35 ps and ~ 150 ps upon addition of 4 and 8 MLs of CdS, respectively, for the $d_{\text{core}} = 2.2$ nm CdSe QD core. On the other hand, for the same CdSe core, the addition of 4 and 8 MLs of ZnS does not lead to an increase in the AR lifetime.

In order to understand the vastly different shell thickness dependencies of the AR lifetimes between CdSe/CdS and CdSe/ZnS QDs, we plot the root–mean–square exciton radius

$(\sqrt{\langle r_{\text{e-h}}^2 \rangle}$ where $r_{\text{e-h}}$ is the electron–hole radial coordinate)[107] as a function of the number of shell MLs for both series of core/shell QDs in the bottom panel of Figure 3.3. For CdSe/CdS QDs, the root–mean–square exciton radius systematically increases with the number of shell MLs. On the other hand, for CdSe/ZnS QDs there is an increase upon adding the first ZnS layer, but then the addition of more and more ZnS MLs barely changes the root–mean–square exciton radius. Specifically, the root–mean–square exciton radius increases from 1.11 nm to 1.46 nm upon going from 4 MLs to 8 MLs of CdS but only increases from 1.08 nm to 1.14 nm upon going from 4 MLs to 8 MLs of ZnS for the same $d_{\text{core}} = 2.2$ nm CdSe core (bottom panel of Figure 3.3).

These different dependencies of the AR lifetime and root–mean–square exciton radius with shell thickness are a direct consequence of the quasi–type–II[6,78] and type–I nature of the CdS and ZnS shells, respectively. Figure 3.4 shows the hole and electron carrier densities of the lowest energy excitonic state (i.e. electron–hole interactions have been included) projected onto the x–axis of the core/shell QDs for the $d_{\text{core}} = 2.2$ nm CdSe QD cores with 0 MLs, 4 MLs and 8 MLs of shell. For CdSe/CdS (left panels of Figure 3.4), the quasi–type–II nature can be observed as the projected hole density remains confined to the CdSe core for all shell thicknesses while the electron density continuously spreads out into the CdS shell. In contrast, both the hole and electron densities remain confined to the CdSe core in CdSe/ZnS core/shell QDs, highlighting the type–I band alignment of CdSe/ZnS core/shell QDs (right panels of Figure 3.4). The impact of the electron spreading out into the CdS shell and, thus, increasing the root–mean–square exciton radius in larger CdS shell nanocrystals leads to a decrease in the Coulomb coupling involved in AR calculations. This result can be understood by noting that the larger the electron and hole wavefunctions overlap the larger the Coulomb matrix elements, as the product $\phi_c(\mathbf{r}')\phi_k(\mathbf{r}')$ where $\phi_c(\mathbf{r}')$ and $\phi_k(\mathbf{r}')$ are wavefunctions for an initial electron and hole, respectively, arises in the Coulomb coupling (Eq. (3.3)).

The type–I band alignment of CdSe/ZnS core/shell QDs results in the addition of ZnS MLs barely changing the root–mean–square exciton radius and not increasing the AR lifetime. Surprisingly, the AR lifetimes for all CdSe/ZnS core/shell QDs are slightly shorter, with lifetimes of ~ 2 ps, compared to the ~ 5 ps AR lifetime for the bare CdSe core (Figure 3.3). To elucidate whether or not the compressive strain of the ZnS shell causes the decrease of the AR lifetime, we performed AR lifetimes calculations on strained CdSe cores. Specifically, we performed molecular dynamics based structural minimizations with ZnS shells and then removed the ZnS shells before performing the electronic structure calculations. This procedure resulted in compressively strained CdSe QDs,[23] where the degree of compressive strain was related to the number of ZnS MLs that were present during molecular dynamics minimization (Table 6.6). Our calculations on this series of CdSe QDs show that the AR lifetime decreases from ~ 5 ps to ~ 2 ps upon increasing the strain on the CdSe QD (Table 6.7). Interestingly, the AR lifetime decreasing by $\sim 250\%$ upon adding strain to the CdSe QD is much greater than would be expected due to just a volumetric change as the compressive strain only changes the CdSe QD volume by $\sim 10\%$. We were able to trace the decrease of the AR lifetime to a decrease in the hole channel AR lifetime. Furthermore, the decrease of the hole channel AR lifetime was caused by an increase in the average Coulomb coupling
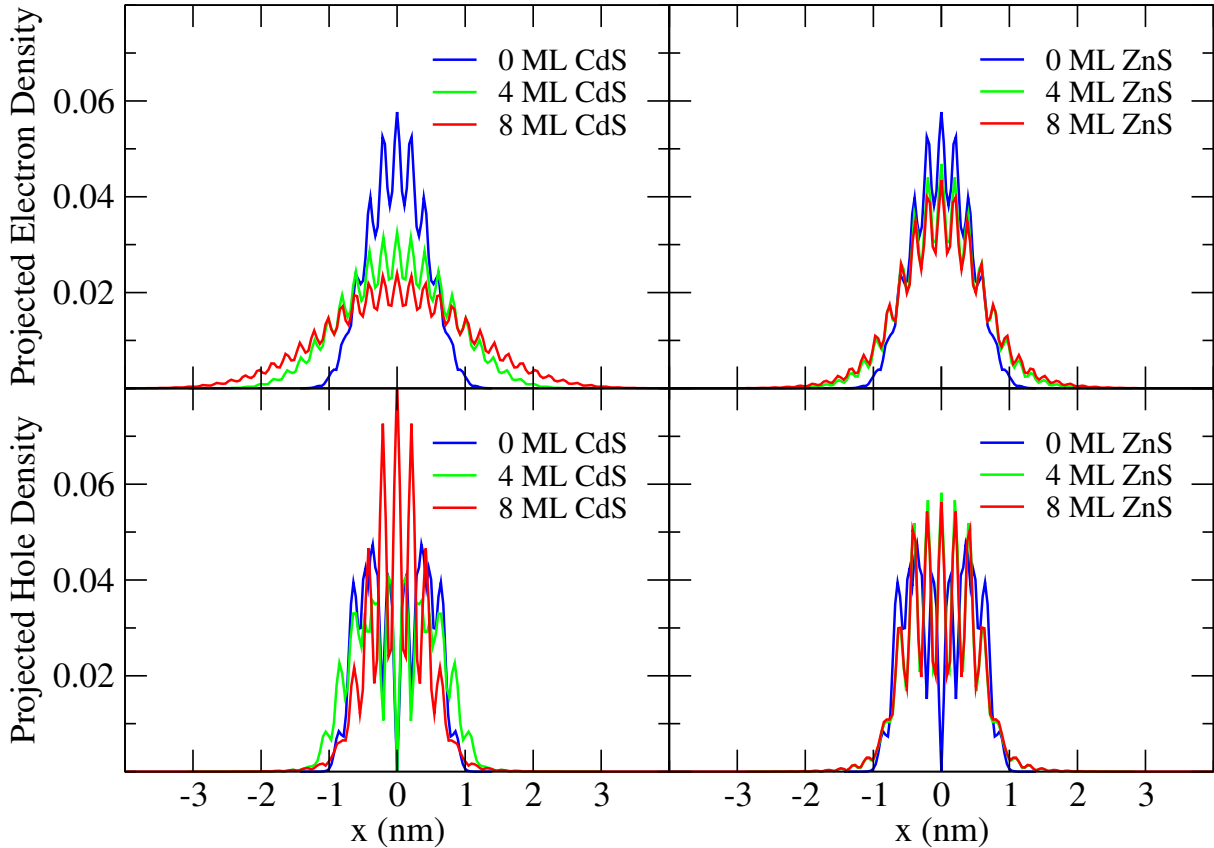
Figure 3.4: Hole and electron carrier densities of the lowest energy excitonic state for a series of shell thicknesses for CdSe/CdS and CdSe/ZnS core/shell QDs with a CdSe core diameter of 2.2 nm.

matrix elements (V_{ijck}) of the hole channel and not by any substantial changes in the density of final states (Table 6.8). Thus, it appears that the hole channel is more sensitive to stress induced structural changes. And this suggests it is worthwhile to perform more comprehensive studies on the impact of strain on AR lifetimes, as strain may be playing a role in other nonmonotonic dependencies of AR in core/shell nanomaterials.[98] That being said, we do note that this is a rather small change of the AR lifetime and experimental confirmation of this decrease in the AR lifetime upon ZnS shell growth on QDs would likely be impeded by inhomogeneous broadening and alloying of the core/shell interface.

The goals of this chapter were to elucidate how biexciton Auger recombination in colloidal core/shell QDs can be accurately modeled and efficiently computed, and to uncover some of the underlying physics of excitons and biexcitons in core/shell QDs by testing different approximations. In order to achieve these goals, we developed a stochastic computational scheme for calculating the nonradiative decay rate of biexcitonic states. This efficient, stochastic method for calculating Auger recombination lifetimes presented in this

chapter is general and can be used for any confined nanomaterial. In fact, we utilize it in Chapter 5 to calculate Auger recombination lifetimes in CdSe NPLs. We also utilized this efficient method for calculating quantitatively accurate biexciton Auger recombination lifetimes within an interacting (exciton–based) formalism to elucidate the different impact of growing quasi–type–II (CdS) and type–I (ZnS) shells on QD cores (CdSe). Specifically, we showed that the Auger recombination lifetime monotonically increases as the number of quasi–type–II shell monolayers increases whereas the Auger recombination lifetime is mainly unchanged upon the addition of type–I shells.

3.2   Impact of strain in core/shell nanomaterials

The importance of strain in core/shell QDs has been discussed in detail in many papers.[108,109] The lattice mismatch between CdSe and CdS causes strain in both lattices in their heterostructures. An interesting finding is that if one begins with a CdSe core and grows a CdS shell around the CdSe core that the shape (i.e. dimensionality) of the CdSe core qualitatively changes the impact that strain has on the emission energy (i.e. optical gap).[23] A comparative study between CdSe/CdS QDs and CdSe/CdS NPLs highlights how growing a quasi–type–II shell (Figure 3.1) with a smaller lattice constant (the lattice constant of CdS is approximately 10% smaller than that of CdSe) impacts the emission energy.

To gain quantitative insights on the interplay of strain and confinement in QDs and NPLs, we have calculated the lowest excitonic state for a series of CdSe/CdS core/shell QDs (3.5 nm diameter CdSe cores) and NPLs (4 ML thick CdSe cores) with different shell thicknesses. Calculations were performed within the semi–empirical pseudopotential model combined with a static approximation to the Bethe–Salpeter equation with a dielectric constant of $\epsilon = 6$.[78] To this end, we first compared the experimental emission energies with the optical gaps from our calculations for a series of core/shell CdSe/CdS QDs and NPLs with thicknesses ranging from 0 MLs to 4 MLs. In these calculations, we first built the heterostructures with the lattice constant of CdSe and then minimized the structure using molecular dynamics to obtain the lowest energy configuration (details of the configurations are given in Chapter 6). We found that the calculated optical gap of the 3.5 nm CdSe QD was 2.20 eV for 0 ML CdS, which reduced down to 2.11 eV after addition of a 4 ML thick CdS shell; the red–shift of 97 meV (Figure 3.5) is in quantitative agreement with the experimental results.[23] Similarly, we found good agreement with experiments for nCdS/4CdSe/ nCdS NPLs; the optical gap red–shifted by 446 meV when going from n = 0 to n = 4 , where n is the number of CdS shell MLs.[23]

In order to disentangle the contributions from strain and carrier delocalization, we performed molecular dynamics (MD) based minimization with 4 MLs of CdS and then removed the CdS shell before performing the electronic structure calculation. In other words, we performed calculations of just the CdSe cores but for the atom positions as if there were a 4 ML thick CdS shell, and these data points are labeled as "strained QD" and "strained NPL" in Figure 3.5. These structures would, thus, not be able to delocalize the carrier wave
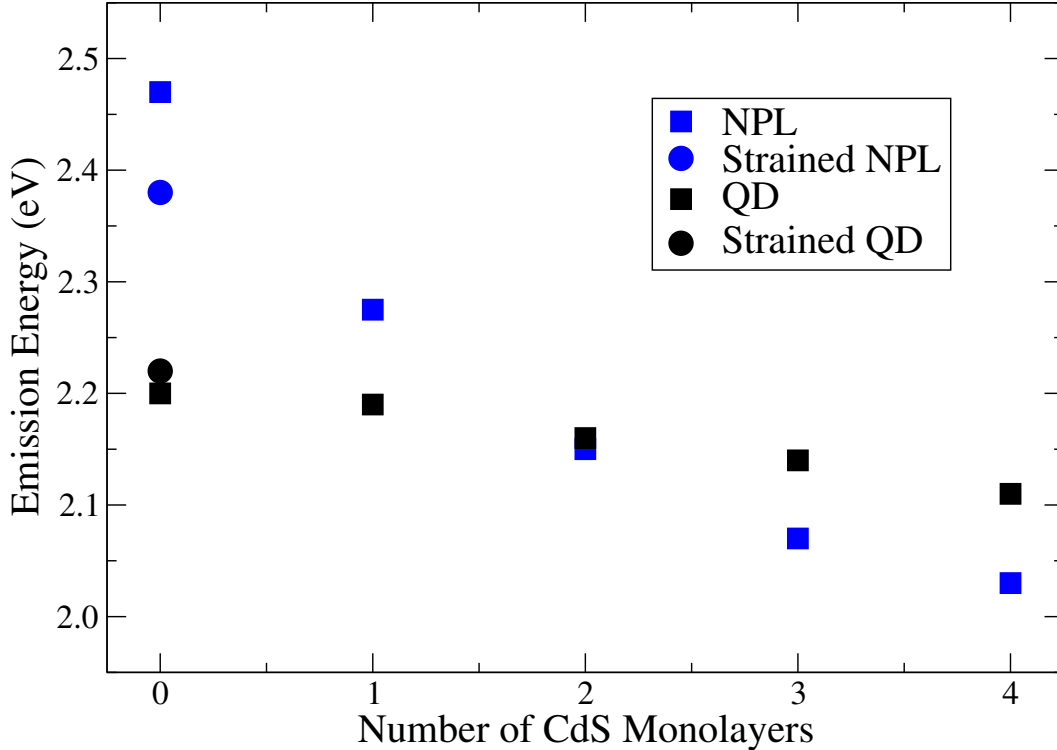
Figure 3.5: Calculated optical gaps of 4 ML CdSe NPLs and 3.5 nm diameter CdSe QDs as a function of the number of monolayers of CdS shell.

functions into the shell, but will have the influence of the strain induced onto the CdSe core by the shell. Expectedly, the isotropic strain in core/shell QDs resulted in a compression of the core in all dimensions, whereas the anisotropic strain in the NPL resulted in less compression because the CdSe can expand in the axial direction (Table 3.1).

Specifically, we calculated averaged lattice constant along the lateral plane (a_x and a_y) and axial (a_z) dimensions for both the CdSe core in the CdSe/CdS QDs and NPLs after MD minimization. The results of this analysis are shown in Table 3.1. We find that, as expected, $a_x = a_y = a_z$ for these zinc blende QDs and $a_x = a_y \neq a_z$ for these zinc blende NPLs. For the QDs, the lattice constants monotonically decrease with increasing number of CdS MLs; this is the expected result for isotropic shell growth. The percent change of the CdSe lattice constants relative to CdSe only (i.e. 0 MLs of CdS) range from -1.2% to -1.5%. For the NPLs, we the MD minimization captures both the axial expansion and the lateral area compression that is seen in the experiments. The axial expansion can be seen by the increasing a_z values and positive percent changes given in Table 3.1 for increasing number of CdS shell MLs. The percent changes for the axial expansion do seem to be smaller for the MD minimization relative to the experimental values.[23] The MD predicted lateral area lattice constant decrease by $\sim 2.3\%$ for all CdSe/CdS NPLs shell thicknesses (Table 3.1).

CdS MLs	a_x		a_y		a_z	
	QD	NPL	QD	NPL	QD	NPL
0	6.05	6.06	6.05	6.06	6.05	6.065
1	5.98 (-1.2%)	5.92 (-2.2%)	5.98	5.92	5.98 (-1.2%)	6.13 (1.3%)
2	5.97 (-1.3%)	5.92 (-2.3%)	5.97	5.92	5.97 (-1.3%)	6.13 (1.4%)
3	5.97 (-1.4%)	5.91 (-2.3%)	5.97	5.91	5.97 (-1.4%)	6.14 (1.5%)
4	5.96 (-1.5%)	5.91 (-2.4%)	5.96	5.91	5.96 (-1.5%)	6.15 (1.7%)

Table 3.1: Lattice constants of the CdSe portion for the MD minimized CdSe/CdS heterostructures along the different axis. The number of CdS MLs is given in the first column and the average lattice constant for the NCs along the x, y and z directions are given in Angstroms. For the NPLs, a_z corresponds the axial lattice constant, and $a_x = a_y$ for all systems studied. The numbers in parenthesis are the percent change of the lattice constant relative to the core only (i.e., 0 ML) lattice constant.

This lateral area compression is in good agreement with the DFT lateral area contraction of about 3%. Altogether, MD provides nano-heterostructure atomic configurations consistent with the experiments and DFT findings for which the optical and electronic properties can be studied using the semi–empirical pseudopotential method.[23]

These strain differences led to differences in the optical gap between the strained CdSe QD and strained CdSe NPL. Quantitatively, the strained QD showed a small (~ 20 meV) blue–shift of its optical gap relative to the unstrained QD, whereas the strained CdSe NPL red–shifted its optical gap by ~ 100 meV relative to the unstrained NPL, as shown in Figure 3.5. In summary, the optical gap (i.e. emission energy) shifts (ΔE_{opt}) upon growing CdS shell MLs due to electron delocalization ($\Delta E_{\mathrm{delocalization}}$) into the shell and strain induced confinement changes ($\Delta E_{\mathrm{strain}}$):

$$\Delta E_{\mathrm{opt}} \;=\; \Delta E_{\mathrm{delocalization}} + \Delta E_{\mathrm{strain}}. \tag{3.9}$$

In both CdSe/CdS QDs and NPLs, the quasi–type-II band–alignment (Figure 3.5) leads to electron delocalization into the CdS shell, resulting in $\Delta E_{\mathrm{delocalization}} < 0$. For CdSe/CdS QDs, the isotropic compression leads to $\Delta E_{\mathrm{strain}} > 0$ which partially cancels out the red–shift contribution from the electron delocalization, leading to a small overall red–shift of the optical gap as the number of CdS MLs increases. On the other hand, $\Delta E_{\mathrm{strain}} < 0$ in CdSe/CdS NPLs because of the increase in a_z (the confined dimension) upon CdS shell growth. This strain induced red–shift adds to the delocalization induced red–shift in CdSe/CdS NPLs, resulting in a large overall red–shift of the optical in CdSe/CdS NPLs relative to CdSe/CdS QDs (Figure 3.5).

Chapter 4

Nanorods

4.1 Auger recombination in nanorods

Chapters 2 and 3 discussed the importance of electron–hole correlations on the decay of biexcitonic states via Auger recombination (AR) in QDs and core/shell QDs by comparing the interacting formalism (Eq. (2.4)) with a noninteracting formalism (Eq. (2.7)). Now, we show that the deviations in AR lifetimes predicted by the two formalisms are even larger in quasi–1D nanorods (NRs). In Figure 4.1, we show the calculated and measured[4,5,7] AR lifetimes for a series of CdSe NRs of different volumes. It is immediately evident that the noninteracting formalism is quantitatively incorrect for all NRs studied. The noninteracting–based AR lifetimes are also too long by approximately $1 - 2$ orders of magnitude! This result arises from an underestimation of the Coulomb coupling due to the electron–hole wavefunctions being delocalized over the entire NR in the noninteracting formalism; there is no electron–hole attraction to localize the electron–hole pair to form a bound Wannier exciton in the noninteracting formalism. In contrast, the interacting formalism predicts the scaling (nearly linearly with volume) as well as the magnitude of the AR lifetimes quiet accurately in comparison with the experimental results depicted by the solid blue squares.[4] Based on the results reported for spherical QDs, this is to be expected and further signifies the importance of electron–hole correlations in the AR process in confined nanostructures.

Interestingly, recent experimental measurements show nearly no volume effect on the AR lifetimes in CdSe NRs (striped blue square),[5] however, the same authors reported on the inconsistencies between transient absorption and time–resolved photoluminescence measurements (for the largest system studied, the two measurements differ by a factor of ≈ 3). Similar inconsistencies for NRs were reported for the reverse process, by which a hot exciton decays into a biexcitonic state by impact excitation, leading to multiexciton generation. Preliminary measurements reported a notable volume dependence of the impact excitation rate,[110,111] while more recent theoretical work,[112] followed by experimental validation,[68] argued that impact excitation rates are volume independent. This suggests that different experimental setups (synthesis and optical measurements) may lead to different scaling behavior.
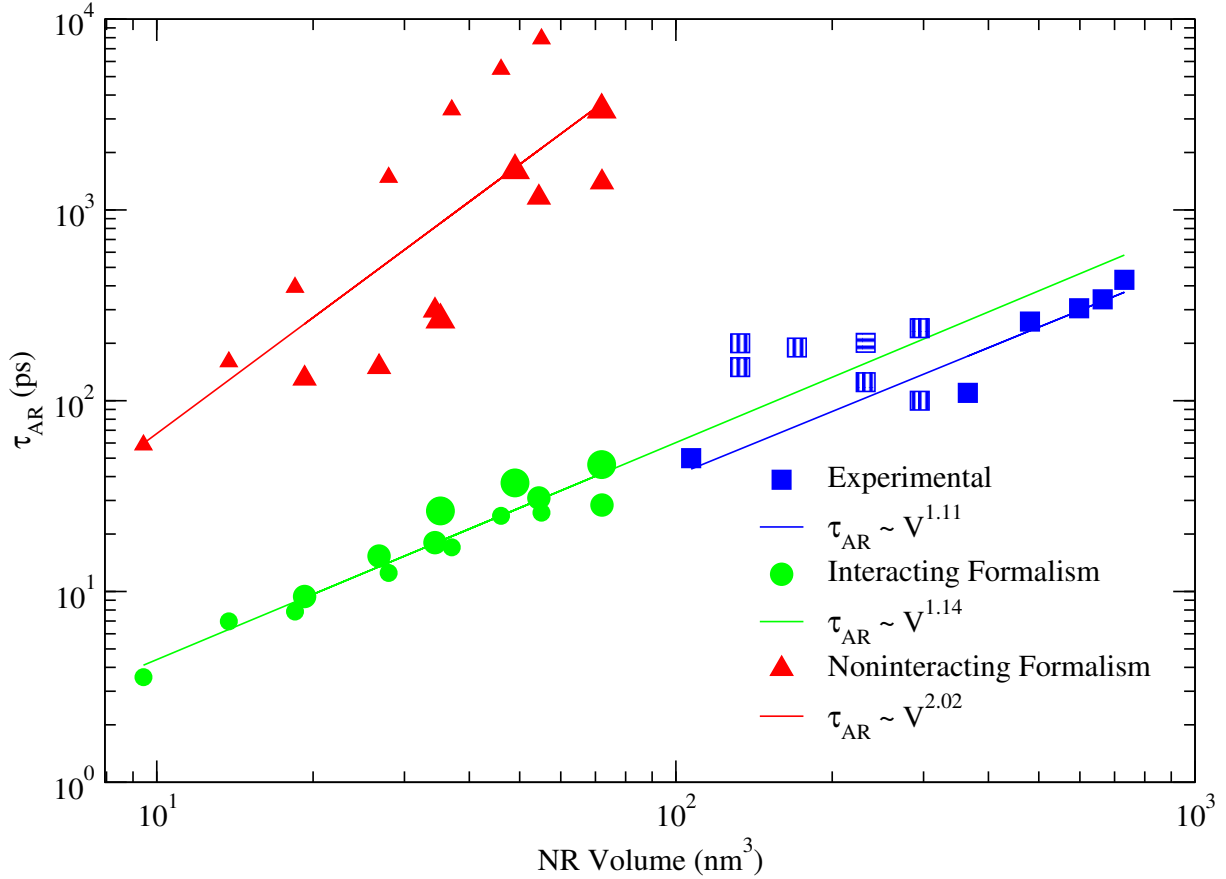
Figure 4.1: Auger recombination lifetimes for CdSe NRs as a function of the volume of the NRs predicted by the interacting (green circles), the noninteracting (red triangles) formalisms along with experimentally measured (blue squares: solid,[4] vertical[5] and horizontal[7] lines) AR lifetimes. The three different sizes used correspond to the three different diameters (1.53 nm, 2.14 nm and 2.89 nm) studied computationally. Power law fits, $\tau_{AR} = a \times V^b$, are also shown for each of the three sets of AR lifetimes.

A similar reasoning may also explain the discrepancy between the two sets of experimental results on AR lifetimes shown in Figure 4.1. However, more experimental work is needed to fully understand the diversity of experimental outcomes, in particular, given that our new theoretical predictions are consistent with one set of measurements but not the other.

Returning to the AR lifetime scaling with volume in NRs, the noninteracting formalism behaves as $\tau_{AR,NR}^{(0)} \propto V^{2.02}$. This is expected based on the scaling of the Coulomb matrix elements with the diameter and length of the NR,[112] but is in contrast to the scaling observed both experimentally[4] and theoretically using the interacting formalism. Thus, including electron–hole correlations is needed for both a quantitatively and qualitatively accurate description of the AR lifetime calculation in NRs. Intuitively, this result makes sense due to
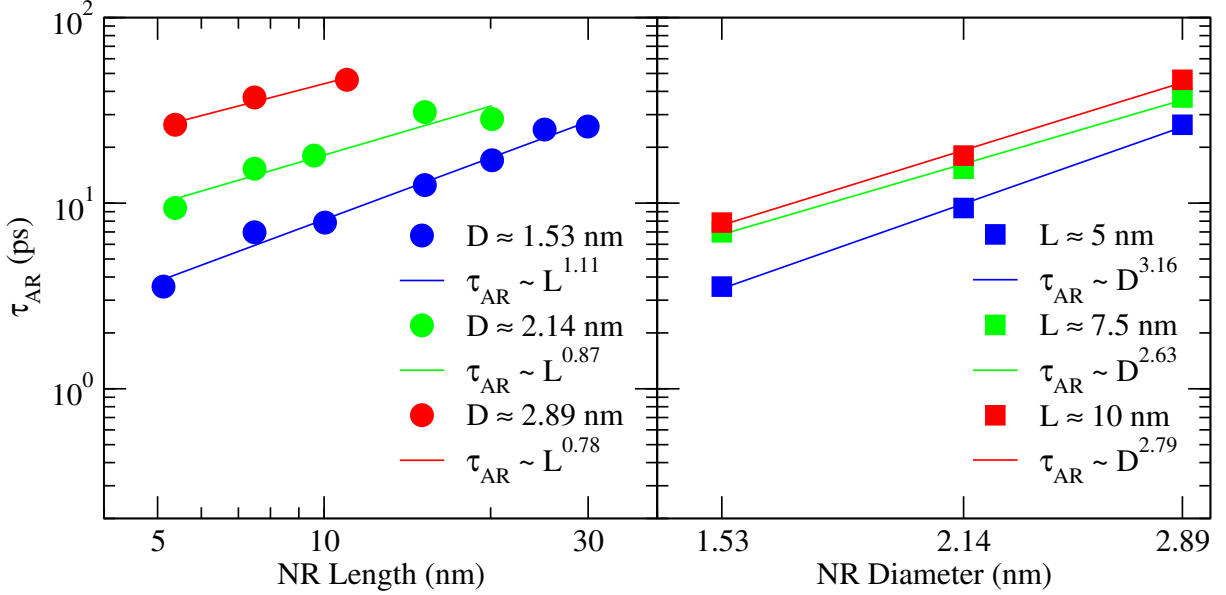
Figure 4.2: Interacting formalism based Auger recombination lifetimes for CdSe NRs as a function of the length (left) and diameter (right) of the NR. Power law fits, $\tau_{AR} = a \times D^b$ and $\tau_{AR} = a \times L^b$, are also shown for each NR set.

both the lack of confinement along the NR axis and the large electron–hole binding energy in CdSe NRs (~ 200 meV)[85] contributing to making the noninteracting carrier approximation invalid in NRs.

As mentioned above, it is experimentally difficult to independently control the NR diameter and length; however, it is trivial to do so computationally. Therefore, we analyzed the AR lifetime scaling separately for the NR diameter and length. We found that the AR lifetime scales approximately *quadratically–cubically* with the length of the NR in the noninteracting formalism, while it scales nearly *linearly* in the interacting formalism (Figure 4.2), in agreement with previous experimental measurements.[4,67–70] However, the scaling with the length of the NR depends slightly on the diameter. We also observed an approximate D^3 scaling in the interacting formalism, which still awaits experimental validation. The noninteracting formalism based scaling of the AR lifetimes are shown in Figure 4.3 with respect to the NR length (left) and diameter (right). The scaling with the length is overestimated by the noninteracting formalism relative to both the interacting formalism based scaling and experimental scaling. This result is intuitive based on the importance of electron–hole correlations in 1D systems and the lack of confinement along the NR axis.

Our finding that the noninteracting formalism is inaccurate for NRs whereas the interacting formalism is accurate further corroborates previous kinetic models and experiments that argued that the total AR rate (k_{AR}) in NRs increases quadratically with the number of excitons, n ($k_{AR}(n) \propto n(n-1)/2$).[7,55,69,113] In other words, kinetic models of AR in
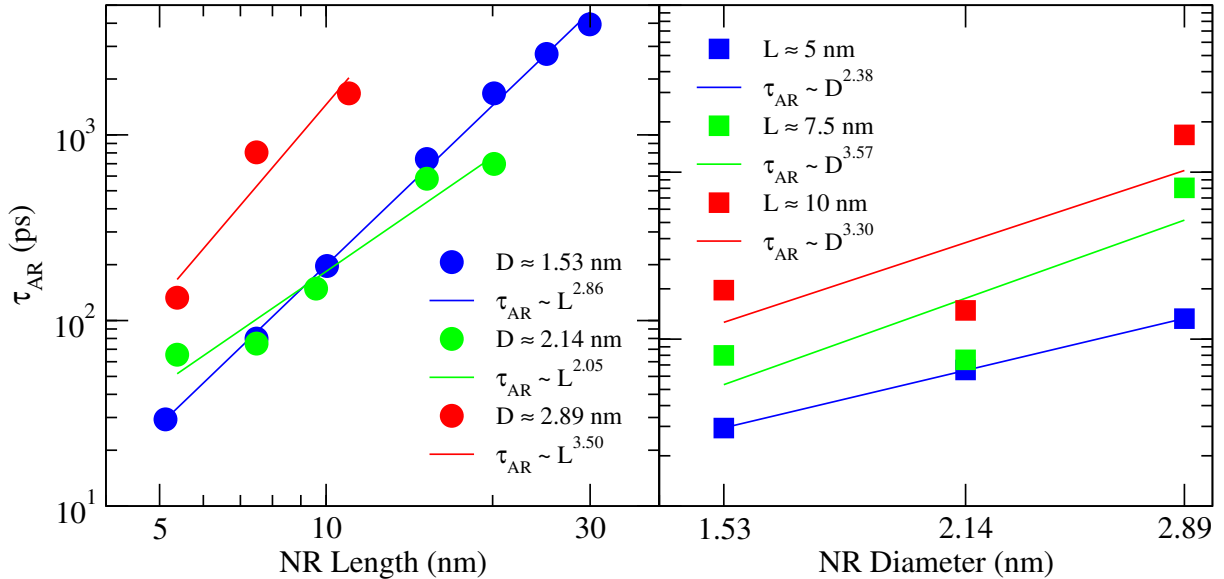
Figure 4.3: Noninteracting formalism based Auger recombination lifetimes for CdSe NRs as a function of the length (left) and diameter (right) of the NR. Power law fits, $\tau_{\mathrm{AR}} = a \times D^b$ and $\tau_{\mathrm{AR}} = a \times L^b$, are also shown for each NR set.

NRs should model AR as a bimolecular collision of two excitons; in opposition to the combinatorial scaling of $n^2 (n - 1)/2$ if modeling AR as a three particle collision between free, noninteracting electrons and holes. Overall, these results on CdSe NRs add to the body of work that electrons and holes form bound 1D Wannier excitons in quasi–1D systems such as semiconductor NRs and carbon nanotubes.[114–117]

4.2   Exciton dynamics in hybrid CdS–Au metal–nanorods

Hybrid semiconductor–metal nanoparticles (HNPs) manifest unique, synergistic electronic and optical properties as a result of combining semiconductor and metal physics via a controlled interface.[19,118] These structures can exhibit spatial charge separation across the semiconductor–metal junction upon light absorption, enabling their use as photocatalysts.[119] The combination of the photocatalytic activity of the metal domain with the ability to generate and accommodate multiple excitons in the semiconducting domain can lead to improved photocatalytic performance because injecting multiple charge carriers into the active catalytic sites can increase the quantum yield.

Herein, in collaboration with the Banin group, we show a significant metal domain size dependence of the charge carrier dynamics as well as the photocatalytic hydrogen generation efficiencies under nonlinear excitation conditions.[55] An understanding of this size depen-

dence allows one to control the charge carrier dynamics following the absorption of light. We utilized kinetic modeling to uncover a competition between the kinetics of Auger recombination and charge separation. Specifically, a crossover in the dominant process from Auger recombination to charge separation as the metal domain size increases allows for effective multiexciton dissociation and harvesting in large metal domain HNPs. This was also found to lead to relative improvement of their photocatalytic activity under nonlinear excitation conditions.[55]

In order to rationalize the aforementioned experimental findings, we developed a kinetic model that explicitly disentangles the importance of radiative recombination, Auger recombination, and electron transfer in the three systems: CdS NRs, small–tipped CdS−Au HNPs (S–HNPs), and large–tipped CdS−Au HNPs (L–HNPs). Our model includes all the essential processes of charge dynamics in the HNPs: carrier cooling, radiative recombination, charge transfer (both hot and band–edge electron transfer and hole recombination) and Auger recombination (all processes are shown pictorially in Figure (4.4)d). We solved the set of coupled differential equations (Eq. (4.1)–Eq. (4.7)) by running trajectories with a Monte Carlo approach using the Gillespie algorithm.[120] The initial conditions were such that the initial populations were zero for all particles except the initial populations of hot electrons and holes which obeyed the Poisson distribution with the average number of the hot electrons and holes equal to the average number of photons absorbed for the given excitation intensity. The kinetic model then allowed us to simulate the decay of the hot electrons and holes on the NR via the aforementioned processes. Because it is known how each process depends on the particles on the NR, we were able to fit a rate constant of each process (Table 4.1). For example, the rate constant (i.e. base rate) of Auger recombination corresponds to the Auger recombination rate for $n = 2$, and the overall Auger recombination rate increases with the number of excitons (n) with a scaling of $n\,(n-1)\,/2$. The full set of kinetic equations are:

$$n = \min\left(n_{\mathrm{e}}, n_{\mathrm{h}}\right) \tag{4.1}$$

$$\frac{dn_{\mathrm{e}}}{dt} = -nk_{\mathrm{rad}} - \frac{n\,(n-1)}{2}k_{\mathrm{AR,h}} - n\,(n-1)\,k_{\mathrm{AR,e}} - n_{\mathrm{e}}k_{\mathrm{ET}} + n_{\mathrm{e}}^{\mathrm{hot}}k_{\mathrm{cool}} \tag{4.2}$$

$$\frac{dn_{\mathrm{h}}}{dt} = -nk_{\mathrm{rad}} - \frac{n\,(n-1)}{2}k_{\mathrm{AR,e}} - n\,(n-1)\,k_{\mathrm{AR,h}} - n_{\mathrm{h}}k_{\mathrm{rec}} + n_{\mathrm{h}}^{\mathrm{hot}}k_{\mathrm{cool}} \tag{4.3}$$

$$\frac{dn_{\mathrm{e}}^{\mathrm{hot}}}{dt} = -n_{\mathrm{h}}^{\mathrm{hot}}k_{\mathrm{cool}} - n_{\mathrm{e}}^{\mathrm{hot}}k_{\mathrm{ET}}^{\mathrm{hot}} + \frac{n\,(n-1)}{2}k_{\mathrm{AR,e}} \tag{4.4}$$

$$\frac{dn_{\mathrm{h}}^{\mathrm{hot}}}{dt} = -n_{\mathrm{h}}^{\mathrm{hot}}k_{\mathrm{cool}} - n_{\mathrm{h}}^{\mathrm{hot}}k_{\mathrm{rec}}^{\mathrm{hot}} + \frac{n\,(n-1)}{2}k_{\mathrm{AR,h}} \tag{4.5}$$

$$\frac{dn_{\mathrm{e}}^{\mathrm{metal}}}{dt} = n_{\mathrm{e}}k_{\mathrm{ET}} + n_{\mathrm{e}}^{\mathrm{hot}}k_{\mathrm{ET}}^{\mathrm{hot}} \tag{4.6}$$

$$\frac{dn_{\mathrm{h}}^{\mathrm{metal}}}{dt} = n_{\mathrm{h}}k_{\mathrm{rec}} + n_{\mathrm{h}}^{\mathrm{hot}}k_{\mathrm{rec}}^{\mathrm{hot}} \tag{4.7}$$

where for each process we have a rate constant (i.e., base rate) multiplied by a statistical scaling factor and $k_{\mathrm{AR}} = k_{\mathrm{AR,e}} + k_{\mathrm{AR,h}}$, $k_{\mathrm{AR,e(h)}} = \frac{1}{2}k_{\mathrm{AR}}$ is an assumption in our model

(breaking this assumption by having asymmetric base rates for the electron and hole channels does not change the conclusions of the model). We also assumed equal carrier cooling base rates (k_{cool} = 4.0 ps^{-1}) – this choice of a cooling base rate is consistent with the hot electron decay signals shown in Ref. 55. An additional constraint on the parameters was that the base rates of electron transfer and hole recombination are related by a factor of 50 (see Supplementary Note 4 of Ref. 119 for a detailed explanation of this constraint). Therefore, our fitting parameters were only the radiative rate constant, Auger recombination rate constant and band–edge and hot electron transfer rate constants. The radiative and Auger recombination rate constants were both fit using the CdS NRs transient absorption spectrums. The radiative rate constant was fit using the low fluence transient absorption CdS NRs decays, and the Auger recombination rate constant was fit using the higher fluence transient absorption CdS NRs decays. We then used these rate constants when modeling the S–HNPs and L–HNPs decays. The electron transfers rate constants were the fitting parameters for the S–HNPs and L–HNPs. The hot electron transfer rates were estimated such that the number of carriers in our model matched the experimental number of carriers at $\sim$ 4 ps.[55] Additionally, our plots have 80% of the signal coming from the electrons and 20% coming from the holes. This parameter models the fact that the bleach signal comes primarily from electrons as compared to holes and is needed to match the experimental decays for the L–HNPs (where our model predicts all the electrons to transfer to the metal in much less than 1 ns). The base rates that resulted from the fitting procedure are shown in Table 4.1.

Figure 4.4 show the average number of excitons on a NR as a function of time as predicted by our Markov chain Monte Carlo simulations (black lines) and as determined by monitoring the bleach signals in the transient absorption measurements for CdS NRs, S–HNPS, and L–HNPS.[55] Overall, considering the simplicity of the model, the model reproduces the experimental data remarkably well. For the CdS NRs, as expected, Auger recombination dominates the multiexcitonic decays. We found that a base biexciton Auger recombination rate constant of (180 ps)$^{-1}$ matches the experimental decays very well, and we used this base Auger recombination rate in our small and large–tipped HNP simulations as well. For small–tipped HNPs, Auger recombination outcompetes electron transfer from the semiconductor to the metal tip. This is especially true for high fluences because the rate of Auger recombination increases the with square of the number of excitons (i.e., $k_{AR} \propto n (n - 1) /2$) whereas electron transfer rate only scales linearly with the number of electrons ($k_{ET} \propto n$). The smaller recovery amplitudes observed in comparison to bare NRs at 1 ns delay can be explained by a fast hot electron transfer (lifetime of $\sim$ 2 ps) which lowers the excited electron populations remaining in the NR CB state. On the other hand, for large–tipped HNPs electron transfer dominates (lifetimes of $\sim$ 0.25 ps for hot electron transfer and $\sim$ 44 ps for band–edge electron transfer). Almost no Auger recombination events occur in the large–tipped HNPs; thus, these simulations are consistent with the experimentally observed absence of fluence dependence of the MX decay in large–tipped HNPs. Altogether, these simulations point toward large–tipped HNPs benefiting more than small tips from absorbing multiple photons, because the large–tipped HNPs are able to extract all the excited
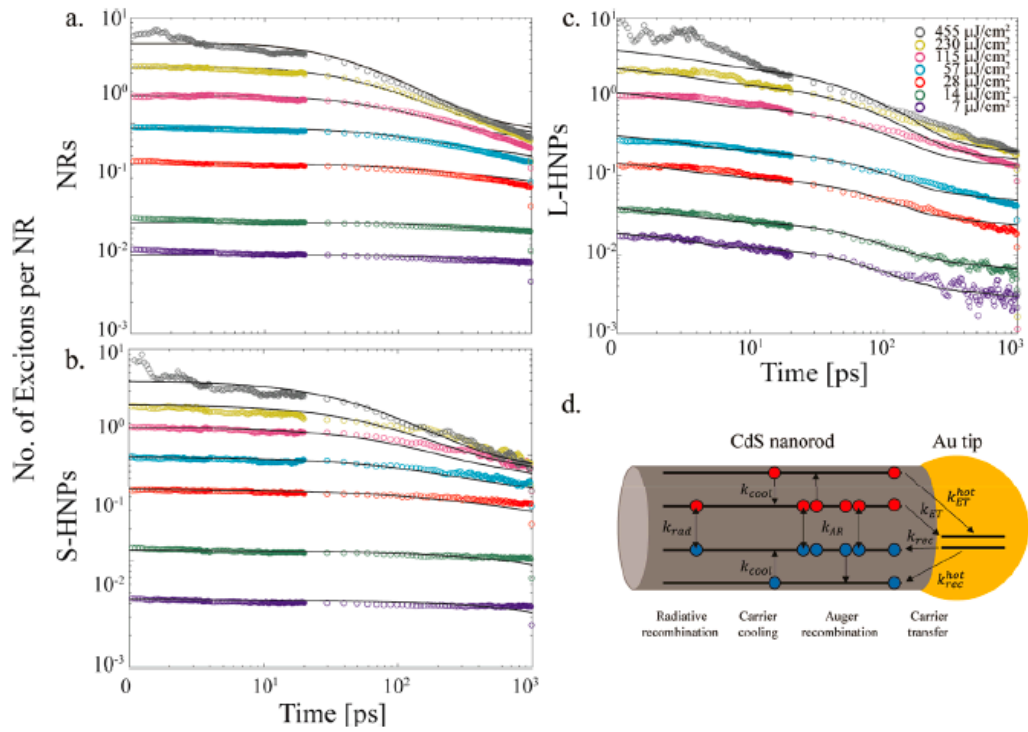
Figure 4.4: Experimental dynamics of number of excitons per rod for (a) CdS NRs and (b) small and (c) large metal–tipped CdS−Au hybrid nanoparticles at different fluences, alongside the fitted Markov chain Monte Carlo simulation curves (solid black lines). (d) A pictorial representation of the states and the four types of events that make up our kinetic model. Electrons are shown in red and holes in blue. Double–sided arrows indicate a loss of an exciton whereas single sided arrows indicate the carrier moving from one state to another.

Process	Scaling	Process Base Lifetime		
		CdS NRs	S–HNPs	L–HNPs
k_{rad}	$\binom{n}{1}$	5.0 ns	5.0 ns	5.0 ns
k_{AR}	$\binom{n}{2}$	180 ps	180 ps	180 ps
k_{cool}	$\binom{n_{\mathrm{e(h)}}}{1}$	0.25 ps	0.25 ps	0.25 ps
k_{ET}	$\binom{n_{\mathrm{e}}}{1}$	0.0 ps	5.0 ns	44 ps
$k_{\mathrm{ET}}^{\mathrm{hot}}$	$\binom{n_{\mathrm{e}}^{\mathrm{hot}}}{1}$	0.0 ps	2.0 ps	0.25 ps
k_{rec}	$\binom{n_{\mathrm{h}}}{1}$	0.0 ps	$50\tau_{\mathrm{ET}}$	$50\tau_{\mathrm{ET}}$
$k_{\mathrm{rec}}^{\mathrm{hot}}$	$\binom{n_{\mathrm{h}}^{\mathrm{hot}}}{1}$	0.0 ps	$50\tau_{\mathrm{ET}}^{\mathrm{hot}}$	$50\tau_{\mathrm{ET}}^{\mathrm{hot}}$

Table 4.1: Parameters of the kinetic model along with the scaling (i.e., how the total rate of the process depends on the populations of the particles) of each process. The statistical scaling factors are written in standard $\binom{n}{k} = \frac{n!}{k!(n-k)!}$ notation.

electrons whereas the small–tipped HNPs lose most of their excited electrons due to Auger recombination.

In conclusion, CdS−Au HNPs with large Au tips are found to be advantageous for MX dissociation and transfer to the metal domain. This also led to relative improvement in their photocatalytic activity under nonlinear excitation conditions for the hydrogen generation reaction.[55] This size dependence was explained by the competition between Auger recombination that dominates the multiexciton dynamics in NRs and small–tipped HNPs and ultrafast electron transfer that is greatly enhanced and therefore dominates over Auger recombination in large–tipped HNPs. Altogether, an in–depth understanding of the synergistic light–induced charge separation process across the semiconductor−metal nanojunction in both the low and high excitation limits provides a key–knob to control the relaxation dynamics and will lead to the further utilization of hybrid metal−semiconductor nanosystems as efficient photocatalysts in numerous applications.

4.3 CdSe/Cd$_{1-x}$Zn$_x$S seeded nanorods with minimal blinking and polarized emission

Colloidal semiconductor nanocrystals are outstanding building blocks for various applications because of the ability to tune their properties by changing their size, shape, composition, and surface characteristics.[13,14,121,122] Within this family, seeded NRs (SNRs) composed of a spherical seed from one semiconductor material embedded in a rod–shaped second semiconductor material are particularly interesting, since they show tunable properties manifesting their mixed 0D–1D character.[123,124] In these SNRs, control of the electronic properties is further enabled by independently adjusting the size of the seed and/or the rod.[125]

In this work, we present atomistic electronic structure calculations on CdSe/Cd$_{1-x}$Zn$_x$S SNRs with radially graded rod compositions and directly compare them to experimental measurements performed by the Banin group.[95] These novel seeded rods exhibit intense, highly polarized emission and minimal fluorescence intermittency owing to the localization of the electron in the region of the seed as demonstrated by molecular dynamics and electronic structure calculations. The importance of the graded composition of the nanorod as demonstrated here offers a path for designing high–quality nanostructures with targeted optoelectronic properties. In other words, the controlled addition of Zn influences and improves the nanorods' optoelectronic performance by providing an additional handle to manipulate the degree confinement beyond the common size control approach.[95] These nanorods may be utilized in applications that require the generation of a full, rich spectrum such as energy-efficient displays and lighting.

To begin to better understand the influence of Zn on the optical properties of the SNRs, we developed an atomistic model of CdSe/Cd$_{1-x}$Zn$_x$S SNR with no adjustable parameters and computed the fundamental and optical band gaps for SNRs with varying degrees of Zn:Cd alloying.[95] All calculations were performed for a 1.5 nm diameter CdSe seed and a 20 nm × 4 nm rod (see insets of Figure 4.5). The fundamental gaps are higher than the optical gaps by ∼ 200 meV. For the neat CdSe/CdS SNR, we find that there is an excellent agreement between the measured and computed optical gaps as well as for the value of the exciton binding energy in comparison to experimental results obtained from scanning tunneling spectroscopy measurements.[126] This provide additional validation of the model.

We find an increase in the fundamental and optical gap energies upon the addition of Zn, which can be explained by a stronger confinement of the electron to the CdSe seed when Zn is added to the rod. This is illustrated in Figure 4.5, where we plot the electron density projected onto the rod axis for the fundamental (upper panel, ignoring electron–hole interactions) and optical (lower panel) excitations (the insets show the corresponding 3D electron densities as well as the seed location). In both cases, it is clearly seen that the extent of overlap between the electron wave function and the CdSe core increases with the Zn content. The effect is more pronounced for the noninteracting (fundamental) case but is significant also when the electron–hole interactions are included (the width of the projected electron density decreases by 20% when Zn is added at a ratio of 2 : 1).[95] The observed
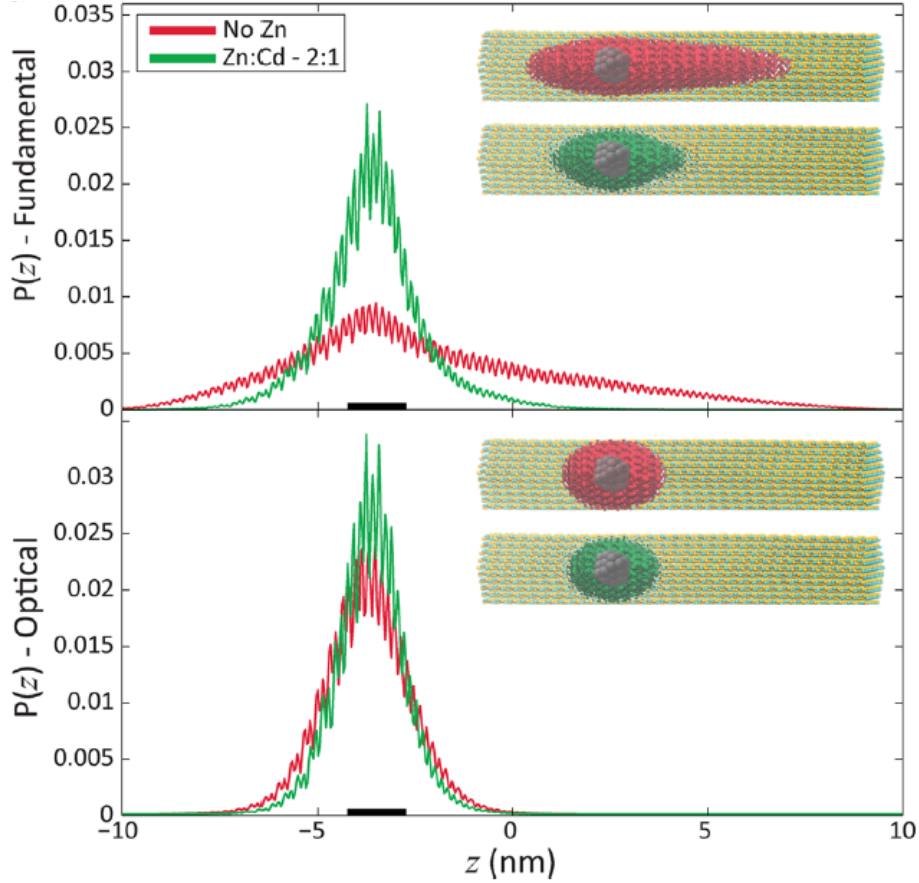
Figure 4.5: Comparison between measured (left panel) and calculated (right panel) of the absorption degree of polarization as a function of energy above the optical gap for CdSe/Cd$_{1\text{-}x}$Zn$_x$S seeded nanorods.

localization of the electron near the core as the Zn content increases leads to a quantum confinement effect which results in an increase of the optical gap upon addition of Zn to the shell. This electron localization is also intertwined with the improved QY and reduced blinking seen in the Zn containing SNRs.[95]

In our theoretical investigation of the polarization, we were able to explicitly calculate the energies of the individual optical transitions along with their intensities, polarization, and radiative lifetimes. In our comparison of CdSe/CdS and CdSe/Cd$_{1-x}$Zn$_x$S SNRs, we found that the Zn being radially distributed was imperative for the improved polarization of the CdSe/Cd$_{1-x}$Zn$_x$S SNRs. Specifically, the separation between the z–polarized transition (which arises from the lowest energy exciton) and the xy–polarized transitions were calculated to be 88, 118, and 87 meV for the CdSe/CdS, graded composition CdSe/Cd$_{0.75}$Zn$_{0.25}$S, and homogeneously distributed CdSe/Cd$_{0.75}$Zn$_{0.25}$S SNRs, respectively. The calculated absorption polarization spectrum is shown in the right panel of Figure 4.6 and is clearly in
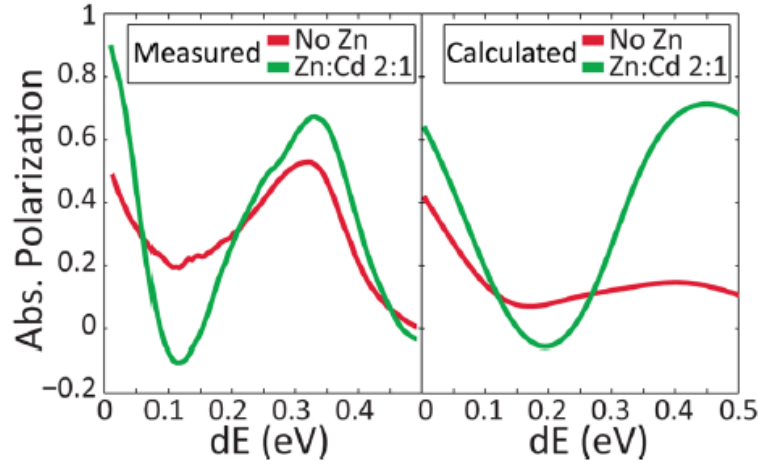
Figure 4.6: Comparison between measured (left panel) and calculated (right panel) of the absorption degree of polarization as a function of energy above the optical gap for CdSe/Cd$_{1-x}$Zn$_x$S seeded nanorods.

agreement with the measured absorption polarization that is shown in the left panel of Figure 4.6.[95] Thus, the control of the rod's radial composition provides an additional powerful knob to tune the optoelectronic properties. These insights will enable further design of SNRs with specific properties (e.g., type–I or quasi–type–II band alignments) for various applications.

Chapter 5

Nanoplatelets

5.1 Exciton size in CdSe nanoplatelets

Colloidal, quasi–2D semiconductor nanoplatelets (NPLs) exhibit strong quantum confinement in only one dimension, which results in an electronic structure that is significantly altered compared to that of other quantum–confined nanomaterials. Whereas it is often assumed that the lack of quantum confinement in the lateral plane yields a spatially extended exciton, reduced dielectric screening and enhanced Coulomb interactions in quasi–2D systems potentially challenges this picture. Herein, we performed atomistic electronic structure calculations of the exciton size for NPLs with varying lengths, widths, and thicknesses to elucidate that the exciton lateral extent is comparable in magnitude to the NPL thickness, indicating that the quantum confinement, reduced screening, and the quasi–2D nature of NPLs strongly reduce the exciton lateral extent compared to bulk excitons.

Since the first detailed report of CdSe NPLs,[40] the topic of excitons in CdSe NPLs has been treated theoretically,[127–130] but with only one explicit calculation of exciton size.[131] As in Ref. 131, estimates regarding exciton size can be developed based on the exciton binding energy,[132] but discrepancies in reports of this energy exist, with experimental and theoretical papers conveying values ranging from about 100 meV to greater than 400 meV.[127,128,131,133] Derived values also depend upon whether the NPLs are treated using 3D or 2D Coulomb potentials. Whereas it is apparent that the change in dimensionality from 3D bulk material to quasi–2D NPLs increases the exciton binding energy through reduced dielectric screening and the enhanced Coulomb interaction in two dimensions, as is the case with monolayer transition metal dichalcogenides,[134,135] it is not clear to what degree this alters the lateral exciton extent in the II–VI NPLs.

In order to better understand the lateral exciton extent in CdSe NPLs, magneto–optical spectroscopy was performed to obtain $\left\langle r^2_{\mathrm{plane}} \right\rangle$ from the diamagnetic shift coefficient (σ):

$$\sigma = \frac{e^2}{8\mu_{\mathrm{r,plane}}} \left\langle r^2_{\mathrm{plane}} \right\rangle. \tag{5.1}$$

In the above, r_{plane} is the radial coordinate between the electron and hole in the direction

perpendicular to the magnetic field, e is the elementary charge, and $\mu_{\text{r,plane}}$ is the in–plane exciton reduced mass. Thus, $\langle r^2_{\text{plane}} \rangle$ is the expectation value of $x^2 + y^2$ with respect to the exciton wavefunction.[107] In order to understand and to be able to compare directly to experiments, we calculated the root–mean–square exciton radius ($r_{\text{plane}} = \sqrt{\langle r^2_{\text{plane}} \rangle}$).

Specifically, we employed the semi–empirical pseudopotential method to obtain the non-interacting (i.e. single–particle) electron and hole states. These calculations were performed on real–space grids and converged with respect to the grid point density. Because we are only interested in the lowest energy excitonic states, we were able to use filter–diagonalization techniques[81,83] to calculate only the lowest energy electron (ϕ_a) and hole (ϕ_i) eigenstates. The eigenstates obtained from the application of filter–diagonalization techniques were then used as input to the Bethe-Salpeter equation.[36] The Bethe–Salpeter equation was solved within the static dielectric constant approximation ($\epsilon = 5$). Although the quantitative accuracy may improve if a more complicated approximation for the screening was used (e.g. the random phase approximation), we do not expect any qualitative changes. In other words, it would be expected the dependence of r_{plane} with the number of MLs should hold, because if the screening were different between the 3, 4 and 5 ML NPLs, it would be expected that the thinner NPLs would have the least amount of screening (i.e. lowest ϵ) which would lead to even smaller r_{plane} values for the thinner NPLs relative to the thicker NPLs. The output from solving the Bethe–Salpeter equation are the excitonic states:

$$\psi \left(\mathbf{r}_e, r_h \right) \quad = \quad \sum_{a,i} c_{a,i} \phi_a \left(\mathbf{r}_e \right) \phi_i \left(\mathbf{r}_h \right) \tag{5.2}$$

where ϕ_a (ϕ_i) are the single–particle electron (hole) eigenstates, $\mathbf{r}_e$ ($\mathbf{r}_h$) is the position of the electron (hole), and the coefficients ($c_{a,i}$) are obtained by diagonalizing the Bethe–Salpeter Hamiltonian.[36] After calculating the excitonic states (i.e. correlated electron-hole states), we then calculated the in–plane exciton size, as follows:

$$\langle r^2_{\text{plane}} \rangle \quad = \quad \langle \psi \left| (x_e - x_h)^2 + (y_e - y_h)^2 \right| \psi \rangle \tag{5.3}$$

where $|\psi\rangle$ is the output from the Bethe–Salpeter equation discussed above. The calculated values for $r_{\text{plane}} = \sqrt{\langle r^2_{\text{plane}} \rangle}$ are shown in Figure 5.1 and reported in Table 5.1.

The calculated in–plane exciton radii (shown in Figure 5.1) are of similar magnitude to the experimentally determined in–plane exciton radii,[107] in the range of $1.0 - 1.5$ nm depending only weakly on the NPL thickness and lateral area. The increase of the in–plane exciton radius with increasing NPL dimensions (both lateral area and thickness) can be justified on account of the reduction in Coulomb attraction between the electron and hole when the volume of the NPL is increased. Notably, although dielectric screening affects the overall lateral extent of the exciton, the exciton spatial extent remains small (in the range of $1.2 - 2.0$ nm) even when a larger, less warranted dielectric constant is chosen (see Table 5.1 and the discussion below). The measured and calculated small, in–plane exciton radii found here are consistent with reports for other 2D structures, such as transition metal
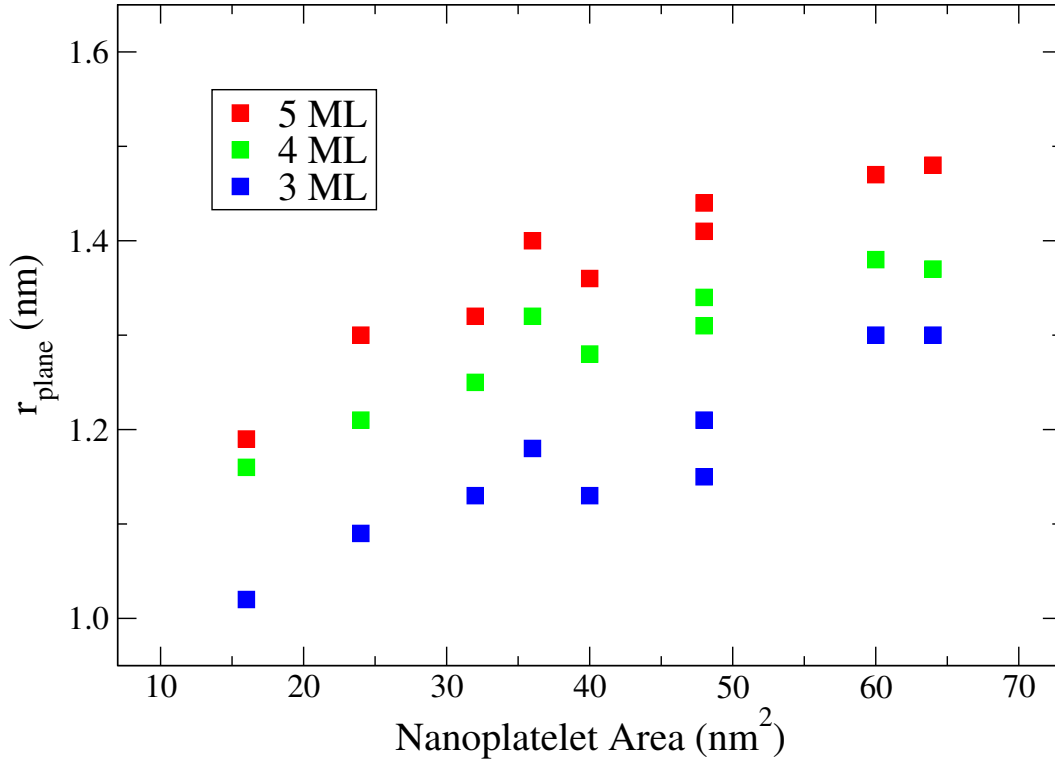
Figure 5.1: Atomistic electronic structure calculations of r_{plane} for 3, 4, and 5 ML CdSe NPLs of varying lateral sizes.

dichalcogenides. An often–invoked explanation for the small exciton size is based on reduced screening, where the electron and hole interact through the surrounding lower dielectric environment, leading to localization of the electron−hole pair, but are also consistent with pictures of minimized orbital kinetic energy.[107]

The calculations described above use a value of $\epsilon = 5$ as the high frequency dielectric constant. While the static dielectric constant of bulk CdSe is typically taken to be 10, the contribution from the nuclei ($\epsilon = 3.5$) does not contribute as the energy scale of excitons is in the $100 - 200$ meV range, which is much larger than the highest energy phonons for this composition. Furthermore, in quantum–confined materials, the dielectric screening is reduced, and our calculations have suggested that a dielectric constant of $\epsilon = 5$ is most appropriate. Nevertheless, as the value of the dielectric constant does impact the spatial extent of the exciton, we have performed additional calculations using $\epsilon = 10$ to investigate the effect of altered dielectric screening. Table 5.1 compares values for the in–plane exciton radius for $\epsilon = 5$ versus $\epsilon = 10$. While the in–plane exciton radius is larger when the dielectric screening is increased to 10, the values (which range from 1.2 nm to 2.0 nm) are still significantly less than the bulk exciton Bohr radius of 5.6 nm for CdSe. Additionally, all of the qualitative trends for the in–plane exciton size are valid, irrespective of the choice

ML	$L_x \times L_y$ (nm $\times$ nm)	r_{plane} for $\epsilon = 5$ (nm)	r_{plane} for $\epsilon = 10$ (nm)
3	4×4	1.02	1.22
3	4×6	1.09	1.39
3	4×8	1.13	1.43
3	4×10	1.13	1.45
3	4×12	1.15	1.50
3	6×6	1.18	1.61
3	6×8	1.21	1.69
3	6×10	1.30	1.74
3	8×8	1.30	1.79
4	4×4	1.16	1.36
4	4×6	1.21	1.47
4	4×8	1.25	1.53
4	4×10	1.28	1.60
4	4×12	1.31	1.62
4	6×6	1.32	1.60
4	6×8	1.34	1.69
4	6×10	1.38	1.79
4	8×8	1.37	1.79
5	4×4	1.19	1.34
5	4×6	1.30	1.53
5	4×8	1.32	1.60
5	4×10	1.36	1.63
5	4×12	1.41	1.69
5	6×6	1.40	1.76
5	6×8	1.44	1.85
5	6×10	1.47	1.89
5	8×8	1.48	1.96

Table 5.1: Root–mean–square in–plane exciton radius (r_{plane}) for 3, 4, and 5 ML CdSe NPLs of varying lateral sizes, for different values of the dielectric constant.

of dielectric constant.

In conclusion, the atomistic modeling using realistic, discrete NPL structures arrives at similar r_{plane} values as those determined from magneto–optical experiments and supports the picture of excitons in NPLs being small and nearly spherical symmetric.[107] These small values of r_{plane} relative to the NPL lateral area has important consequences for both the radiative recombination rate (smaller r_{plane} values lead to larger oscillator strengths) and, as discussed in detail in the next section, on the decay rate of biexcitons via Auger recombination.

5.2 Auger recombination in nanoplatelets

Colloidal semiconductor nanoplatelets (NPLs) are quasi–2D materials with thicknesses that can be controlled with monolayer (ML) precision and lengths and widths that can be controlled on the nanometer scale.[40,136,137] The ability to vary the synthesis to separately yield NPLs of 2 through 8 ML thickness, with 3, 4, and 5 ML thicknesses the most well studied, opens the door to tuning the properties of the quasi–2D semiconductor NPL by just changing their thickness.[138–140] The most obvious property that can be tuned is that of the optical gap (i.e. absorption and emission energies), as the thickness is the primary determinant of the degree of quantum confinement in NPLs.[8,29,40,137] A more subtle aspect of the emission that also changes upon a change in the thickness is the rate of radiative recombination. Not only does the radiative recombination rate depend on the thickness, it also depends on the lateral area of the NPL.[133,141,142] An additional aspect related to applications of NPLs, ranging from lasers to photocatalysts, is that multiple excitons are required to be present in the NPL at the same time.[8,44,45,143–145] Thus, it is of general interest to understand how the lifetime of multiexcitonic states depends on the lateral area and thickness of NPLs.

Herein, we focus on the decay of biexcitonic states via Auger recombination (similar to exciton–exciton annihilation). Auger recombination (AR) is a nonradiative process in which one electron–hole pair recombines by transferring its energy to an additional quasiparticle (Figure 5.2A) and is typically the dominant mechanism by which multiexcitonic states decay in semiconductor nanomaterials, making it of central importance to many nanomaterial–based applications.[3,41] Therefore, a fundamental understanding on how the AR lifetime (τ_{AR}) depends on the size and dimensionality of nanomaterials is of broad interest.

In quasi–0D quantum dots, the AR lifetime (see Eq. (5.4)) depends linearly on the nanocrystal volume and has become known as the "universal volume scaling law."[3,16,68,76,92] For quasi–1D nanomaterials, the AR lifetime scales linearly with the length of the nanorod and nearly quadratically with its diameter, thereby approximately following the universal volume scaling law.[4,76] The situation is somewhat more evolved for quasi–2D CdSe NPLs. Most recently, Li and Lian[9] reported that the AR lifetime scales linearly with the lateral area, $A = L_x L_y$ (see sketch in Figure 5.2B). This linear dependence was rationalized by thinking of AR in NPLs as a classical collision of two particles in which the frequency of collision is limited by their spatial diffusion. Because electron–hole pairs are known to form bound Wannier excitons that are nearly spherical with average in–plane separation distances of approximately $1 - 2$ nm in CdSe NPLs,[107,131] the classical picture of AR as a collision between two independent particles where the particles are excitons is reasonable at first glance. Underlying this picture of AR are the assumptions that the biexciton binding energy is negligible such that the two excitons do not form a bound biexciton. And that the excitons are not coherent throughout the NPL and, therefore, diffuse in the NPL. A linear dependence of the AR lifetime on the lateral area was also recently reported for CsPbBr$_3$ perovskite NPLs.[93] These studies contradict an earlier report by She *et al.*[8] which found that the AR lifetimes are independent of area. It is important to note that the two studies on CdSe performed their studies using similarly sized NPLs.[8,9] In contrast to the volume
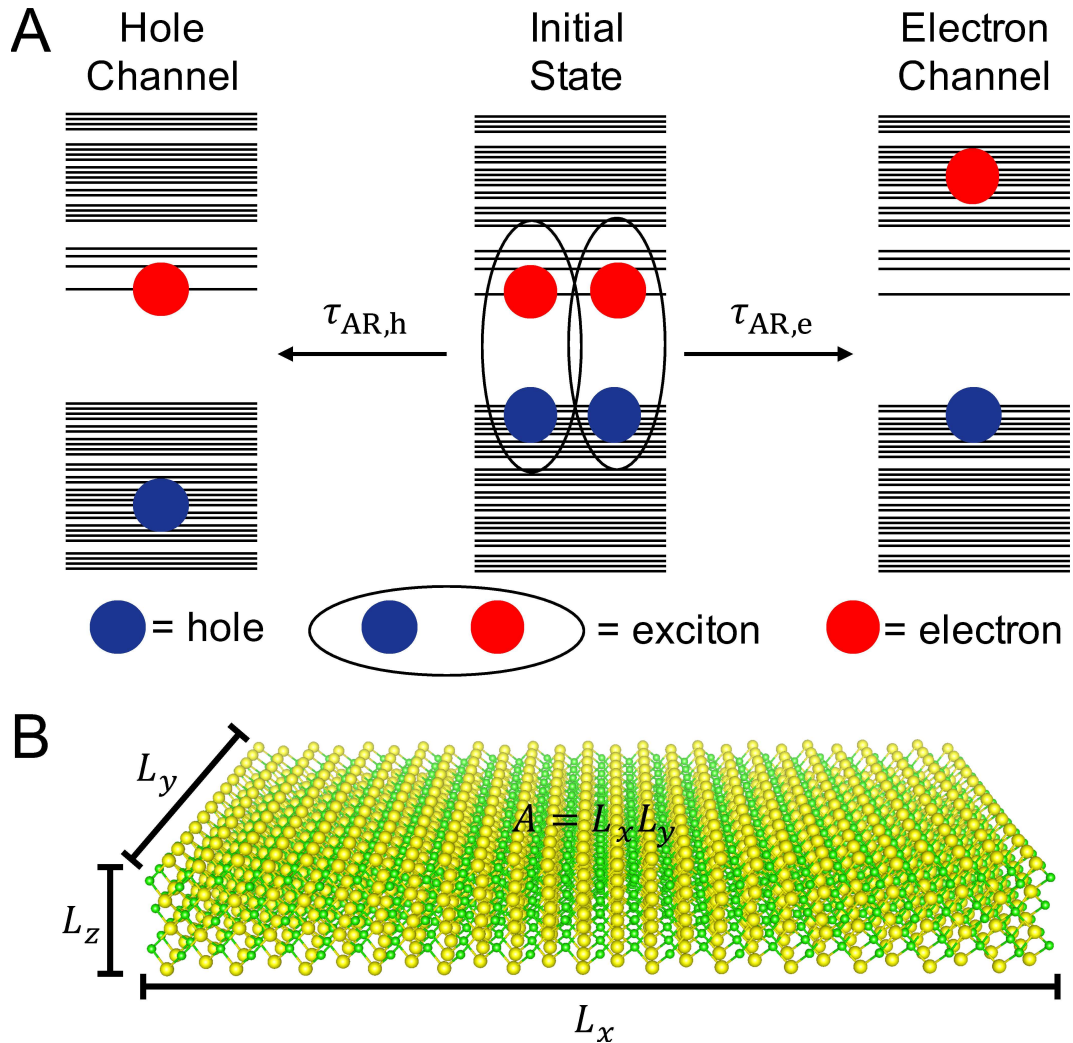
Figure 5.2: (A) Schematic of an Auger recombination event. The initial biexcitonic state is shown as two spatially uncorrelated excitonic states and the final states are shown as unbound electron–hole pairs. The hole (electron) channel on the left (right) shows the hole (electron) receiving a majority of the energy from the recombining exciton. (B) Representation of a 3 ML ($L_z = 0.91$ nm) CdSe nanoplatelet with $L_x = L_y = 8$ nm. Cd (Se) atoms are shown in yellow (green).

(i.e. $\tau_{AR} \propto A^1$) or sub–volume ($\tau_{AR} \propto A^0$) scaling of AR lifetimes with respect to the lateral area of NPLs, the scaling of the AR lifetime as a function of the NPL thickness (L_z) or number of monolayers (MLs) was reported to obey a seventh power dependence, $\tau_{AR} \propto L_z^7$, in CdSe NPLs, a super–volume dependence.[9]

In this study, we provide an alternative mechanism that leads to similar area scaling for AR lifetimes in NPLs, which is based on the traditional scattering picture within lowest order

perturbation theory coupling the initial biexcitonic state with the final electron–hole pair. A similar approach has been successfully applied to describe AR lifetimes in 0D quantum dots and quasi–1D nanorods, with very good agreement in comparison to experimental results over a wide range of system sizes.[76] Here, we focus on the regime $A \leq 100$ nm^2 which is suitable for this coherent scattering picture and study the AR lifetimes for different CdSe NPLs shapes and thicknesses by applying our recently developed stochastic approach.[146] We uncover the underlying physics that cause the particular scaling in this coherent scattering picture. In addition, we analyze the thickness–dependent AR lifetimes in quasi–2D NPLs (as well as other properties, such as electron and hole kinetic energy, exciton binding energy, exciton Bohr radius, and screening), and provide reasonings for the mild thickness dependence observed in the coherent scattering picture as well as in other experiments on similar NPLs.

Due to the computational methods being described in details in previous chapters, only a brief description will be recapped here. AR is commonly described as a Coulomb–mediated scattering process for which an initial biexcitonic state ($|B\rangle$) of energy E_B decays into a final excitonic state ($|S\rangle$) of energy E_S via Coulomb (V) scattering (Figure 5.2). An AR lifetime (τ_{AR}) for a nanostructure can be calculated using Fermi's golden rule where we average over thermally distributed initial biexcitonic states and sum over all final decay channels into single excitonic states:[72,76]

$$\tau_{\mathrm{AR}}^{-1} = \sum_B \frac{e^{-\beta E_B}}{Z_B} \left[\frac{2\pi}{\hbar} \sum_S |\langle B\,|V|\,S\rangle|^2 \, \delta\left(E_B - E_S\right) \right]. \tag{5.4}$$

In the above, the delta function ($\delta\left(E_B - E_S\right)$) enforces energy conservation between the initial and final states and the partition function (Z_B) is for the initial biexcitonic states (we assume biexcitons follow Boltzmann statistics). Utilizing the interacting, exciton–based framework, previously developed by Philbin and Rabani,[76] a deterministic calculation of an AR lifetime can be performed using

$$\tau_{\mathrm{AR}}^{-1} = \tau_{\mathrm{AR,e}}^{-1} + \tau_{\mathrm{AR,h}}^{-1} \tag{5.5}$$

$$\tau_{\mathrm{AR,e}}^{-1} = \frac{2\pi}{\hbar Z_B} \sum_B e^{-\beta E_B} \sum_{a,i} \left| \sum_{b,c,k} c_{b,i}^B c_{c,k}^B V_{abck} \right|^2 \delta\left(E_B - E_S\right)$$

$$\tau_{\mathrm{AR,h}}^{-1} = \frac{2\pi}{\hbar Z_B} \sum_B e^{-\beta E_B} \sum_{a,i} \left| \sum_{j,c,k} c_{a,j}^B c_{c,k}^B V_{ijck} \right|^2 \delta\left(E_B - E_S\right),$$

where $E_S = \varepsilon_a - \varepsilon_i$ and V_{rsut} is the Coulomb coupling given by

$$V_{rsut} = \iint \frac{\phi_r\left(\mathbf{r}\right) \phi_s\left(\mathbf{r}\right) \phi_u\left(\mathbf{r}'\right) \phi_t\left(\mathbf{r}'\right)}{|\mathbf{r} - \mathbf{r}'|} d^3\mathbf{r}\, d^3\mathbf{r}'. \tag{5.6}$$

In the above equations, $\phi_r\left(\mathbf{r}\right)$ are quasiparticle states for electrons ($r \in a, b, c, ...$) or holes ($r \in i, j, k, ...$) and the coefficients ($c_{c,k}^B$) in Eq. (5.5) are determined by solving the Bethe–

Salpeter equation.[36] The above approach includes spatial correlations within the electron–hole pairs but ignores correlations between the excitons[77] and in the final electron–hole pair. It was previously shown that this interacting formalism predicts quantitively accurate AR lifetimes for quantum dots, nanorods and core/shell quantum dots.[76,146] On the other hand, noninteracting formalisms that ignore all electron–hole interactions in the initial biexcitonic state do not predict accurate AR lifetimes except for quantum dots in the very strong confinement regime[72] — highlighting the importance of exciton formation in nanocrystals. However, a major drawback of the interacting formalism for calculating AR lifetimes (Eq. (5.5)) is the computational cost, which scales with the system size (N) as $O\left(N^5\right)$. To reduce the computational cost, we utilize a stochastic formulation of Eq. (5.5) to calculate AR lifetimes for the CdSe NPLs studied in this work:[146]

$$\tau_{\mathrm{AR}}^{-1} = \tau_{\mathrm{AR,e}}^{-1} + \tau_{\mathrm{AR,h}}^{-1} \tag{5.7}$$

$$\tau_{\mathrm{AR,e}}^{-1} = \frac{2\pi}{\hbar Z_B} \sum_B e^{-\beta E_B} \left\langle \left\langle \left(\sum_b c_{b,i^A}^B R_{\theta^A b}^{\zeta'} \sum_{c,k} c_{c,k}^B R_{ck}^{\zeta'} \right)^* \left\langle \sum_b c_{b,i^A}^B R_{\theta^A b}^{\zeta} \sum_{c,k} c_{c,k}^B R_{ck}^{\zeta} \right\rangle_{\zeta'} \right\rangle_{\zeta} \right\rangle_A$$

$$\tau_{\mathrm{AR,h}}^{-1} = \frac{2\pi}{\hbar Z_B} \sum_B e^{-\beta E_B} \left\langle \left\langle \left(\sum_j c_{a^I,j}^B R_{\theta^I j}^{\zeta'} \sum_{c,k} c_{c,k}^B R_{ck}^{\zeta'} \right)^* \left\langle \sum_j c_{a^I,j}^B R_{\theta^I j}^{\zeta} \sum_{c,k} c_{c,k}^B R_{ck}^{\zeta} \right\rangle_{\zeta'} \right\rangle_{\zeta} \right\rangle_I,$$

Eq. (5.7), the indices θ^A, i^A and a^I, θ^I are sampled final states from the complete set of single excitonic states $(a, i$ pairs) in Eq. (5.5) and the notation $\langle ... \rangle_\zeta$ denotes an average over N_s stochastic orbitals. The R_{rs}^ζ matrices are calculated using

$$R_{rs}^\zeta = \int \phi_r^*\left(\mathbf{r}\right) \phi_s^*\left(\mathbf{r}\right) \theta^\zeta\left(\mathbf{r}\right) d^3\mathbf{r}, \tag{5.8}$$

where $\theta^\zeta\left(\mathbf{r}\right)$ is a stochastic representation of the Coulomb integral given by[101]

$$\theta^\zeta\left(\mathbf{r}\right) = \frac{1}{\left(2\pi\right)^3} \int d\mathbf{k} \sqrt{\widetilde{u}_\mathrm{C}\left(\mathbf{k}\right)}\, \mathrm{e}^{\mathrm{i}\varphi(\mathbf{k})}\, \mathrm{e}^{\mathrm{i}\mathbf{k}\cdot\mathbf{r}} \tag{5.9}$$

where $\varphi\left(\mathbf{k}\right)$ is a random phase between 0 and 2π at each k–space grid point, $\widetilde{u}_\mathrm{C}\left(\mathbf{k}\right) = 4\pi/k^2$ is the Fourier transform of the Coulomb potential. The computational cost of Eq. (5.7), is drastically lower than Eq. (5.5) for large systems sizes, scaling as $O\left(N^2\right)$ instead of $O\left(N^5\right)$.[146]

To begin to understand biexciton AR in CdSe NPLs, we compare the calculated AR lifetimes using both a noninteracting, free carrier–based formalism and an interacting, exciton–based formalism[146] to experimental measurements performed herein using transient absorption spectroscopy and to past measurements[8,9] for 4 ML ($L_z = 1.21$ nm) CdSe NPLs with various lateral areas ($A = L_x L_y$). NPLs were synthesized according to previous reports[8,23,147] using reaction time and temperature to adjust the lateral areas, later determined via transmission electron microscopy. For transient absorption measurements, samples were excited

at 1 kHz using the 400 nm, frequency–doubled output of a 35 fs Ti:sapphire laser and probed using white light generated by passing 800 nm light through a sapphire plate. Scans were acquired at fluences corresponding to very low ($\langle N_{\text{exc}}\,(t=0)\rangle \ll 0.1$) to moderate ($\langle N_{\text{exc}}\,(t=0)\rangle \approx 0.2 - 0.5$) average number of initial excitons ($\langle N_{\text{exc}}\,(t=0)\rangle$). Kinetics at the bleach maximum were normalized at $1.5 - 2.0$ ns, where dynamics are dominated by single exciton recombination, and then differenced to separate out biexciton–only dynamics. Biexciton dynamics were fit to a single exponential, and this process was repeated for multiple measurements at moderate fluences to yield an average AR lifetime.

As expected, the inclusion of electron–hole correlations in the initial biexcitonic state drastically impacts both the predicted AR lifetimes and scaling of the AR lifetimes with respect to the NPL lateral area. Specifically, Figure 5.3 shows that the noninteracting (free carrier–based) method predicts AR lifetimes that are $1 - 2$ orders of magnitude longer than those predicted by the interacting, exciton–based formalism (Eq. (5.5)). For example, the AR lifetime of the 4 ML ($L_z = 1.2$ nm) CdSe NPL with $L_x = 4$ nm and $L_y = 10$ nm has a calculated AR lifetime of ~ 3800 ps using the free carrier–based formalism and an AR lifetime of ~ 90 ps using the exciton–based formalism. Figure 5.3 also highlights the general accuracy of the atomistic electronic structure calculations. Specifically, exciton–based AR lifetime (green circles) calculations appear to provide quantitative agreement compared to our measurements (black squares) and previous measurements (blue and brown squares).[8,9] Importantly, both theory and experiments predict an increase in the AR lifetime as the area of the NPL increases for $A \leq 100$ nm^2. For larger lateral areas, at this point not accessible by the current theory, there seems to be a change in behavior in some of the experiments (see discussion below).

The disagreement between the free carrier–based and exciton–based formalisms arises from two primary reasons. The first is that the attractive Coulomb interaction that is responsible for exciton formation between the band–edge electron and band–edge hole mixes in band–edge states that have large momentums into the lowest energy excitonic states which facilitates momentum conservation in Auger processes.[9,71] The second reason derives from the free carrier–based formalism neglecting the large electron–hole attractive interaction on the single exciton level. This leads to an overestimation of the exciton Bohr radius ($a_{\text{B,exc}}$) and the root–mean–square exciton radius ($r_{\text{e-h}} = \sqrt{\langle (\mathbf{r}_e - \mathbf{r}_h)^2 \rangle}$ where $\mathbf{r}_e$ and $\mathbf{r}_h$ are the coordinates of the electron and hole, respectively) when electron–hole interactions are ignored. Figure 5.4 shows that the noninteracting formalism predicts that $r_{\text{e-h}}$ is nearly proportional to the square root of the NPL area, and, in contrast, that $r_{\text{e-h}}$ is nearly independent of the NPL area when electron–hole interactions are taken into account by solving the Bethe-Salpeter equation as is done using the interacting formalism. This overestimation of $r_{\text{e-h}}$ by noninteracting formalisms leads to an underestimation of the Coulomb matrix elements in Eq. (5.6) and, thus, an overestimation of AR lifetimes by free carrier–based formalisms (Figure 5.3).

Transitioning now to the lateral area dependence of AR in NPLs, Figure 5.5 shows a nearly linear dependence of the AR lifetimes on the lateral area ($A = L_x L_y$) for 3, 4, and
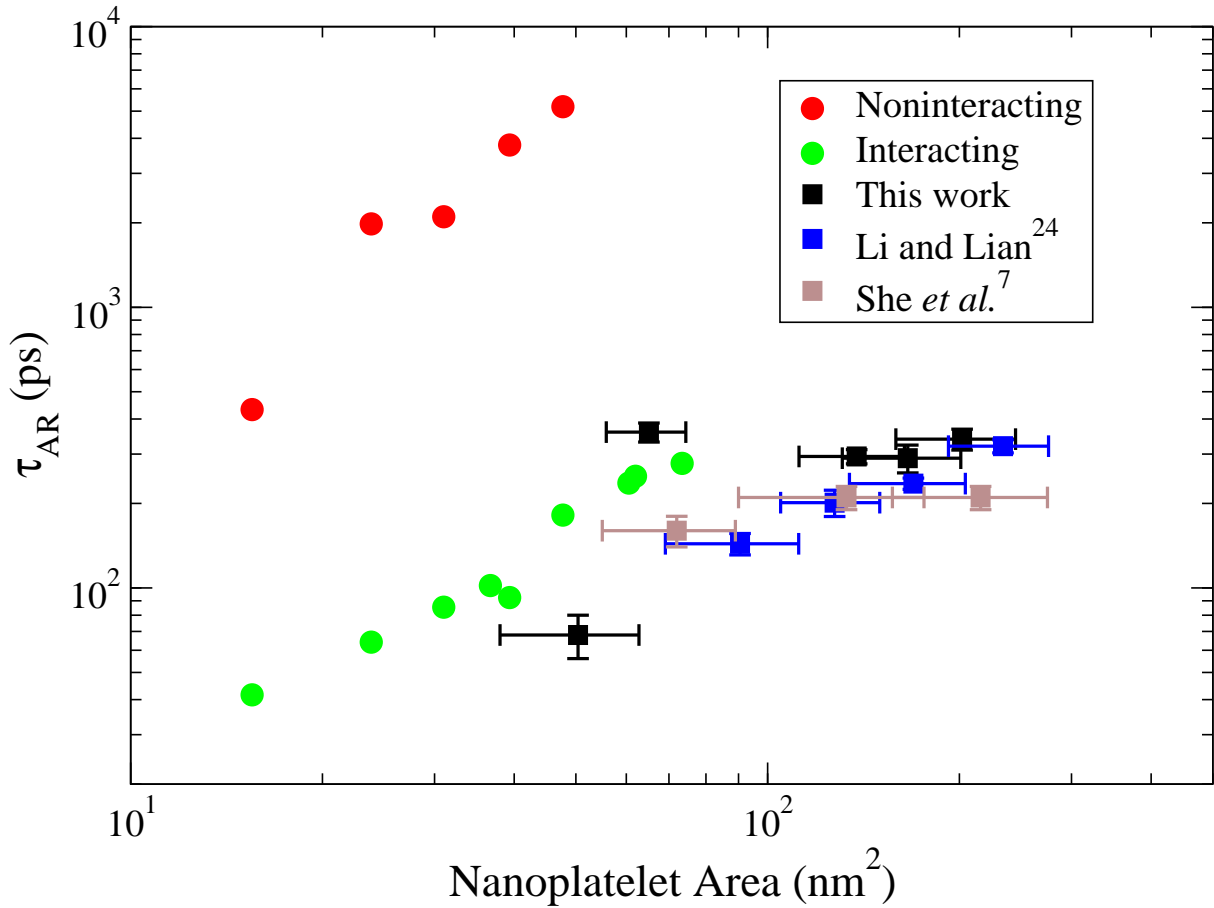
Figure 5.3: Biexciton Auger recombination lifetimes (τ_{AR}) for 4 ML CdSe NPLs calculated using both noninteracting, free carrier–based (red circles) and interacting, exciton–based (green circles) formalisms. The AR lifetimes predicted by the free carrier–based formalism are $1 - 2$ orders of magnitude longer than those predicted by the exciton–based formalism and those measured experimentally.[8,9] The experimentally measured lifetimes are shown using square symbols and calculated lifetimes are shown using circular symbols.
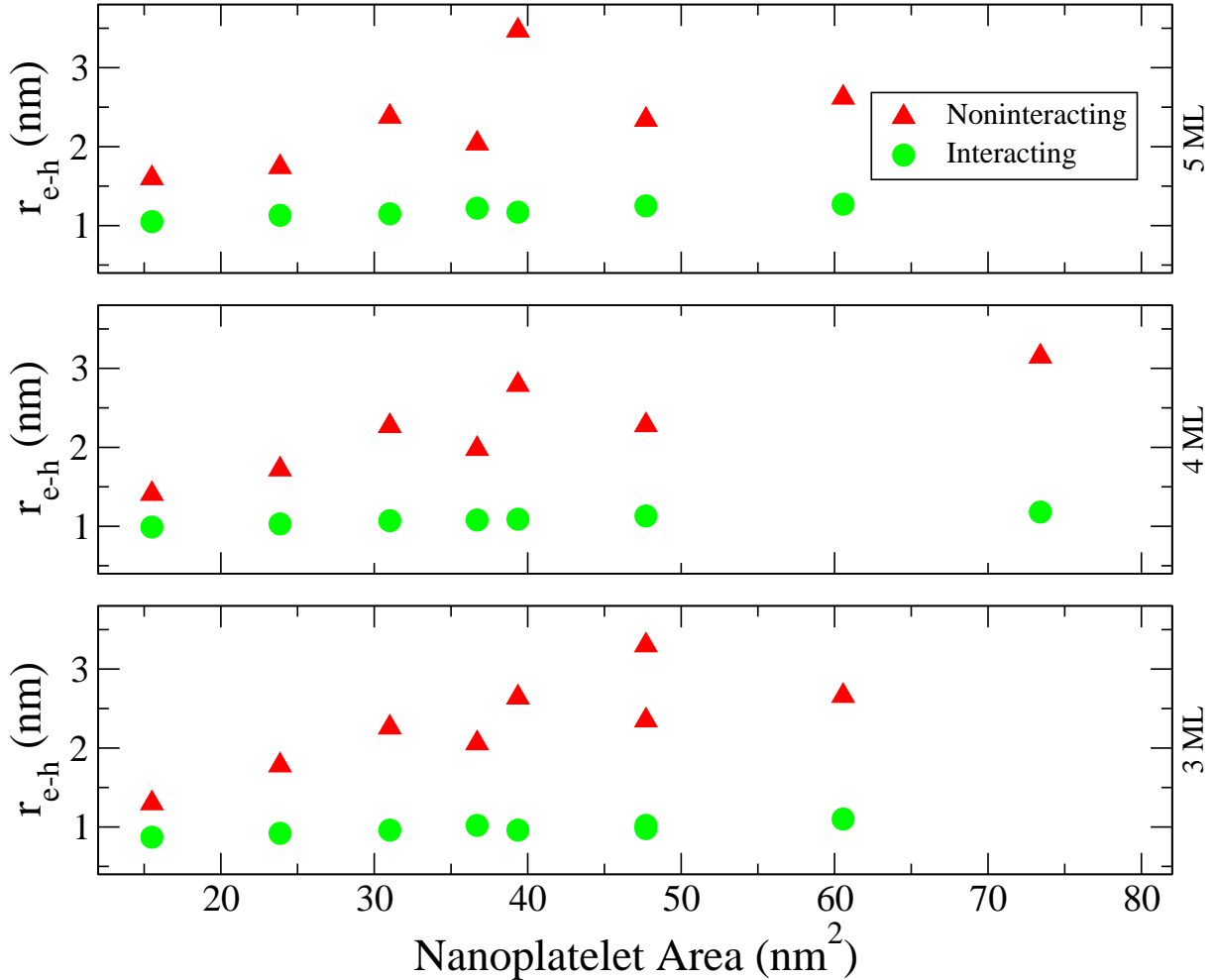
Figure 5.4: Root–mean–square exciton radii ($r_\text{e-h} = \sqrt{\langle(\mathbf{r}_\text{e} - \mathbf{r}_\text{h})^2\rangle}$) for 3 ML (bottom), 4 ML (middle), and 5 ML (top) thick CdSe NPLs as a function of the area of the NPLs. The red triangles show the calculated value using noninteracting (i.e. free–carrier) electron–hole pair states and the green circles show the calculated value using the interacting (i.e. excitonic) electron–hole pair states.

5 ML CdSe NPLs. The linear dependence on the NPL area is in agreement with recent experimental reports for both CdSe NPLs and CsPbBr$_3$ perovskite NPLs.[9,93] Interestingly, both the coherent scattering mechanism used in our calculations and the exciton diffusion–based model[9] described previously lead to linear dependencies with the lateral area.

The results of She *et al.*[8] are not necessarily at odds with this linear dependence. In fact, She *et al.* reported that the AR lifetime increases upon increasing the lateral area of 4 ML CdSe NPLs from 72 nm^2 to 133 nm^2, which is consistent with results presented in this work for the size regime that we focus on ($A \leq 100$ nm^2). At larger areas, She *et al.*

reported a plateau of the AR lifetime, whereas Li and Lian[9] do not observe a plateauing of the AR lifetime, even for NPLs with lateral areas greater than 200 nm^2. At this point, our computational technology is still limited to the size regime of $A \leq 100$ nm^2 and further developments are required to address larger areas.

The last main result (before we discuss the results in detail) is that of the thickness dependence of AR in NPLs. An important aim of this work was to determine and understand the prediction of the exciton–based, interacting formalism for the thickness (L_z) dependence of AR in CdSe NPLs. The only previous experimental work on this found a seventh power dependence ($\tau_{AR} \propto L_z^7$). Figure 5.6 shows the calculated AR lifetime as a function of the thickness for six different lateral dimensions that were kept fixed upon changing the thickness. The power law fits for each set of three thicknesses studied here (corresponding to 3, 4, and 5 MLs) give a calculated AR lifetime dependence on the thickness ranging from 0.6 to 1.6 ($\tau_{AR} \propto L_z^{0.6-1.6}$). While this is a rather large range of power dependence on thickness, it is certainly a milder dependence than reported previously.[9] In fact, it is rather close to the scaling that would be predicted by the universal volume scaling law (i.e. $\tau_{AR} \propto L_z^{1.0}$). The increase of the AR lifetime upon increasing NPL thickness is intuitive as thinner NPLs have larger exciton binding energies and smaller exciton Bohr radii. Both of these result in an increase of the Coulomb coupling matrix elements which overtakes the decrease in the density of states, thus leading to shorter AR lifetimes for thinner NPLs.

Experimentally, it is difficult to perform a systematic study of the thickness dependence, as control over NPL lateral area is more difficult to achieve than thickness control. In particular, 3 ML NPLs tend to have larger lateral dimensions than those of 4 and 5 ML CdSe NPLs using presently available syntheses, making it difficult to compare thickness independent of lateral area.[8,148,149] That being said, we determined AR lifetimes for many 4 and 5 ML CdSe NPLs and consistently found longer AR lifetimes for the 5 ML NPLs, which is also consistent with the work of She *et al.*[8] and Li and Lian.[9] Therefore, we conclude that AR lifetimes increase upon increasing thickness based on our experimental measurements and calculations; however, we believe that the dependence on the thickness is milder than previously reported.[9]

We begin the discussion of the lateral area dependence of AR lifetimes predicted by our Coulomb–mediated scattering approach by introducing an important concept of the exciton coherence area (A_{exc}) and its lateral area dependence in CdSe NPLs. The exciton coherence area is a measure of the area over which the center of mass of the exciton undergoes coherent motion.[150,151] An implicit assumption of our model (Eq. (5.5)) is that the two excitonic states that comprise the initial biexcitonic state are coherent throughout the NPL. This is shown pictorially in Figure 5.7. Specifically, the electron (red) and hole (blue) densities without (top panel) and with (bottom panel) electron–hole interactions included in the calculation of the low lying excitonic states are shown for a 3 ML ($L_z = 0.91$ nm) CdSe NPL with $L_x = L_y = 8$ nm. It can be seen in Figure 5.7 that in both the noninteracting and interacting cases the electron and hole densities look similar: they both are delocalized over almost the entire NPL area and the electron density is composed primarily of S–type atomic orbitals and the hole density is composed primarily of P–type atomic orbitals. The delocalization
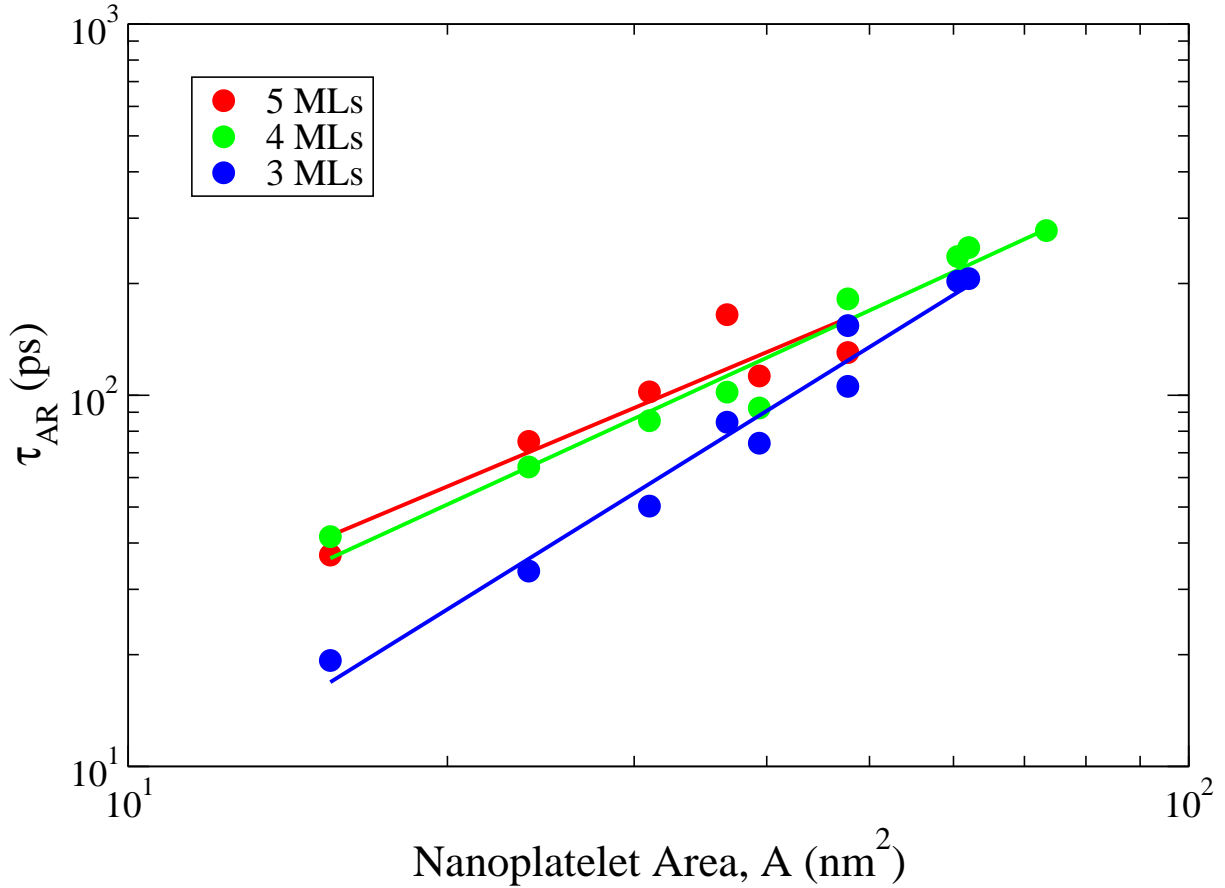
Figure 5.5: Auger recombination lifetimes, τ_{AR}, for CdSe NPLs as a function of the area of the NPL. Power law fits, $\tau_{\mathrm{AR}} \propto A^{\alpha}$, are also shown for each set of AR lifetimes with $\alpha = 1.2, 1.3$, and 1.8 in descending ML thickness.

of their projected densities and similar spatial extent suggest that the exciton center–of–mass coherence area is similar and is almost equal to the entire size of the NPL. This result makes sense as our calculations were performed with the 0 K atomic configuration and, even if considered at room temperature, the exciton coherence area measured experimentally is greater than or equal to the NPL areas for which we have calculated AR lifetimes.[151,152]

The fact that the exciton is coherent throughout the entire NPL highlights the wave–like nature of electron–hole pairs in CdSe NPLs. As a side note, this wave–like nature of electron–hole pairs is also very important in single exciton decay as it, together with the small average electron–hole separations shown in Figure 5.4, is responsible for the giant oscillator strengths of NPLs as the radiative decay rate is proportional to the ratio of the exciton coherence area to the square of the exciton Bohr radius.[127,133,153,154] In terms of our calculations of AR lifetimes, the linear dependence of the AR lifetime on the lateral area observed in our calculations arises from the Coulomb coupling between initial biexcitonic
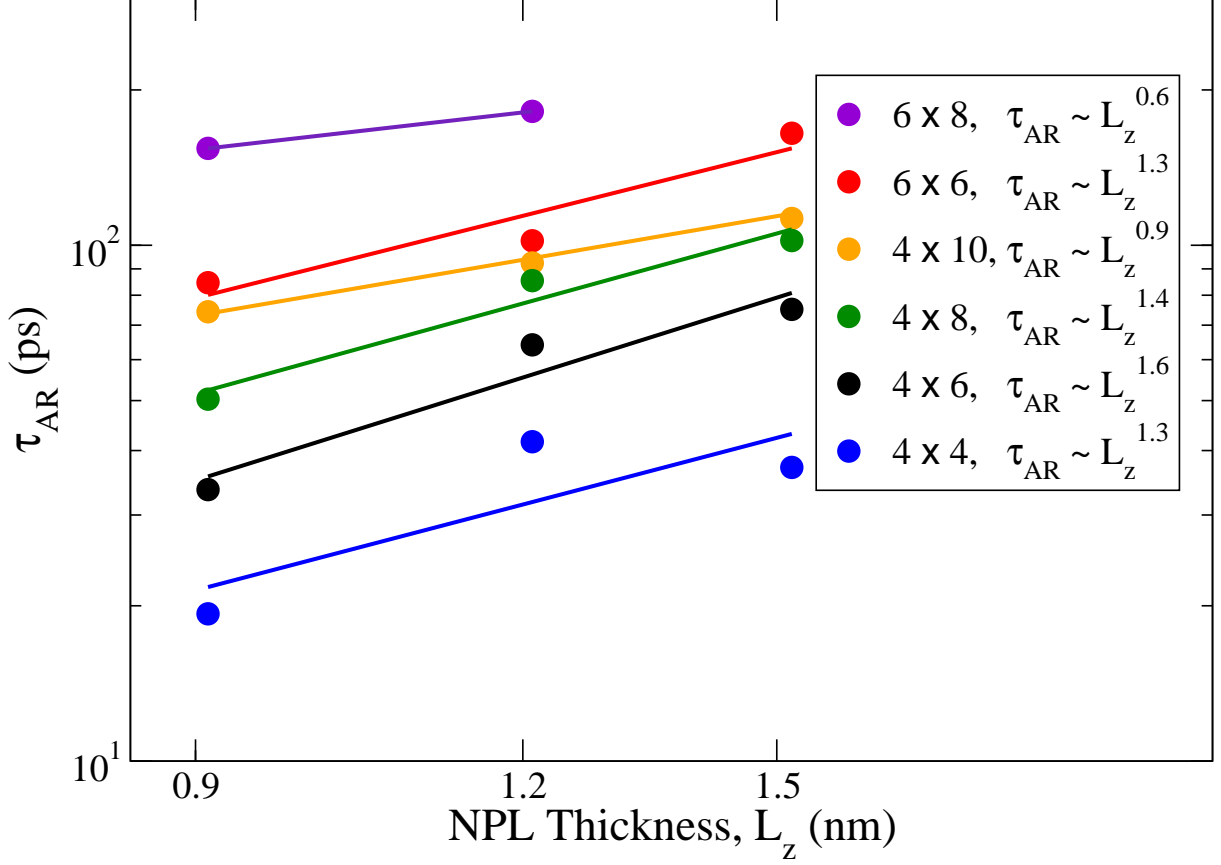
Figure 5.6: Auger recombination lifetimes (τ_{AR}) for CdSe NPLs as a function of the thickness of the NPL. Power law fits, $\tau_{AR} \propto L_z^\gamma$, are also shown for each set of AR lifetimes. The lateral dimensions are shown as $L_x \times L_y$ in nm.

states and final excitonic states decreasing upon increasing area and not from the collision frequency of the two excitons decreasing upon increasing area as previously used to explain the measured linear area dependence.[9,93] Thus, the measurement of a linear area dependence cannot distinguish between the two mechanisms, and the coherent mechanism developed here is an alternative picture that seems consistent with the exciton coherent areas of the CdSe NPLs studied in this work ($A \leq 100$ nm^2).[151,152]

Switching our focus to the disagreement with an earlier report that measured area–independent AR lifetimes,[8] the question that arises is why the exciton–based formalism given in Eq. (5.5) predicts a linear dependence and not an area independent AR lifetime? This can be addressed by analyzing the initial biexcitonic states. In Eq. (5.5), the initial biexcitonic state is given by

$$|B\rangle^{\text{exc}} = \sum_{b,j} \sum_{c,k} c_{b,j} c_{c,k} a_b^\dagger a_j a_c^\dagger a_k |0\rangle \otimes |\chi_B\rangle, \tag{5.10}$$
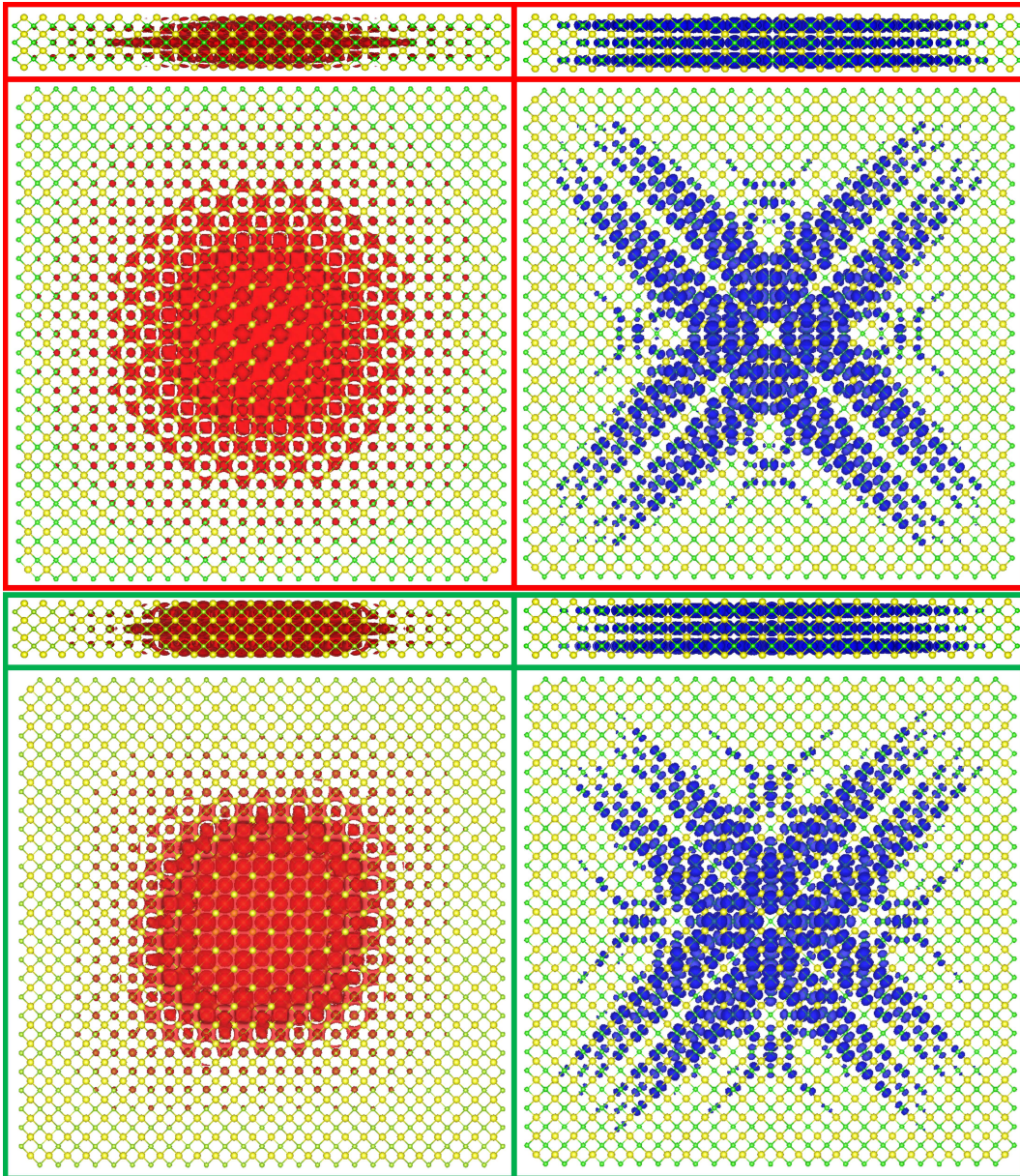
Figure 5.7: Electron (red) and hole (blue) carrier densities for the lowest lying noninteracting (top, red box) and interacting (bottom, green box) excitonic state for a 3 ML ($L_z = 0.91$ nm) CdSe nanoplatelet with $L_x = L_y = 8$ nm. The quasiparticle densities are integrated over all possible locations of the other quasiparticle for the interacting (i.e. correlated electron–hole pair state). The densities are visualized by looking down the x–axis and z–axis to show that the exciton coherence areas extend throughout a majority of the NPLs and the total area does not change much upon inclusion of electron–hole correlations.

where $|B\rangle^{\mathrm{exc}}$ denotes the initial biexcitonic state within the exciton–based (interacting) formalism and $|\chi_B\rangle$ is the spin part of the biexciton. Eq. (5.10) does not include spatial correlations between the excitonic states; correlations are only included within the single excitons by the two index coefficients ($c_{b,j}$ and $c_{c,k}$). On the other hand, a fully–correlated biexcitonic state,

$$|B\rangle^{\mathrm{biexc}} \;\; = \;\; \sum_{b,j,c,k} c_{b,j,c,k} a_b^\dagger a_j a_c^\dagger a_k \, |0\rangle \otimes |\chi_B\rangle \,, \tag{5.11}$$

includes spatial correlations between all four quasiparticles by using four index coefficients, ($c_{b,j,c,k}$). Unfortunately, the calculation of the four index coefficients in Eq. (4) is currently not feasible for NPLs. However, the biexciton binding energy is believed to be comparable to $k_{\mathrm{B}}T$ at room temperature where k_{B} is the Boltzmann constant and T is the temperature in CdSe nanocrystals[155] and quasi–2D materials,[8,156] implying that two excitons do not bind to form a stable biexciton. Thus, the combination of large coherence lengths of single excitons on the order of hundreds of nanometers in II–VI 2D materials[150] and the relatively small biexciton binding energies should make Eq. (5.10) a good approximation of the initial biexcitonic states involved in AR. If, on the other hand, the biexciton binding energy were large[8,44,157] and the lateral dimensions of the NPL were larger than the biexciton Bohr radius, then one could imagine that the initial biexcitonic state would stop changing as the NPL lateral dimensions increase beyond the biexciton Bohr radius. This could lead to a plateauing of the AR lifetime with increasing lateral area. Currently, it is unclear if this is the regime the experiments have been in ($A \sim 200$ nm^2 and $T = 298$ K).

A brief discussion of the thickness dependence of AR will now be given. An important aspect of the calculations shown in Figure 5.6 is that the dielectric constant (ϵ) used to obtain the coefficients ($c_{c,k}^B$) in Eq. (5.7) by solving the Bethe–Salpeter equation was set to a fixed value of 5 for all NPLs. We believe that the use of $\epsilon = 5$ is justified because the screening in the Bethe–Salpeter equation arises from the electron motion (i.e., not the ions) and the larger optical gap of confined systems combine to reduce the screening compared to bulk CdSe. That being said, we calculated the AR lifetime for NPLs with $L_x = L_y = 6$ nm for the three thicknesses ($L_z = 0.91, 1.21, 1.52$ nm) for dielectric constants ranging from 4 to 6 to test if these changes in the dielectric constant would change the predicted thickness dependence of AR lifetimes in CdSe NPLs. If we were to assume that the dielectric constants were 4 for 3 ML NPLs, 5 for 4 ML NPLs, and 6 for 5 ML NPLs, the thickness dependence is $\tau_{\mathrm{AR}} \propto L_z^2$, suggesting that dielectric changes can make the thickness dependence of AR lifetimes a bit steeper in NPLs. However, this is a far from comprehensive study on how the dielectric constant changes as a function of NPL thickness and how these changes impact AR lifetimes. Furthermore, our calculations neglect the dielectric mismatch between the NPLs and the surrounding environment, which is known to have important consequences on the electronic structure of excitons in NPLs.[128,130,158] Altogether, this suggests a more detailed investigation of the impact of dielectric changes and dielectric mismatch on AR lifetimes in nanomaterials along with more experiments to better understand the scaling with respect to the NPL thickness.

In summary, we report the first atomistic, electronic structure based calculations of AR lifetimes in quasi–2D NPLs. We find that electron–hole correlations in the initial biexcitonic state are necessary to obtain AR lifetimes that are in agreement with experimental measurements. The AR lifetimes show an increase with the lateral area for NPLs in the regime $A \leq 100$ nm^2 according to both our theory and current and previous measurements.[8,9] For larger lateral areas ($A \geq 150$ nm^2), not accessible by current computational technology, two distinct behaviors were observed. The current work suggests that AR lifetimes plateau with increasing area, consistent with the measurements of She *et al.*,[8] while previous experiments observed a linear increase with area.[9,93] The linear increase of the AR lifetime with area was previously explained using an exciton diffusion–based mechanism.[9,93] Our theory provides an alternative explanation based on a coherent scattering mechanism that seems consistent with exciton coherent lengths in CdSe NPLs[152] and shows a nearly linear increase of AR lifetimes with lateral area. In addition, we find that the AR lifetimes depend on the NPL thickness with a power law of L_z^{1-2}, depending on the shape of the NPL, which is milder than previously reported.[9] This milder thickness dependence together with the nearly linear lateral area dependence are consistent with the universal volume scaling law observed in quasi–0D quantum dots and quasi–1D nanorods.[3,4,76,92]

Chapter 6

Methods

6.1 Atomic configurations

Quantum dots and nanorods

The nanostructure configurations were obtained by cleaving a sufficiently large wurtzite crystal with a lattice constant of bulk wurtzite CdSe $\left(a = 4.30\,\text{Å},\ c = a\sqrt{\frac{8}{3}}\right)$ such that all Cd and Se atoms have at least two bonds. For the electronic structure calculations, dangling bonds on the nanostructure surface must be passivated by ligand potentials. These ligand potentials (details in Ref. 81) were placed in the correct geometry by using the positions of the outermost monolayer of Cd and Se atoms and replacing each Cd (Se) atom by a ligand potential for Se (Cd). Details on the sizes of the QD and NR configurations are given in Table 6.1 and Table 6.2, respectively.

Core/shell quantum dots

The nanostructure configurations were obtained by initially cleaving a sufficiently large wurtzite crystal with a lattice constant of bulk wurtzite CdSe $\left(a = 4.30\,\text{Å},\ c = a\sqrt{\frac{8}{3}}\right)$ such that all Cd, Zn, S and Se atoms have at least two bonds. Because of the lattice mismatch between CdSe and the CdS or ZnS shells, we relaxed the atomic coordinates of the core/shell quantum dots (QDs) prior to performing the electronic structure calculations. Specifically, we utilized molecular dynamics (MD) minimization of the core/shell QDs using the conjugate gradient algorithm. We used LAMMPS with Stillinger–Weber interaction potentials, which were previously developed for Cd, Zn, Se, S heterostructures, to obtain the minimized CdSe/CdS and CdSe/ZnS core/shell QD configurations.[106,159] In the next step, we passivated the MD minimized structures by using ligand potentials that were taken from Ref. 81. The ligand potentials were placed in the correct location by utilizing the atomic posi-

Configuration	Diameter (nm)	Volume (nm^3)
$Cd_{20}Se_{19}$	1.23	0.97
$Cd_{35}Se_{41}$	1.58	2.06
$Cd_{41}Se_{45}$	1.73	2.70
$Cd_{80}Se_{78}$	2.05	4.54
$Cd_{84}Se_{84}$	2.11	4.89
$Cd_{139}Se_{141}$	2.54	8.55
$Cd_{163}Se_{153}$	2.59	9.05
$Cd_{202}Se_{208}$	2.81	11.59
$Cd_{226}Se_{221}$	2.94	13.33
$Cd_{313}Se_{302}$	3.22	17.51
$Cd_{397}Se_{395}$	3.48	22.05
$Cd_{585}Se_{575}$	3.98	32.89
$Cd_{639}Se_{642}$	4.21	39.13
$Cd_{750}Se_{750}$	4.33	42.54
$Cd_{858}Se_{850}$	4.50	47.67
$Cd_{1104}Se_{1105}$	4.89	61.31
$Cd_{1358}Se_{1360}$	5.28	76.94

Table 6.1: CdSe quantum dot configuration details.

Configuration	Diameter (nm)	Length (nm)	Volume (nm^3)
$Cd_{133}Se_{145}$	1.53	5.12	9.42
$Cd_{202}Se_{197}$	1.53	7.49	13.77
$Cd_{266}Se_{273}$	1.53	10.04	18.46
$Cd_{406}Se_{411}$	1.53	15.21	27.97
$Cd_{544}Se_{539}$	1.53	20.12	37.01
$Cd_{672}Se_{677}$	1.53	25.04	46.04
$Cd_{810}Se_{805}$	1.53	29.95	55.08
$Cd_{299}Se_{301}$	2.14	5.38	19.26
$Cd_{421}Se_{419}$	2.14	7.49	26.80
$Cd_{539}Se_{541}$	2.14	9.59	34.35
$Cd_{859}Se_{861}$	2.14	15.21	54.46
$Cd_{1141}Se_{1139}$	2.14	20.12	72.05
$Cd_{548}Se_{547}$	2.89	5.38	35.19
$Cd_{766}Se_{767}$	2.89	7.49	48.97
$Cd_{1132}Se_{1131}$	2.89	11.00	71.93

Table 6.2: CdSe nanorod configuration details.

Configuration	Shell MLs	Diameter (nm)	Volume (nm^3)
$Cd_{462}Se_{462}$	0	3.8	30.1
$Cd_{462}Se_{462}/Cd_{735}S_{735}$	2	5.4	83.7
$Cd_{462}Se_{462}/Cd_{1326}S_{1326}$	3	6.2	127.2
$Cd_{462}Se_{462}/Cd_{2085}S_{2085}$	4	7.1	183.8
$Cd_{462}Se_{462}/Cd_{3033}S_{3033}$	5	7.9	255.6

Table 6.3: CdSe/CdS quantum dot configuration details for core/shell quantum dots with core diameters of 3.8 nm.

Configuration	Shell MLs	Diameter (nm)	Volume (nm^3)
$Cd_{102}Se_{102}$	0	2.2	5.2
$Cd_{102}Se_{102}/Cd_{120}S_{120}$	1	2.9	13.2
$Cd_{102}Se_{102}/Cd_{333}S_{333}$	2	3.7	27.6
$Cd_{102}Se_{102}/Cd_{651}S_{651}$	3	4.6	49.8
$Cd_{102}Se_{102}/Cd_{1095}S_{1095}$	4	5.4	81.7
$Cd_{102}Se_{102}/Cd_{1686}S_{1686}$	5	6.2	125.1
$Cd_{102}Se_{102}/Cd_{2445}S_{2445}$	6	7.0	181.7
$Cd_{102}Se_{102}/Cd_{4551}S_{4551}$	8	8.7	341.8

Table 6.4: CdSe/CdS quantum dot configuration details for core/shell quantum dots with core diameters of 2.2 nm.

tions of the extra outermost monolayer of Se/S and Cd/Zn atoms and replacing each Se/S (Cd/Zn) atom by a corresponding ligand potential for Cd/Zn (Se/S). Details on the sizes of the core/shell QD configurations are given in Table 6.3, Table 6.4, and Table 6.5.

Strained CdSe quantum dots and nanoplatelets

Strained CdSe/ZnS quantum dots

For the strained CdSe QD nanostructures, MD minimizations were performed with ZnS shells using the aforementioned procedure, and, afterwards, all of the Zn and S atoms were removed from the shell such that the final configuration was that of just the CdSe QD but with strained positions. The results of this procedure for varying amounts of ZnS MLs are shown in Table 6.6. Because ZnS has a smaller lattice constant than CdSe, the strain is

Configuration	Shell MLs	Diameter (nm)	Volume (nm^3)
Cd$_{102}$Se$_{102}$	0	2.2	5.2
Cd$_{102}$Se$_{102}$/Zn$_{120}$S$_{120}$	1	2.8	11.7
Cd$_{102}$Se$_{102}$/Zn$_{333}$S$_{333}$	2	3.5	23.3
Cd$_{102}$Se$_{102}$/Zn$_{651}$S$_{651}$	3	4.3	41.1
Cd$_{102}$Se$_{102}$/Zn$_{1095}$S$_{1095}$	4	5.0	66.5
Cd$_{102}$Se$_{102}$/Zn$_{1686}$S$_{1686}$	5	5.8	101.1
Cd$_{102}$Se$_{102}$/Zn$_{2445}$S$_{2445}$	6	6.5	146.2
Cd$_{102}$Se$_{102}$/Zn$_{4551}$S$_{4551}$	8	8.1	273.9

Table 6.5: CdSe/ZnS quantum dot configuration details for core/shell quantum dots with core diameters of 2.2 nm.

Configuration	ZnS MLs in MD	$\langle r_{\text{Cd-Se}} \rangle$ (nm)	Diameter (nm)	Volume (nm^3)
Cd$_{93}$Se$_{93}$	0	2.620	2.155	5.242
Cd$_{93}$Se$_{93}$	1	2.545	2.078	4.702
Cd$_{93}$Se$_{93}$	2	2.533	2.068	4.634
Cd$_{93}$Se$_{93}$	4	2.521	2.059	4.569
Cd$_{93}$Se$_{93}$	8	2.520	2.056	4.552

Table 6.6: Configuration details of the strained CdSe QDs. The quantum dots average Cd–Se bond lengths ($\langle r_{\text{Cd-Se}} \rangle$), diameters, and volumes are given in nm, nm, and nm^3, respectively.

compressive in all dimensions and results in smaller average Cd–Se bonds ($\langle r_{\text{Cd-Se}} \rangle$) and diameters in the strained CdSe QDs relative to the unstrained CdSe QD.

This procedure allowed us to isolate the impact of the compressive strain, which is induced by the ZnS shell, has on the Auger recombination lifetime (τ_{AR}). Table 6.7 shows how the addition of the compressive strain results in a reduction of τ_{AR} by about a factor of 2, and the reduction primarily arises from the hole channel. In other words, the Auger recombination channel in which the hole receives a majority of the additional energy ($\tau_{\text{AR,h}}$) becomes faster when the core is compressed. The electron channel lifetime ($\tau_{\text{AR,e}}$) also becomes faster, but not significantly in comparison to the hole channel (Table 6.7).

In order to understand the decrease in the hole channel Auger recombination lifetime, we analyzed the Coulomb matrix elements (V_{ijck}) and number of final states ($n_{\text{h,final}}$) in each of these CdSe QDs in a noninteracting formalism to simplify the analysis. Interestingly, we found that the major difference arises from an increase in the Coulomb matrix elements (V_{ijck}). Specifically, the average of the square of the Coulomb matrix elements ($\langle V_{ijck}^2 \rangle$) is approximately twice as large in the strained CdSe QDs (bottom four lines in Table 6.8) compared to the unstrained CdSe QD (top line of Table 6.8). A similar increase of the Coulomb matrix elements in the electron channel (V_{abck}) is not observed. This suggests that the increase of the Coulomb matrix elements in the hole channel arises from the $\phi_i(\mathbf{r}) \phi_j(\mathbf{r})$ part of the Eq. (3.3) as both the electron and hole channels contain $\phi_c(\mathbf{r}') \phi_k(\mathbf{r}')$. The

Configuration	ZnS MLs in MD	τ_{AR} (ps)	$\tau_{\mathrm{AR,h}}$ (ps)	$\tau_{\mathrm{AR,e}}$ (ps)
$Cd_{93}Se_{93}$	0	4.6	8.7	9.8
$Cd_{93}Se_{93}$	1	2.0	3.2	5.5
$Cd_{93}Se_{93}$	2	2.0	3.2	5.7
$Cd_{93}Se_{93}$	4	2.4	3.6	6.9
$Cd_{93}Se_{93}$	8	2.6	3.8	7.6

Table 6.7: Auger recombination lifetimes the strained CdSe QDs. The total Auger recombination lifetime (τ_{AR}), Auger recombination lifetime of the hole channel ($\tau_{\mathrm{AR,h}}$), and the Auger recombination lifetime of the electron channel ($\tau_{\mathrm{AR,e}}$) are given in picoseconds (ps).

Configuration	ZnS MLs used in MD	$n_{\mathrm{h,final}}$	$\langle V_{ijck}^2 \rangle$ (a.u.)	$n_{\mathrm{e,final}}$	$\langle V_{abck}^2 \rangle$ (a.u.)
$Cd_{93}Se_{93}$	0	27	1.0	16	1.0
$Cd_{93}Se_{93}$	1	22	2.0	17	1.1
$Cd_{93}Se_{93}$	2	22	2.1	19	1.1
$Cd_{93}Se_{93}$	4	22	2.4	16	1.1
$Cd_{93}Se_{93}$	8	22	2.5	16	1.1

Table 6.8: The number of final high energy hole ($n_{\mathrm{h,final}}$) and electron ($n_{\mathrm{e,final}}$) states that satisfy energy conservation along with the average of the squared Coulomb matrix elements that couple to the high energy hole and electron states, respectively, in a noninteracting Auger recombination lifetime calculation. The average of the squared Coulomb matrix elements is normalized to the unstrained (top line) value.

$\phi_i(\mathbf{r})\,\phi_j(\mathbf{r})$ is a product of the initial band–edge hole state ($\phi_j(\mathbf{r})$) with the final high energy hole state ($\phi_i(\mathbf{r})$). We speculate that the compressive strain increases the rate of the hole channel decay by increasing the oscillatory nature of the band–edge hole states, which leads to better overlap with the highly oscillatory final high energy hole states.

Strained CdSe/CdS quantum dots and nanoplatelets

6.2   Free carrier states

All calculations were preformed within the semi–empirical pseudopotential method for CdSe (Ref. 81) implemented on real–space grids with spacings of at most 0.8 a.u. – sufficient to converge the results. Ligand potentials were used to passivate the surface atoms with dangling bonds. The ligand potentials taken from Ref. 81.

The first step in both the noninteracting and interacting formalisms calculations of an AR lifetime was to apply the filter–diagonalization technique to obtain the band–edge quasi-

Configuration	CdS MLs	Thickness (nm)	Length (nm)	Width (nm)
$Cd_{1019}Se_{800}$	0	1.21	6.06	6.06
$Cd_{1019}Se_{800}/Cd_{xx}S_{xx}$	1	1.81	5.93	5.93
$Cd_{1019}Se_{800}/Cd_{xx}S_{xx}$	2	2.39	5.93	5.93
$Cd_{1019}Se_{800}/Cd_{xx}S_{xx}$	3	2.97	5.92	5.92
$Cd_{1019}Se_{800}/Cd_{xx}S_{xx}$	4	3.56	5.92	5.92
Strained $Cd_{1019}Se_{800}$	0	1.23	5.92	5.92

Table 6.9: Configuration details of the strained CdSe/CdS NPLs.

Configuration	CdS MLs	Diameter (nm)
$Cd_{408}Se_{429}$	0	3.53
$Cd_{408}Se_{429}/Cd_{451}S_{434}$	1	4.43
$Cd_{408}Se_{429}/Cd_{xx}S_{xx}$	2	5.07
$Cd_{408}Se_{429}/Cd_{xx}S_{xx}$	3	5.83
$Cd_{408}Se_{429}/Cd_{xx}S_{xx}$	4	6.30
Strained $Cd_{408}Se_{429}$	0	3.48

Table 6.10: Configuration details of the strained CdSe/CdS QDs.

particle states. This involved filtering electron and hole states at a target energy near the HOMO and LUMO energies using an interpolation polynomial of length $N_c \approx 4,096$ (a shorter interpolation polynomial could be used for the smaller nanostructures and longer interpolation polynomials were required for the largest nanostructures). The states obtained form this application of the filter–diagonalization technique were then immediately used to build the initial biexcitonic states in the noninteracting formalism or used as input to the Bethe–Salpeter equation before writing the initial biexcitonic states in the interacting formalism. To obtain the final excitonic states, we again filtered electron and hole states at energies resonant with the initial biexcitonic state using an interpolation polynomial of length $N_c \approx 8,192$ (a longer length needed here reflecting the greater density of quasiparticle states at high energies compared to the band–edge). For each interpolation polynomial filter we generated 10 electron states and 10 hole states. We then calculated the Coulomb coupling using the initial and final states and enforced energy conservation as discussed below to obtain AR lifetimes.

6.3 Excitonic states

The correlated electron–hole pair (excitonic) states used in the initial biexcitonic states in the interacting formalism were represented as a linear combination of noninteracting electron–hole pairs as discussed in detail in Ref. 36. The electron–hole kernel in the Bethe–Salpeter equation included both the screened direct Coulomb attraction and unscreened exchange–

like repulsive term, as the latter term is needed for bright excitons (i.e. excitons generated by a photon absorption) in CdSe nanostructures. The number of quasiparticle (electron and hole) states used to build the Bethe–Salpeter Hamiltonian varied from ~ 50 in the smaller systems to ~ 300 in the larger systems studied; we checked that the exciton energies and AR lifetimes were converged with respect to the number of quasiparticle states included in the Bethe–Salpeter equation.

6.4 Energy conservation in Auger recombination lifetime calculations

We enforced conservation of energy ($\delta \left(E_B - E_S \right)$) in Fermi's golden rule by approximating the delta function as:

$$\delta \left(x \right) \;\; = \;\; \begin{cases} \frac{1}{2dE} & -dE < x < dE \\ 0 & \text{otherwise} \end{cases}, \tag{6.1}$$

where dE is a parameter (i.e. all final single excitonic states with energies between $E_B \pm dE$ were taken to conserve energy). We reported AR lifetimes for $dE \approx 20$ meV – similar broadening to what was used in previous calculations.[72,76] Importantly, the conclusions discussed in the main text do not change for dE values ranging from $5 - 50$ meV.

Chapter 7

Summary

The first take home message of this dissertation is that the inclusion of the electron–hole interactions that are responsible for exciton formation is imperative if one wants to have the formalism predict quantitatively accurate Auger recombination (AR) lifetimes in quasi–0D quantum dots (QDs), quasi–1D nanorods (NRs), quasi–2D nanoplatelets (NPLs), and heterostructure nanomaterials (e.g. core/shell QDs).[76,146] This requirement is best summarized in Figure 7.1. Specifically, the interacting formalism (whether implemented deterministically or stochastically) models biexciton Auger recombination in a framework that is very similar to exciton–exciton annihilation and predicts quantitively accurate AR lifetimes, as indicated by the green arrow in Figure 7.1. The overestimation of AR lifetimes by noninteracting formalisms, as indicated by the red x in Figure 7.1, stems from the fact that the Coulomb matrix elements (Eq. (3.3)) in Eq. (2.4) are underestimated due to the lack of correlation between the initial electrons and holes in noninteracting formalisms.
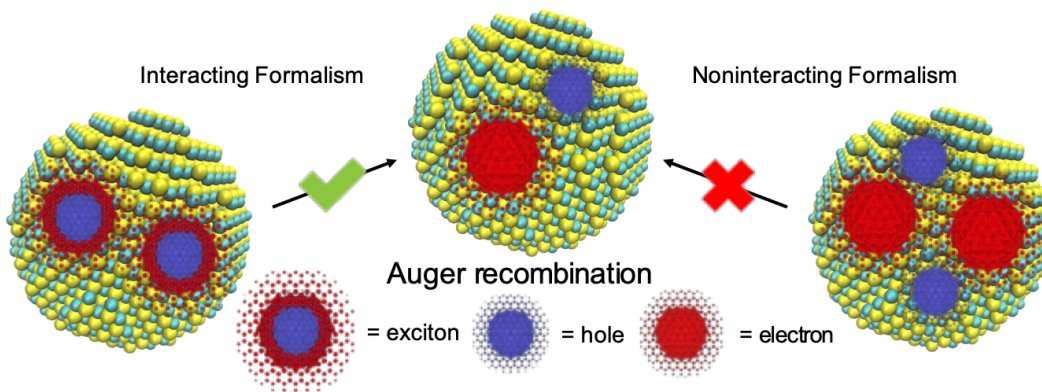

Figure 7.1: A pictorial representation of the decay of a biexcitonic state via an Auger recombination event in the interacting (left) and noninteracting (right) formalisms. The green checkmark (red x) arrow signifies that the formalism predicts accurate (inaccurate) Auger recombination lifetimes.

An important aspect of the quantitative accuracy of the interacting formalism (Eq. (2.7)) is that the accuracy is not limited to a specific size or dimensionality limit, as evidenced by its accuracy in the very strong and moderate confinement regimes for QDs and all size regimes studied thus far in NRs and NPLs. This generality resulted in the interacting formalism being the first theoretical and computational method to predict the "universal volume scaling law" of AR lifetimes in QDs and, furthermore, accurate AR lifetimes in NRs and NPLs.[3,16,76] Interestingly, the impact of electron–hole interactions is noticeable even in the rather strong confinement regime (radius of the QD being significantly less than the bulk exciton Bohr radius).[76] For NRs and NPLs, the approximate linear dependence of the AR lifetime with the weakly confined dimensions (i.e. NR length and NPL lateral area) predicted by the interacting formalism provides a new mechanism based on coherent scattering of excitons that can explain the experimental measurements showing a linear dependence of the AR lifetime with the NR length and NPL lateral area.[4,9,93]

In a broader context, this work exemplifies how electron–hole correlations are very important to the decay of multiexcitonic states in systems of reduced dimensionality – similar to had been found for the radiative decay of single excitons in 1D and 2D systems.[39,136] Additionally, the interacting formalism shows the similarity between Auger recombination discussed in the colloidal nanocrystal communities and that of exciton–exciton annihilation discussed in the 1D and 2D communities. In summary, this work unraveled details on how the size, shape, and composition of nanomaterials impacts the electronic and optical properties of the nanomaterials through the development and application of atomistic electronic structure methods.

Bibliography

[1] Jasieniak, J.; Califano, M.; Watkins, S. E. *ACS Nano* **2011**, *5*, 5888–5902.

[2] Franceschetti, A.; Zunger, A. *Phys. Rev. Lett.* **1997**, *78*, 915–918.

[3] Klimov, V. I.; Mikhailovsky, A. A.; McBranch, D. W.; Leatherdale, C. A.; Bawendi, M. G. *Science* **2000**, *287*, 1011–1013.

[4] Htoon, H.; Hollingsworth, J. A.; Dickerson, R.; Klimov, V. I. *Phys. Rev. Lett.* **2003**, *91*, 227401.

[5] Taguchi, S.; Saruyama, M.; Teranishi, T.; Kanemitsu, Y. *Phys. Rev. B* **2011**, *83*, 155324.

[6] Kong, D.; Jia, Y.; Ren, Y.; Xie, Z.; Wu, K.; Lian, T. *J. Phys. Chem. C* **2018**, *122*, 14091–14098.

[7] Zhu, H.; Lian, T. *J. Am. Chem. Soc.* **2012**, *134*, 11289–11297.

[8] She, C.; Fedin, I.; Dolzhnikov, D. S.; Dahlberg, P. D.; Engel, G. S.; Schaller, R. D.; Talapin, D. V. *ACS Nano* **2015**, *9*, 9475–9485.

[9] Li, Q.; Lian, T. *Nano Lett.* **2017**, *17*, 3152–3158.

[10] Ekimov, A. I.; Onushchenko, A. A. *Sov Phys Semicond* **1982**, *16*, 775–778.

[11] Rossetti, R.; Nakahara, S.; Brus, L. E. *J. Chem. Phys.* **1983**, *79*, 1086–1088.

[12] Ekimov, A. I.; Efros, A. L.; Onushchenko, A. A. *Solid State Commun.* **1985**, *56*, 921–924.

[13] Murray, C. B.; Norris, D. J.; Bawendi, M. G. *J. Am. Chem. Soc.* **1993**, *115*, 8706–8715.

[14] Alivisatos, A. P. *Science* **1996**, *271*, 933–937.

[15] Lohse, S. E.; Murphy, C. J. *J. Am. Chem. Soc.* **2012**, *134*, 15607–15620.

[16] Robel, I.; Gresback, R.; Kortshagen, U.; Schaller, R. D.; Klimov, V. I. *Phys. Rev. Lett.* **2009**, *102*, 177404.

[17] Peng, X.; Manna, L.; Yang, W.; Wickham, J.; Scher, E.; Kadavanich, A.; Alivisatos, A. P. *Nature* **2000**, *404*, 59–61.

[18] Kumar, S.; Nann, T. *Small* **2006**, *2*, 316–329.

[19] Costi, R.; Saunders, A. E.; Banin, U. *Angew. Chemie - Int. Ed.* **2010**, *49*, 4878–4897.

[20] Yin, Y.; Talapin, D. *Chem. Soc. Rev.* **2013**, *42*, 2484–2487.

[21] Van Embden, J.; Chesman, A. S.; Jasieniak, J. J. *Chem. Mater.* **2015**, *27*, 2246–2285.

[22] Cui, J.; Panfil, Y. E.; Koley, S.; Shamalia, D.; Waiskopf, N.; Remennik, S.; Popov, I.; Oded, M.; Banin, U. *Nat. Commun.* **2019**, *10*, 5401.

[23] Hazarika, A.; Fedin, I.; Hong, L.; Guo, J.; Srivastava, V.; Cho, W.; Coropceanu, I.; Portner, J.; Diroll, B. T.; Philbin, J. P.; Rabani, E.; Klie, R.; Talapin, D. V. *J. Am. Chem. Soc.* **2019**, *141*, 13487–13496.

[24] Utterback, J. K.; Grennell, A. N.; Wilker, M. B.; Pearce, O. M.; Eaves, J. D.; Dukovic, G. *Nat. Chem.* **2016**, *8*, 1061–1066.

[25] Giansante, C.; Infante, I. *J. Phys. Chem. Lett.* **2017**, *8*, 5209–5215.

[26] Califano, M. *J. Phys. Chem. C* **2008**, *112*, 8570–8574.

[27] Califano, M. *J. Phys. Chem. C* **2011**, *115*, 18051–18054.

[28] Califano, M.; Gómez-Campos, F. M. *Nano Lett.* **2013**, *13*, 2047–2052.

[29] Zhou, Q.; Cho, Y.; Yang, S.; Weiss, E. A.; Berkelbach, T. C.; Darancet, P. *Nano Lett.* **2019**, *19*, 7124–7129.

[30] Watson, B. R.; Doughty, B.; Calhoun, T. R. *Nano Lett.* **2019**, *19*, 6157–6165.

[31] Ondry, J. C.; Philbin, J. P.; Lostica, M.; Rabani, E.; Alivisatos, A. P. *ACS Nano* **2019**, *13*, 12322–12344.

[32] Hartley, C. L.; Dempsey, J. L. *Nano Lett.* **2019**, *19*, 1151–1157.

[33] Wannier, G. H. *Phys. Rev.* **1937**, *52*, 191.

[34] Dresselhaus, G. *J. Phys. Chem. Solids* **1956**, *1*, 14–22.

[35] Cohen, M. L.; Louie, S. G. *Fundamentals of Condensed Matter Physics*, 1st ed.; Cambridge University Press, 2016.

[36] Rohlfing, M.; Louie, S. G. *Phys. Rev. B* **2000**, *62*, 4927–4944.

[37] Sercel, P. C.; Efros, A. L. *Nano Lett.* **2018**, *18*, 4061–4068.

[38] Scholes, G. D.; Rumbles, G. *Nat. Mater.* **2006**, *5*, 683–696.

[39] Yang, L.; Spataru, C. D.; Louie, S. G.; Chou, M. Y. *Phys. Rev. B* **2007**, *75*, 201304.

[40] Ithurria, S.; Tessier, M. D.; Mahler, B.; Lobo, R. P.; Dubertret, B.; Efros, A. L. *Nat. Mater.* **2011**, *10*, 936–941.

[41] Klimov, V. I. *Annu. Rev. Condens. Matter Phys.* **2014**, *5*, 285–316.

[42] Olshansky, J. H.; Ding, T. X.; Lee, Y. V.; Leone, S. R.; Alivisatos, A. P. *J. Am. Chem. Soc.* **2015**, *137*, 15567–15575.

[43] Nanda, J.; Ivanov, S. A.; Htoon, H.; Bezel, I.; Piryatinski, A.; Tretiak, S.; Klimov, V. I. *J. Appl. Phys.* **2006**, *99*.

[44] Grim, J. Q.; Christodoulou, S.; Di Stasio, F.; Krahne, R.; Cingolani, R.; Manna, L.; Moreels, I. *Nat. Nanotechnol.* **2014**, *9*, 891–895.

[45] Pelton, M. *J. Phys. Chem. C* **2018**, *122*, 10659.

[46] Roh, J.; Park, Y. S.; Lim, J.; Klimov, V. I. *Nat. Commun.* **2020**, *11*, 271.

[47] Boles, M. A.; Engel, M.; Talapin, D. V. *Chem. Rev.* **2016**, *116*, 11220–11289.

[48] Colvin, V. L.; Schlamp, M. C.; Alivisatos, A. P. *Nature* **1994**, *370*, 354–357.

[49] Imamoglu, A.; Michler, P.; Mason, M. D.; Carson, P. J.; Strouse, G. F.; Buratto, S. K. *Nature* **2000**, *406*, 968–970.

[50] Pietryga, J. M.; Zhuravlev, K. K.; Whitehead, M.; Klimov, V. I.; Schaller, R. D. *Phys. Rev. Lett.* **2008**, *101*, 217401.

[51] Bae, W. K.; Padilha, L. A.; Park, Y. S.; McDaniel, H.; Robel, I.; Pietryga, J. M.; Klimov, V. I. *ACS Nano* **2013**, *7*, 3411–3419.

[52] Fathpour, S.; Mi, Z.; Bhattacharya, P.; Kovsh, A. R.; Mikhrin, S. S.; Krestnikov, I. L.; Kozhukhov, A. V.; Ledentsov, N. N. *Appl. Phys. Lett.* **2004**, *85*, 5164–5166.

[53] Sukhovatkin, V.; Hinds, S.; Brzozowski, L.; Sargent, E. H. *Science* **2009**, *324*, 1542–1544.

[54] Nair, G.; Zhao, J.; Bawendi, M. G. *Nano Lett.* **2011**, *11*, 1136–1140.

[55] Ben-Shahar, Y.; Philbin, J. P.; Scotognella, F.; Ganzar, L.; Cerullo, G.; Rabani, E.; Banin, U. *Nano Lett.* **2018**, *18*, 5211–5216.

[56] García-Santamaría, F.; Chen, Y.; Vela, J.; Schaller, R. D.; Hollingsworth, J. A.; Klimov, V. I. *Nano Lett.* **2009**, *9*, 3482–3488.

[57] Pijpers, J. J.; Milder, M. T.; Delerue, C.; Bonn, M. *J. Phys. Chem. C* **2010**, *114*, 6318–6324.

[58] Chepic, D. I.; Efros, A. L.; Ekimov, A. I.; Ivanov, M. G.; Kharchenko, V. A.; Kudriavtsev, I. A.; Yazeva, T. V. *J. Lumin.* **1990**, *47*, 113–127.

[59] Vaxenburg, R.; Rodina, A.; Shabaev, A.; Lifshitz, E.; Efros, A. L. *Nano Lett.* **2015**, *15*, 2092–2098.

[60] Vaxenburg, R.; Rodina, A.; Lifshitz, E.; Efros, A. L. *Nano Lett.* **2016**, *16*, 2503–2511.

[61] Cragg, G. E.; Efros, A. L. *Nano Lett.* **2010**, *10*, 313–317.

[62] Zavelani-Rossi, M.; Lupo, M. G.; Tassone, F.; Manna, L.; Lanzani, G. *Nano Lett.* **2010**, *10*, 3142–3150.

[63] García-Santamaría, F.; Brovelli, S.; Viswanatha, R.; Hollingsworth, J. A.; Htoon, H.; Crooker, S. A.; Klimov, V. I. *Nano Lett.* **2011**, *11*, 687–693.

[64] Park, Y. S.; Bae, W. K.; Padilha, L. A.; Pietryga, J. M.; Klimov, V. I. *Nano Lett.* **2014**, *14*, 396–402.

[65] Jain, A.; Voznyy, O.; Hoogland, S.; Korkusinski, M.; Hawrylak, P.; Sargent, E. H. *Nano Lett.* **2016**, *16*, 6491–6496.

[66] Jain, A.; Voznyy, O.; Korkusinski, M.; Hawrylak, P.; Sargent, E. H. *J. Phys. Chem. Lett.* **2017**, *8*, 3179–3184.

[67] Yang, J.; Hyun, B. R.; Basile, A. J.; Wise, F. W. *ACS Nano* **2012**, *6*, 8120–8127.

[68] Padilha, L. A.; Stewart, J. T.; Sandberg, R. L.; Bae, W. K.; Koh, W.-k.; Pietryga, J. M.; Klimov, V. I. *Nano Lett.* **2013**, *13*, 1092–1099.

[69] Aerts, M.; Spoor, F. C. M.; Grozema, F. C.; Houtepen, A. J.; Schins, J. M.; Siebbeles, L. D. A. *Nano Lett.* **2013**, *13*, 4380–4386.

[70] Stolle, C. J.; Lu, X.; Yu, Y.; Schaller, R. D.; Korgel, B. A. *Nano Lett.* **2017**, *17*, 5580–5586.

[71] Wang, F.; Wu, Y.; Hybertsen, M. S.; Heinz, T. F. *Phys. Rev. B* **2006**, *73*, 245424.

[72] Wang, L.-W.; Califano, M.; Zunger, A.; Franceschetti, A. *Phys. Rev. Lett.* **2003**, *91*, 056404.

[73] Korkusinski, M.; Voznyy, O.; Hawrylak, P. *Phys. Rev. B* **2011**, *84*, 155327.

[74] Patton, B.; Langbein, W.; Woggon, U. *Phys. Rev. B* **2003**, *68*, 125316.

[75] Balan, A. D.; Eshet, H.; Olshansky, J. H.; Lee, Y. V.; Rabani, E.; Alivisatos, A. P. *Nano Lett.* **2017**, *17*, 1629–1636.

[76] Philbin, J. P.; Rabani, E. *Nano Lett.* **2018**, *18*, 7889–7895.

[77] Refaely-Abramson, S.; Da Jornada, F. H.; Louie, S. G.; Neaton, J. B. *Phys. Rev. Lett.* **2017**, *119*, 267401.

[78] Eshet, H.; Grünwald, M.; Rabani, E. *Nano Lett.* **2013**, *13*, 5880–5885.

[79] Wang, L. W.; Zunger, A. *J. Phys. Chem.* **1994**, *98*, 2158–2165.

[80] Wang, L.-W.; Zunger, A. *Phys. Rev. B* **1996**, *53*, 9579–9582.

[81] Rabani, E.; Hetenyi, B.; Berne, B. J.; Brus, L. E. *J. Chem. Phys.* **1999**, *110*, 5355–5369.

[82] Williamson, A.; Zunger, A. *Phys. Rev. B* **2000**, *61*, 1978–1991.

[83] Wall, M. R.; Neuhauser, D. *J. Chem. Phys.* **1995**, *102*, 8011–8022.

[84] Toledo, S.; Rabani, E. *J. Comput. Phys.* **2002**, *180*, 256–269.

[85] Shabaev, A.; Efros, A. L. *Nano Lett.* **2004**, *4*, 1821–1825.

[86] Cohn, A. W.; Schimpf, A. M.; Gunthardt, C. E.; Gamelin, D. R. *Nano Lett.* **2013**, *13*, 1810–1815.

[87] Rabani, E.; Baer, R. *Chem. Phys. Lett.* **2010**, *496*, 227–235.

[88] Baer, R.; Rabani, E. *Nano Lett.* **2012**, *12*, 2123–2128.

[89] Klimov, V. I.; Ivanov, S. S. a.; Nanda, J.; Achermann, M.; Bezel, I.; McGuire, J. a. J.; Piryatinski, A. *Nature* **2007**, *447*, 441–446.

[90] Lim, J.; Park, Y. S.; Klimov, V. I. *Nat. Mater.* **2018**, *17*, 42–48.

[91] Bae, W. K.; Park, Y.-S.; Lim, J.; Lee, D.; Padilha, L. a.; McDaniel, H.; Robel, I.; Lee, C.; Pietryga, J. M.; Klimov, V. I. *Nat. Commun.* **2013**, *4*, 2661.

[92] Klimov, V. I.; McGuire, J. A.; Schaller, R. D.; Rupasov, V. I. *Phys. Rev. B* **2008**, *77*, 195324.

[93] Li, Q.; Yang, Y.; Que, W.; Lian, T. *Nano Lett.* **2019**, *19*, 5620–5627.

[94] Chen, O.; Zhao, J.; Chauhan, V. P.; Cui, J.; Wong, C.; Harris, D. K.; Wei, H.; Han, H. S.; Fukumura, D.; Jain, R. K.; Bawendi, M. G. *Nat. Mater.* **2013**, *12*, 445–451.

[95] Hadar, I.; Philbin, J. P.; Panfil, Y. E.; Neyshtadt, S.; Lieberman, I.; Eshet, H.; Lazar, S.; Rabani, E.; Banin, U. *Nano Lett.* **2017**, *17*, 2524–2531.

[96] Hanifi, D. A.; Bronstein, N. D.; Koscher, B. A.; Nett, Z.; Swabeck, J. K.; Takano, K.; Schwartzberg, A. M.; Maserati, L.; Vandewal, K.; van de Burgt, Y.; Salleo, A.; Alivisatos, A. P. *Science* **2019**, *363*, 1199–1202.

[97] Javaux, C.; Mahler, B.; Dubertret, B.; Shabaev, A.; Rodina, A. V.; Efros, A. L.; Yakovlev, D. R.; Liu, F.; Bayer, M.; Camps, G.; Biadala, L.; Buil, S.; Quelin, X.; Hermier, J.-P. *Nat. Nanotechnol.* **2013**, *8*, 206–12.

[98] Pelton, M.; Andrews, J. J.; Fedin, I.; Talapin, D. V.; Leng, H.; O'Leary, S. K. *Nano Lett.* **2017**, *17*, 6900–6906.

[99] Zhang, L.; Li, H.; Liao, C.; Yang, H.; Xu, R.; Jiang, X.; Xiao, M.; Lu, C.; Cui, Y.; Zhang, J. *J. Phys. Chem. C* **2018**, *122*, 25059–25066.

[100] Kaledin, A. L.; Kong, D.; Wu, K.; Lian, T.; Musaev, D. G. *J. Phys. Chem. C* **2018**, *122*, 18742–18750.

[101] Neuhauser, D.; Rabani, E.; Cytter, Y.; Baer, R. *J. Phys. Chem. A* **2016**, *120*, 3071–3078.

[102] Takeshita, T. Y.; Jong, W. A. D.; Neuhauser, D.; Baer, R.; Rabani, E. *J. Chem. Theory Comput.* **2017**, *13*, 4605–4610.

[103] Dou, W.; Takeshita, T. Y.; Chen, M.; Baer, R.; Neuhauser, D.; Rabani, E. *J. Chem. Theory Comput.* **2019**, *15*, 6703–6711.

[104] Baer, R.; Neuhauser, D.; Rabani, E. *Phys. Rev. Lett.* **2013**, *111*, 106402.

[105] Neuhauser, D.; Gao, Y.; Arntsen, C.; Karshenas, C.; Rabani, E.; Baer, R. *Phys. Rev. Lett.* **2014**, *113*, 076402.

[106] Zhou, X. W.; Ward, D. K.; Martin, J. E.; Van Swol, F. B.; Cruz-Campa, J. L.; Zubia, D. *Phys. Rev. B* **2013**, *88*, 085309.

[107] Brumberg, A.; Harvey, S. M.; Philbin, J. P.; Diroll, B. T.; Crooker, S. A.; Wasielewski, M. R.; Rabani, E.; Schaller, R. D. *ACS Nano* **2019**, *13*, 8589–8596.

[108] Smith, A. M.; Mohs, A. M.; Nie, S. *Nat. Nanotechnol.* **2009**, *4*, 56–63.

[109] Park, Y. S.; Lim, J.; Klimov, V. I. *Nat. Mater.* **2019**, *18*, 249–255.

[110] Cunningham, P. D.; Boercker, J. E.; Foos, E. E.; Lumb, M. P.; Smith, A. R.; Tischler, J. G.; Melinger, J. S. *Nano Lett.* **2011**, *11*, 3476–3481.

[111] Sandberg, R. L.; Padilha, L. A.; Qazilbash, M. M.; Bae, W. K.; Schaller, R. D.; Pietryga, J. M.; Stevens, M. J.; Baek, B.; Nam, S. W.; Klimov, V. I. *ACS Nano* **2012**, *6*, 9532–9540.

[112] Baer, R.; Rabani, E. *J. Chem. Phys.* **2013**, *138*, 051102.

[113] Barzykin, A. V.; Tachiya, M. *Phys. Rev. B* **2005**, *72*, 075425.

[114] Ma, Y. Z.; Valkunas, L.; Dexheimer, S. L.; Bachilo, S. M.; Fleming, G. R. *Phys. Rev. Lett.* **2005**, *94*, 157402.

[115] Huang, L.; Krauss, T. D. *Phys. Rev. Lett.* **2006**, *96*, 057407.

[116] Wang, F.; Dukovic, G.; Brus, L. E.; Heinz, T. F. *Science* **2005**, *308*, 838–841.

[117] Pal, S.; Casanova, D.; Prezhdo, O. V. *Nano Lett.* **2018**, *18*, 58–63.

[118] Banin, U.; Ben-Shahar, Y.; Vinokurov, K. *Chem. Mater.* **2014**, *26*, 97–110.

[119] Ben-Shahar, Y.; Scotognella, F.; Kriegel, I.; Moretti, L.; Cerullo, G.; Rabani, E.; Banin, U. *Nat. Commun.* **2016**, *7*, 10416.

[120] Gillespie, D. T. *J. Phys. Chem.* **1977**, *81*, 2340–2361.

[121] Hu, J.; Li, L.-S.; Yang, W.; Manna, L.; Wang, L.-W.; Alivisatos, A. P. *Science* **2001**, *292*, 2060–2063.

[122] Talapin, D. V.; Lee, J. S.; Kovalenko, M. V.; Shevchenko, E. V. *Chem. Rev.* **2010**, *110*, 389–458.

[123] Carbone, L.; et al. *Nano Lett.* **2007**, *7*, 2942–2950.

[124] Talapin, D. V.; Nelson, J. H.; Shevchenko, E. V.; Aloni, S.; Sadtler, B.; Alivisatos, A. P. *Nano Lett.* **2007**, *7*, 2951–2959.

[125] Sitt, A.; Hadar, I.; Banin, U. *Nano Today* **2013**, *8*, 494–513.

[126] Steiner, D.; Dorfs, D.; Banin, U.; Sala, F. D.; Manna, L.; Millo, O. *Nano Lett.* **2008**, *8*, 2954–2958.

[127] Achtstein, A. W.; Schliwa, A.; Prudnikau, A.; Hardzei, M.; Artemyev, M. V.; Thomsen, C.; Woggon, U. *Nano Lett.* **2012**, *12*, 3151–3157.

[128] Benchamekh, R.; Gippius, N. A.; Even, J.; Nestoklon, M. O.; Jancu, J. M.; Ithurria, S.; Dubertret, B.; Efros, A. L.; Voisin, P. *Phys. Rev. B* **2014**, *89*, 035307.

[129] Richter, M. *Phys. Rev. Mater.* **2017**, *1*, 016001.

[130] Rajadell, F.; Climente, J. I.; Planelles, J. *Phys. Rev. B* **2017**, *96*, 035307.

[131] Scott, R.; Achtstein, A. W.; Prudnikau, A. V.; Antanovich, A.; Siebbeles, L. D. A.; Artemyev, M.; Woggon, U. *Nano Lett.* **2016**, *16*, 6576–6583.

[132] Zhang, Y.; Mascarenhas, A. *Phys. Rev. B* **1999**, *59*, 2040–2044.

[133] Naeem, A.; Masia, F.; Christodoulou, S.; Moreels, I.; Borri, P.; Langbein, W. *Phys. Rev. B* **2015**, *91*, 121302.

[134] Berkelbach, T. C.; Hybertsen, M. S.; Reichman, D. R. *Phys. Rev. B* **2013**, *88*, 045318.

[135] Ugeda, M. M.; Bradley, A. J.; Shi, S. F.; Da Jornada, F. H.; Zhang, Y.; Qiu, D. Y.; Ruan, W.; Mo, S. K.; Hussain, Z.; Shen, Z. X.; Wang, F.; Louie, S. G.; Crommie, M. F. *Nat. Mater.* **2014**, *13*, 1091–1095.

[136] Ithurria, S.; Dubertret, B. *J. Am. Chem. Soc.* **2008**, *130*, 16504–16505.

[137] Tessier, M. D.; Javaux, C.; Maksimovic, I.; Loriette, V.; Dubertret, B. *ACS Nano* **2012**, *6*, 6751–6758.

[138] Ithurria, S.; Bousquet, G.; Dubertret, B. *J. Am. Chem. Soc.* **2011**, *133*, 3070–3077.

[139] Cho, W.; Kim, S.; Coropceanu, I.; Srivastava, V.; Diroll, B. T.; Hazarika, A.; Fedin, I.; Galli, G.; Schaller, R. D.; Talapin, D. V. *Chem. Mater.* **2018**, *30*, 6957–6960.

[140] Christodoulou, S.; Climente, J. I.; Planelles, J.; Brescia, R.; Prato, M.; Martín-Garciá, B.; Khan, A. H.; Moreels, I. *Nano Lett.* **2018**, *18*, 6248–6254.

[141] Olutas, M.; Guzelturk, B.; Kelestemur, Y.; Yeltik, A.; Delikanli, S.; Demir, H. V. *ACS Nano* **2015**, *9*, 5041–5050.

[142] Bose, S.; Song, Z.; Fan, W. J.; Zhang, D. H. *J. Appl. Phys.* **2016**, *119*, 143107.

[143] She, C.; Fedin, I.; Dolzhnikov, D. S.; Demortière, A.; Schaller, R. D.; Pelton, M.; Talapin, D. V. *Nano Lett.* **2014**, *14*, 2772–2777.

[144] Li, Q.; Xu, Z.; McBride, J. R.; Lian, T. *ACS Nano* **2017**, *11*, 2545–2553.

[145] Guzelturk, B.; Pelton, M.; Olutas, M.; Demir, H. V. *Nano Lett.* **2019**, *19*, 277–282.

[146] Philbin, J. P.; Rabani, E. **2020**, arXiv:2005.03111.

[147] Diroll, B. T.; Fedin, I.; Darancet, P.; Talapin, D. V.; Schaller, R. D. *J. Am. Chem. Soc.* **2016**, *138*, 11109–11112.

[148] Bertrand, G. H.; Polovitsyn, A.; Christodoulou, S.; Khan, A. H.; Moreels, I. *Chem. Commun.* **2016**, *52*, 11975–11978.

[149] Yoon, D. E.; Kim, W. D.; Kim, D.; Lee, D.; Koh, S.; Bae, W. K.; Lee, D. C. *J. Phys. Chem. C* **2017**, *121*, 24837–24844.

[150] Zhao, H.; Moehl, S.; Kalt, H. *Phys. Rev. Lett.* **2002**, *89*, 097401.

[151] Li, Q.; Lian, T. *Acc. Chem. Res.* **2019**, *52*, 2684–2693.

[152] Ma, X.; Diroll, B. T.; Cho, W.; Fedin, I.; Schaller, R. D.; Talapin, D. V.; Gray, S. K.; Wiederrecht, G. P.; Gosztola, D. J. *ACS Nano* **2017**, *11*, 9119–9127.

[153] Rashba, E. I. *Sov Phys Semicond* **1975**, *8*, 807–816.

[154] Feldmann, J.; Peter, G.; Göbel, E. O.; Dawson, P.; Moore, K.; Foxon, C.; Elliott, R. J. *Phys. Rev. Lett.* **1987**, *59*, 2337.

[155] Korkusinski, M.; Voznyy, O.; Hawrylak, P. *Phys. Rev. B* **2010**, *82*, 245304.

[156] Birkedal, D.; Singh, J.; Lyssenko, V. G.; Erland, J.; Hvam, J. M. *Phys. Rev. Lett.* **1996**, *76*, 672–675.

[157] Singh, J.; Birkedal, D.; Lyssenko, V.; Hvam, J. *Phys. Rev. B* **1996**, *53*, 15909–15913.

[158] Tran Thoai, D. B.; Zimmermann, R.; Grundmann, M.; Bimberg, D. *Phys. Rev. B* **1990**, *42*, 5906.

[159] Plimpton, S. *J. Comput. Phys.* **1995**, *117*, 1–19.